University of Sussex

Search for Supersymmetry in final states with three leptons and missing transverse energy with the ATLAS detector at the Large Hadron Collider

Itzebelt Santoyo Castillo

Submitted for the degree of Doctor of Philosophy

University of Sussex

July 2014

Declaration

I hereby declare that this thesis has not been and will not be submitted in whole or in part to another University for the award of any other degree.

Signature:

Itzebelt Santoyo Castillo

UNIVERSITY OF SUSSEX

Itzebelt Santoyo Castillo, Doctor of Philosophy

Search for Supersymmetry in final states with three leptons and missing transverse energy with the ATLAS detector at the Large Hadron Collider

Summary

The ATLAS experiment at the Large Hadron Collider has collected an unprecedented amount of data in the 3 years of data taking since its start. In this document I will discuss the results of the analysis I performed during my PhD at the university of Sussex for the search of Supersymmetry in events with three leptons (electron/muon/tau) and missing transverse energy in the final state. The search is performed on the full dataset collected by the experiment in 2012, at a centre-of-mass energy of 8 TeV. These results are interpreted in SUSY models with chargino-neutralino pair production via decays involving sleptons, staus, gauge bosons and the newly discovered Higgs boson. These results presented improve on previous searches performed at ATLAS in three lepton final states with only electrons and muons. Special focus will be given to the optimisation process of Supersymmetry signal with respect to the SM background, and the statistical interpretation of the results obtained with this search.

Acknowledgements

I would like to take this space to acknowledge all the wonderful people who supported me throughout this PhD journey which would not have been possible without the financial help of my sponsor: the Mexican science and technology council, CONACYT.

First and foremost, I'd like to thank my supervisor, Fabrizio Salvatore, whose friendly guidance has been invaluable during these past four years. Thanks to Antonella De Santo for giving me the opportunity to join their lovely Sussex group. Tina Potter, a person who I learnt the most from and was a true pleasure to work with, thank you for the stimulating conversations and the above and beyond help. My Sussex colleagues and friends in chronological order: Anthony Rose and Stewart Martin-Haugh, thanks for introducing me to the bits and pieces of the SUSY world and putting up with all my questions at all times; Zara Grout, who has always been a really good friend and a great work buddy; Yusufu, Dan, James, Ed for giving the office a very friendly, funny and pleasant atmosphere. Thanks to the trileptoners: Zoltan, Steve, Lukas and the amazing Basil Schneider, who I worked very closely with during my analysis work. And the friendly faces at CERN who made work trips more fun: Emma, Brett, Nadja, Olivier, Brokk, Dennis and Devin.

I would also like to thank my amazing parents, Elizabeth and Socrates, for their enormous support and encouragement to become the best person I could be. My two great sisters, who are my original life role models. My dear friends: Nina, you gave me courage and strength when I most needed it, and of course, the never ending jokes, you personify the word "friend" my friend; Noor, you are always looking out for me and I'm so lucky to have you as one of my 'B'est friends; Antonio and Luca, my oldest friends at Sussex who made the UK a great place to live in; Yolis and Alma, my life-long friends; Grace K who is such a good supportive friend.

And last but certainly not least, I'm beyond grateful to have a person who I could count on for anything and gave me the uttermost support, my fiancé Bjoern Lekitsch, I'm so glad I found you... this is for us.

Contents

List of Tables

List of Figures

Chapter 1

Introduction

This document summarises the work done during the four years of my PhD at the University of Sussex as part of the ATLAS collaboration at the Large Hadron Collider. The analysis presented in this thesis describes the search for Supersymmetry in events with three leptons and missing transverse energy in the final state using the ATLAS detector. Firstly, the theoretical background is reviewed in Chapter 2, which describes the features of the Standard Model of particle physics as well as its shortcomings, which motivate the need for an extended theory such as Supersymmetry. Chapter 3 focuses on introducing the experimental setup used for these searches: the ATLAS detector at the Large Hadron Collider. Chapters 4-6 give an overview of the tools used in the analysis presented in this thesis, from MC-simulated and real data, to the algorithms used for particle reconstruction and identification. Chapter 7 provides a description of the SUSY trilepton analysis, focusing on my personal contribution. Chapter 8 shows the results of this analysis and Chapter 9 provides some concluding remarks. A brief description on the service work done for the ATLAS experiment during the qualification period is also provided in Appendix B.

This analysis has been published in a refereed paper [1] in April 2014.

Chapter 2

Theoretical Introduction

> "It doesn't matter how beautiful your theory is, it doesn't matter how smart you are. If it doesn't agree with experiment, it's wrong."
>
> Richard P. Feynman

The Standard Model (SM) theory aims to provide a general description of fundamental particles and the way they interact in nature. However, there are several "known unknowns" that are not addressed by this theory.

This chapter gives a brief overview of the most successful theory in particle physics, the Standard Model, as well as some of its limitations which motivate the need for an extended description. Many theoretical extensions of the Standard Model have been formulated to cover such limitations, one of the most popular being Supersymmetry.

2.1 The Standard Model

The Standard Model of particle physics [2, 3, 4] is a remarkable theory which can explain most of the current experimental observations as well as some cosmological phenomena in the early universe. It summarises the current knowledge of the fundamental particles and their interactions in terms of three forces: the electromagnetic, weak and strong (gravity is not considered). It is based on a relativistic Quantum Field Theory (QFT) [5], where particles are treated as fields. This section focuses on the description of the field content of the SM, the interactions compatible with that content and the limitations they imply.

2.1.1 Overview

Elementary particles are generally distinguished by mass eigenstates and quantum numbers. Based on the spin quantum numbers, the elementary particles described within the SM are divided into two types: fermions and bosons, with corresponding spin quantum numbers of half-integer and integer, respectively.

Fermions

Fermions are subdivided into: six quarks, also referred to as "colour triplets" due to the fact that they carry one of three so-called "colour" charges (red, green or blue); and six leptons, three of them electrically neutral, known as neutrinos. Tables 2.1- 2.2 show the categorisation of quarks and leptons, respectively, along with a few of their fundamental properties. Leptons and quarks are organised in three generations each containing one charged lepton, one neutrino, and one up- and down-type quarks. The masses of fermions increase with each generation. The generations are grouped according to their left- and right-handed chirality states, this due to the chiral nature of the theory discussed in Section 2.1.1. Chirality is an non-physical concept closely related to handedness (defined as the projection of the spin of a particle onto its direction of motion), which is equivalent in the case of massless particles. Neutrinos are the only fermionic fields which are assumed massless in the SM and can therefore be considered as either left- or right-handed. Each fermion has an associated antiparticle with all the same quantum numbers but one (two in case of quarks), which is inverted: this is the charge in case of charged leptons, "handedness" in case of neutrinos, and charge as well as colour in case of quarks.

Table 2.1: Quarks in the Standard Model.

		Name	Symbol	Mass [MeV]	Charge [e]
Generation	1st	Up	u	2.3	$+2/3$
		Down	d	4.8	$-1/3$
	2nd	Charm	c	1.3×10^{3}	$+2/3$
		Strange	s	9.5×10^{1}	$-1/3$
	3rd	Top	t	1.7×10^{5}	$+2/3$
		Bottom	b	4.2×10^{3}	$-1/3$

Table 2.2: Leptons in the Standard Model.

		Name	Symbol	Mass [MeV]	Charge [e]
Generation	1st	Electron	e	0.511	-1
		Electron Neutrino	ν_e	$\leq 0.022 \times 10^{-1}$	0
	2nd	Muon	μ	1.057×10^{2}	-1
		Muon Neutrino	ν_μ	$\leq 0.017 \times 10^{1}$	0
	3rd	Tau	τ	1.777×10^{3}	-1
		Tau Neutrino	ν_τ	$\leq 0.155 \times 10^{2}$	0

Forces

Each force in the SM is described by a gauge theory, where the interactions are mediated by gauge fields of the corresponding local symmetry group. All fermions can interact via the weak and electromagnetic forces; additionally quarks can also interact via the strong force. These interactions arise from the exchange of gauge bosons. Table 2.3 summarises the three forces described in the SM, the mass and charge properties of their corresponding mediating particle(s) (gauge bosons).

Table 2.3: Gauge Bosons in the Standard Model.

Force	Name	Symbol	Mass [GeV]	Charge [e]
Electromagnetic	Photon	γ	0	0
Weak	W	$W^{\pm}$	80.398	± 1
	Z	Z	91.188	0
Strong	Gluons	g	0	0

The theory that describes the electromagnetic interactions is the Quantum ElectroDynamics (QED) [6], where the force carrier is the electrically neutral and massless photon, which couples to all charged particles. The strong force, mediated by the exchange of the electrically neutral, coloured and massless gluons, is described by the Quantum ChromoDynamics (QCD) gauge field theory [7]. The weak force is mediated by the heavy Z and $W^{\pm}$ bosons. The gravitational force, with the Graviton as mediator, is not included in Table 2.3, as it is not a part of the SM description.

The electromagnetic and weak forces are described by one unified gauge theory, known as the electroweak theory [8]. It is believed [9] that at very high energies ($\sim 10^{16}$ GeV) the strong and electroweak forces are unified into one force, which may be described by a

Grand Unified Theory (GUT).

Gauge Groups in the SM

In gauge field theory, an interaction can be described by the invariance of fermion fields under a transformation, T_X, where the quantity X is conserved [10].

The SM force interactions can be mathematically described by the local gauge symmetry group presented in Equation 2.1.

$$SU(3)_C \times SU(2)_L \times U(1)_Y, \tag{2.1}$$

where the indices: C denotes colour charge; L denotes left-handedness; and Y denotes weak-hypercharge, a variable used to assess the correlation between the electric charge (Q) and the third component of the weak isospin (I_3), defined as $Q = I_3 + \frac{Y}{2}$, where I_3 is equal to $\pm 1/2$ for left-handed particles and 0 for right-handed particles.

The $SU(3)_C$ gauge group [11] describes the strong interactions (using QCD) acting on coloured fermion fields. This is a non-Abelian group, meaning that not all the group elements commute, where self-interaction terms are allowed, i.e. gluons may couple to themselves. The specific gauge bosons associated to the algebra of the $SU(3)_C$ group are eight massless gluons, denoted as $G_\mu^{\alpha=1,...8.}$, which mediate the interactions. Quark fields are treated as colour triplets (three component field) under the $SU(3)_C$ symmetry, gluons are colour octets and the rest of the gauge bosons and leptons are colour singlets (colourless particles). Another property of the $SU(3)_C$ group symmetry is that it acts in the same way for left- and right-handed particles, and it is therefore considered a non-chiral gauge group.

The weak interactions [6] are represented by the massless $SU(2)_L$ [2] gauge fields, $W_\mu^{\alpha=1,2,3.}$. These massless gauge fields violate parity by acting only on left-handed components of the fermion fields, and therefore left-handed particles are treated as doublets and right-handed particles as singlets. $SU(2)_L$ is also a non-Abelian symmetry group, hence, the weak gauge bosons may couple to each other.

QED is based on the Abelian symmetry group is $U(1)_Q$ [2], which is used to describe the electromagnetic force, where the interaction is between charged fermions and the massless photon. Since it acts on left- and right-handed particles with different strength, it is considered a chiral gauge group.

The ElectroWeaK (EWK) sector corresponds to the $SU(2)_L \times U(1)_Y$ term in Equation 2.1, where the gauge field associated to the $U(1)_Y$ symmetry is identified by B_μ^0.

The four non-physical bosons, $W_\mu^{\alpha=1,2,3.}$ and B_μ^0, associated with the $SU(2)_L$, $U(1)_Y$ symmetries and with corresponding gauge coupling constants g and g', respectively, are related to the physical bosons that mediate the electroweak interactions: $W^\pm, Z$ and γ. The electroweak mixing for gauge bosons (field mixing) is expressed as:

$$W_\mu^\pm = \frac{1}{\sqrt{2}}(W_\mu^1 \mp iW_\mu^2) \tag{2.2}$$

$$Z_\mu = B_\mu^0 cos(\theta_W) + W_\mu^3 sin(\theta_W) \tag{2.3}$$

$$A_\mu = -B_\mu^0 sin(\theta_W) + W_\mu^3 cos(\theta_W) \tag{2.4}$$

where θ_W is the experimentally determined weak mixing angle defined as a ratio of the electroweak coupling constants g and g' ($tan\theta_W = g'/g$) and A_μ is the associated photon field.

Electroweak Symmetry Breaking

The SM can be described by the invariance of massless fermion fields under $SU(3)_C \times SU(2)_L \times U(1)_Y$ transformations, where all the gauge bosons responsible for mediating the forces are considered massless. This is not a problem for the gluon and photon, which mediate long range forces and must be massless. However, it is known from experiments [12] that three of the gauge bosons, $W^\pm$ and Z, have mass, as do the charged leptons and quarks. In order for the SM assumptions to be valid, the electroweak sector symmetry must be broken.

Equation 2.5 defines the Standard Model Lagrangian as the sum of the Lagrangians describing the action of each force in the SM, the interactions and masses of all elementary particles in nature:

$$\mathcal{L}_{SM} = \mathcal{L}_{QCD} + \mathcal{L}_{EWK} + \mathcal{L}_{Mass}, \tag{2.5}$$

If mass terms ($\mathcal{L}_{Mass}$) are inserted by hand into the SM Lagrangian, this would break the gauge invariance of the SM theory, which also leads to divergences and thus, a non-renormalisable theory. The Higgs mechanism [13] overcomes this problem by introducing a scalar field, known as the Higgs field, which couples to massive fermionic and bosonic particles. A complex scalar field (two degrees of freedom) can be generally written as

$$\phi = \frac{\phi_1 + i\phi_2}{\sqrt{2}}, \tag{2.6}$$

with a description provided by a Lagrangian density,

$$\mathcal{L} = (\partial_\mu \phi)^* (\partial^\mu \phi) - V(\phi), \tag{2.7}$$

and an associated potential,

$$V(\phi) = \mu^2|\phi|^2 + \lambda|\phi|^4. \tag{2.8}$$

If the μ and λ constants in Equation 2.8 are assumed to be real, the $V(\phi)$ potential has the shape shown in Figure 2.1. The ground state (minimum) of this potential, the so-called Vacuum Expectation Value (VEV) of the Higgs field, is a circle in the complex plane of radius $|\phi_0|$, which is non-zero ($|\phi_0| = \sqrt{\frac{-mu^2}{\lambda}} = \nu$). In order to generate masses, the gauge symmetry must be broken in a way that preserves the global Lagrangian symmetry at the same time, in order to guarantee a renormalisable theory. This dilemma can be solved by "Spontaneous" Symmetry Breaking (SSB), a mechanism where there is a symmetric Lagrangian, but not a symmetric VEV. For example if a Lagrangian invariant under a generic transformation, G, has a degenerate set of states with minimal energy that transform under G as the members of a given multiplet, and if one of those states is arbitrarily selected as the ground state of the system, the symmetry is said to be spontaneously broken.

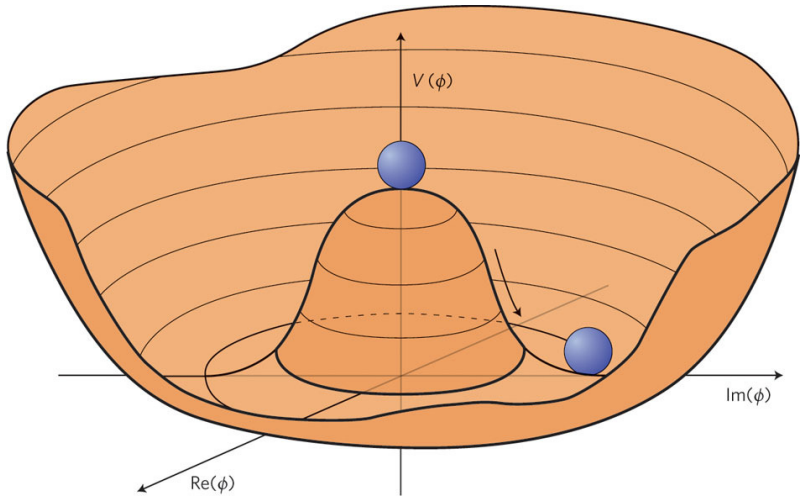

Figure 2.1: Visualisation of the Higgs potential, so called "Mexican hat" in the complex (ϕ_1, ϕ_2) plane [14]. The lowest-energy state is described by a randomly chosen point around the bottom of the hat.

The VEV of the Higgs field is not invariant under gauge transformations and so spontaneously breaks the gauge symmetry, which means that the symmetry is preserved in the model but not on the ground state of the vacuum. The Lagrangian in equation 2.7 is expanded around the selected minimum in order to obtain the equations of motion in terms of new fields which have a zero VEV, η and ξ:

$$\phi(x) = \frac{\nu + \eta(x) + i\xi(x)}{\sqrt{2}}. \tag{2.9}$$

The expanded Lagrangian becomes

$$\mathcal{L} = \frac{1}{2}(\partial_\mu \eta)(\partial^\mu \eta) - \frac{1}{2}(\partial^\mu \xi)(\partial_\mu \xi) - \frac{1}{2}m_\eta^2 + const + \mathcal{O}(\eta, \xi). \tag{2.10}$$

This equation shows that only one of the two fields, η, contains mass and the other one, ξ, is massless. The higher-order terms in η and ξ represent the field interactions. If the same reasoning is applied to a doublet of complex scalar field (four degrees of freedom) then it is possible to generate all the necessary masses for the gauge bosons. Three out of the four degrees of freedom will generate masses for the $W^\pm$, Z bosons, the fourth degree of freedom generates the mass for a real neutral scalar field, the Higgs boson. The photon does not pick up such mass terms in the Lagrangian, hence remaining massless.

This mechanism gives mass to the gauge bosons without violating gauge symmetry. The weak gauge bosons and fermions acquire mass by interacting with the Higgs field, and the mass generated is proportional to the strength of their coupling with the Higgs boson. In particular, fermions can acquire mass through Yukawa couplings [15] to the Higgs field, where the coupling constant and thus the mass can be different for each particle.

The observed differences in the masses of fermions across generations and bosons are not explained by the SM, these unknown features can be parametrised by the SM Lagrangian implying that they are to be considered as "free" parameters in the SM theory. There are 19 free parameters in the SM, including the masses for all charged fermions, mixing parameters, coupling constants, the Z boson mass, and the mass of the Higgs boson, which has been a main subject of study for many experiments.

In 2012, searches at the LHC showed evidence for the discovery of a new particle whose mass was consistent with the SM Higgs ($\sim$125 GeV) [16, 17]. The following year, studies from the ATLAS and CMS experiments confirmed that this particle is consistent with the SM Higgs (some of the latest results can be found in [18, 19]), completing the SM particle content description.

2.1.2 Shortcomings of The Standard Model

Experimental results on the measurements of several of the parameters in the SM have demonstrated the goodness of this model [20]. In Figure 2.2 the measurement of the production cross section of several processes is compared to the SM prediction, showing a very good agreement between the two.

Despite the experimental success of SM theory, many fundamental questions remain unanswered, some of them associated with the adhoc tuning of its free parameters (also known as "fine-tuning" [21]) and others associated to unexplained observational facts. This section briefly describes some of these limitations.

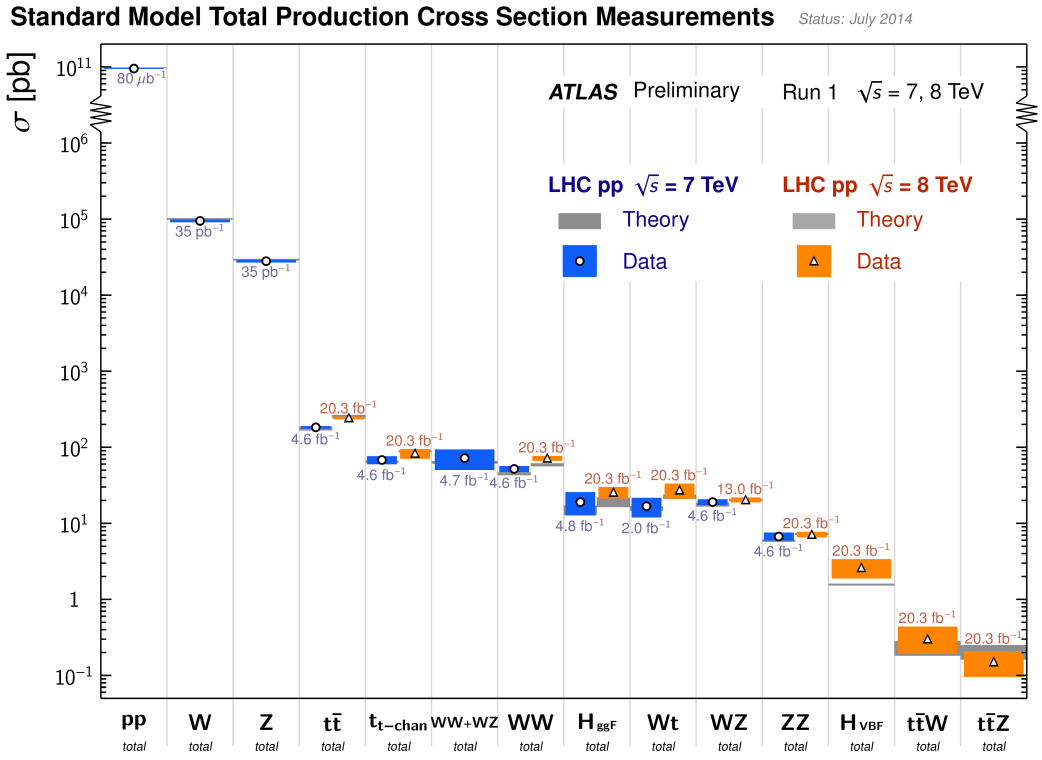

Figure 2.2: Summary of several Standard Model total production cross section measurements at ATLAS, compared to the corresponding theoretical expectations. All theoretical expectations were calculated at NLO or higher. The W and Z vector-boson inclusive cross sections were measured at ATLAS with 35 pb^{-1} of integrated luminosity from the 2010 dataset. All other measurements were performed using the 2011 or 2012 ATLAS dataset [20].

Hierarchy Problem

The mass of the Higgs, m_H^2, receives extremely large quantum corrections [22] from the coupling of every particle to the Higgs field. If the Higgs couples to a fermion (scalar) field, , f (S), with mass m_f (m_S), then this introduces a term in the Lagrangian of the form $-\lambda_f H\bar{f}f$ ($-\lambda_S H\bar{S}S$). The diagrams shown in Figure 2.3 illustrate the coupling (loop diagram) of a Higgs boson to a fermion (a) and scalar (b) field.

The corresponding quadratic Higgs mass corrections from the loop diagrams shown in

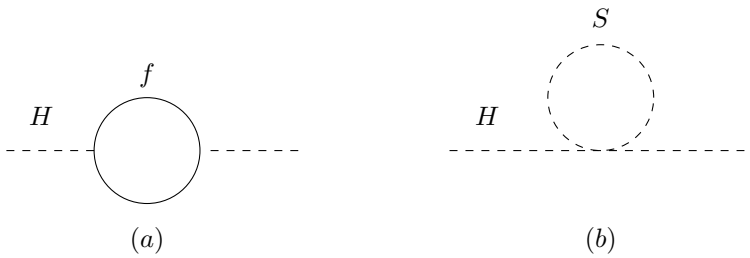

Figure 2.3: One-loop quantum corrections to the Higgs squared mass parameter m_H^2 , due to (a) a fermion field f and (b) a scalar field S.

Figure 2.3 are

$$\Delta m_H^2 = -\frac{|\lambda_f|^2}{8\pi^2}\Lambda_{UV}^2 + \dots \tag{2.11}$$

and

$$\Delta m_H^2 = -\frac{|\lambda_S|^2}{16\pi^2}[\Lambda_{UV}^2 - 2m_S^2 \ln(\Lambda_{UV}/m_S) + \dots], \tag{2.12}$$

where Λ_{UV}^2 is an ultraviolet momentum cut-off used to regulate the loop integral. If Λ_{UV}^2 is of the order of the Planck scale, then the quantum correction to m_H^2 is around 30 orders of magnitude larger than the value of the mass of the Higgs boson associated with electroweak symmetry breaking scale ($\sim$ (100 GeV)^2). In other words, the mass of the Higgs will not be at the electroweak scale but much more massive. Given that all fermions and electroweak bosons in the SM obtain masses from the Higgs expectation value ($\langle H \rangle$), the entire mass spectrum of the Standard Model will be sensitive to this cut-off scale, Λ_{UV}^2.

Dark Matter

Dark matter is a form of matter that cannot be observed directly, but whose existence can be inferred from gravitational effects on matter that is visible, such as the rotation curve of galaxies (rotational velocity as function of the distance from the centre of the galaxy). Latest cosmological observations [23] suggest that this new kind of matter makes up about 27% of the energy density of the universe. Very little is known about the remaining 68% fraction of the universe, called dark energy. Candidate particles for dark matter include the so-called Weakly-Interacting Massive Particles (WIMPs). These hypothetical neutral particles only participate in the gravitational and weak interactions and thus are extremely difficult to detect. Neutrinos are the only WIMP-like particles within the Standard Model field content. However, they are not massive and abundant enough to account for dark

matter, which means that the particle content within the SM fails to provide a dark matter candidate.

Given all the experimental work in the last 4 decades, it becomes clear that the SM provides a rather incomplete description of nature, which only works at the electroweak energy scale. Physics Beyond the Standard Model (BSM) aims to fill the gaps of the SM and by doing so, reduces the number of free parameters in the SM theory, which are to be determined experimentally. One approach of BSM theories is to consider the same fundamental fields but with new interactions, covered by theories such as supersymmetry [24]. Supersymmetry is one of the favoured BSM theory candidates, which by introducing a new symmetry manages to solve the hierarchy problem, provide a dark matter candidate (more on Section 2.2.2) and provide new spectrum of particles that can enable exploring physics beyond the electroweak scale. SUperSYmmetry (SUSY) is the main focus of the search discussed in this thesis.

2.2 Supersymmetry

Supersymmetry introduces a new symmetry that relates scalar fields to fermionic fields, and in doing so, prevents large radiative corrections to the Higgs mass. Each SM particle will have an associated superpartner (known also as "sparticles") which differs in spin by 1/2.

The SUSY algebra is generated with operators Q that transform a fermionic state into a bosonic one, and vice versa

$$Q|Fermion\rangle = |Boson\rangle \tag{2.13}$$

$$Q|Boson\rangle = |Fermion\rangle. \tag{2.14}$$

If supersymmetry was an exact symmetry of nature, then SM particles and their superpartners would have the same quantum numbers, thus the same mass. However, superpartners are yet to be observed, therefore, supersymmetry must be a broken symmetry. The SUSY breaking must occur in such a way that the sparticles are not too heavy to avoid re-introducing the hierarchy problem and still manage to solve the shortcomings within the Standard Model. This can be achieved with the "soft" SUSY breaking mechanism [25]. This form of SUSY breaking imposes constrains on the masses of all superpartners and sets them to a phenomenologically suitable range.

As seen in Section 2.1.2, the SM introduces radiative corrections to the Higgs boson

mass squared due to its coupling to scalar and fermionic fields. Comparing the correction terms for the Higgs mass due to its coupling to a fermionic and bosonic field (Equations 2.11 and 2.12) strongly suggests that if there is a symmetry that can relate fermions and bosons with $\lambda_f^2 = 2m_f^2/\nu^2 = -\lambda_S$ [26], then the quadratic divergences of the Higgs mass term cancel each other out. If this new symmetry exists, it can naturally solve the hierarchy problem.

2.2.1 Minimal Supersymmetric Standard Model

A Minimal Supersymmetric extension of the SM (MSSM) [27] is defined so that it contains all the SM particles described in Section 2.1 as well as their corresponding superpartners, and by so, effectively doubling the particle content in the theory. The MSSM particle content is listed in Table 2.4.

Table 2.4: Supersymmetric Particles in the MSSM [28].

Name	Spin	Gauge Eigenstates	Mass Eigenstates
Squarks ($\tilde{q}$)	0	$\tilde{u}_L\ \tilde{u}_R\ \tilde{d}_L\ \tilde{d}_R$	(same)
		$\tilde{s}_L\ \tilde{s}_R\ \tilde{c}_L\ \tilde{c}_R$	(same)
		$\tilde{t}_L\ \tilde{t}_R\ \tilde{b}_L\ \tilde{b}_R$	$\tilde{t}_1\ \tilde{t}_2\ \tilde{b}_1\ \tilde{b}_2$
Sleptons ($\tilde{\ell}$)	0	$\tilde{e}_L\ \tilde{e}_R\ \tilde{\nu}_e$	(same)
		$\tilde{\mu}_L\ \tilde{\mu}_R\ \tilde{\nu}_\mu$	(same)
		$\tilde{\tau}_L\ \tilde{\tau}_R\ \tilde{\nu}_\tau$	$\tilde{\tau}_1\ \tilde{\tau}_2\ \tilde{\nu}_\tau$
Higgs bosons	0	$H_u^0\ H_d^0\ H_u^+\ H_d^-$	$h^0\ H^0\ A^0\ H^\pm$
Neutralinos ($\tilde{\chi}_j^0$)	1/2	$\tilde{B}^0\ \tilde{W}^0\ \tilde{H}_u^0\ \tilde{H}_d^0$	$\tilde{\chi}_1^0\ \tilde{\chi}_2^0\ \tilde{\chi}_3^0\ \tilde{\chi}_4^0$
Charginos ($\tilde{\chi}_i^\pm$)	1/2	$\tilde{W}^\pm\ \tilde{H}_u^+\ \tilde{H}_d^-$	$\tilde{\chi}_1^\pm\ \tilde{\chi}_2^\pm$
Gluino	1/2	$\tilde{g}$	(same)
Gravitino	3/2	$\tilde{G}$	(same)

The spin-0 superpartners of the quarks and leptons are called squarks ($\tilde{q}$) and sleptons ($\tilde{\ell}$), short for "scalar quark" and "scalar lepton", respectively, and are also collectively known as sfermions ($\tilde{f}$). In the case of bosonic fields, each of the vector bosons and the SM Higgs have a fermionic superpartners which are jointly referred to as gauginos and higgsino (H_u and H_d), respectively. There are two complex Higgs doublets $H_u = (H_u^+, H_u^0)$ and $H_d = (H_d^0, H_d^-)$ rather than just one as in the Standard Model, with a ν_u and ν_d as their respective VEVs, where both of these values are constrained by the SM Higgs VEV as $\nu = \sqrt{\nu_u^2 + \nu_d^2}$.

After electroweak symmetry breaking, the two Higgs doublets generate eight degrees of

freedom: three for neutral Higgs bosons (h^0, the one with the lightest mass, H^0 and A^0), two for charged Higgs bosons ($H^{\pm}$) and the rest to give mass to the Z and $W^{\pm}$ bosons of the SM. The higgsinos and electroweak gauginos (the so called wino, $\tilde{W}^{\pm}$, and bino, $\tilde{B}^0$) mix with each other because of the effects of electroweak symmetry breaking, resulting in four neutralinos ($\tilde{\chi}^0_{1,2,3,4}$) and four charginos ($\tilde{\chi}^{\pm}_{1,2}$). The mixing of these gauginos is given by Equations 2.15-2.16.

$$\begin{pmatrix} \tilde{\chi}^{\pm}_1 \\ \tilde{\chi}^{\pm}_2 \end{pmatrix} = \begin{pmatrix} M_2 & \sqrt{2} m_W sin\beta \\ \sqrt{2} m_W cos\beta & \mu \end{pmatrix} \begin{pmatrix} \tilde{W}^{\pm} \\ \tilde{H}^{\pm} \end{pmatrix} \tag{2.15}$$

$$\begin{pmatrix} \tilde{\chi}^0_1 \\ \tilde{\chi}^0_2 \\ \tilde{\chi}^0_3 \\ \tilde{\chi}^0_4 \end{pmatrix} = \begin{pmatrix} M_1 & 0 & -m_Z cos\beta sin\theta_W & m_Z sin\beta cos\theta_W \\ 0 & M_2 & m_Z cos\beta cos\theta_W & m_Z sin\beta cos\theta_W \\ -m_Z cos\beta sin\theta_W & m_Z cos\beta cos\theta_W & 0 & -\mu \\ m_Z sin\beta cos\theta_W & m_Z sin\beta cos\theta_W & -\mu & 0 \end{pmatrix} \begin{pmatrix} \tilde{B}^0 \\ \tilde{W}^0 \\ \tilde{H}^0_u \\ \tilde{H}^0_d \end{pmatrix}, \tag{2.16}$$

where the parameters M_1, M_2, M_3 refer to the gaugino masses; μ refers to the higgsino mass; β is defined as a ratio of the electroweak coupling constants g and g' and θ_W is defined as the ratio of the VEVs of the two Higgs doublet fields; and the $m_Z(m_W)$ are the masses of the $W(Z)$ boson. Charginos are linear combinations of the charged winos and higgsinos, while the neutralinos are linear combinations of the neutral wino, bino and higgsinos. Therefore, each neutralino and chargino will have a different composition (bino-like, wino-like or higgsino-like) that determines the way in which they decay.

In the MSSM, the soft SUSY-breaking terms [22] introduce a large number of unknown parameters (~ 100) in addition to the 19 free parameters of the SM, which makes any phenomenological analysis extremely complicated. There are several complementary supersymmetric models within the MSSM framework which are mainly defined to reduce the number of free parameters in the MSSM: the so-called "simplified models" [29], which significantly reduce the number of parameters to only the masses of the particles that are relevant for a particular SUSY process of study, by setting all other masses to experimentally inaccessible values; and the phenomenological MSSM [30], which uses existing experimental data and conservative phenomenological assumptions to constrain the values for the mass parameters. A subset of these parameters is listed in Table 2.5, which contains: the gaugino masses (M_1, M_2, M_3); the Higgs mass parameters ($m^2_{H_1}, m^2_{H_2}$); and the ratio of the Higgs VEVs related to the mass of the Z boson and the electroweak gauge couplings (g and g')

$$\nu_u^2 + \nu_d^2 = 2m_Z^2/(g^2 + g'^2) \tag{2.17}$$

with

$$\nu_u = \langle H_u^0 \rangle \ , \ \nu_d = \langle H_d^0 \rangle. \tag{2.18}$$

Table 2.5: List of main free parameters within the pMSSM description [22].

Parameters	Definition
$tan\beta$	The ratio of the VEVs of the two Higgs doublet fields ($\langle H_u^0 \rangle / \langle H_d^0 \rangle$).
m_{A^0}, μ	The higgsino mass parameters.
M_1, M_2, M_3	The bino, wino and gluino mass parameters.
$m_{\tilde{q}}, m_{\tilde{u}_R}, m_{\tilde{d}_R}, m_{\tilde{l}}, m_{\tilde{e}_R}$	The first/second generation sfermion mass parameters.
A_u, A_d, A_e	The first/second generation tri-linear couplings.
$m_{\tilde{Q}}, m_{\tilde{t}_R}, m_{\tilde{b}_R}, m_{\tilde{L}}, m_{\tilde{\tau}_R}$	The third generation sfermion mass parameters.
A_t, A_b, A_τ	The third generation tri-linear couplings.

Simplified models and pMSSM are used to perform the SUSY searches described in this thesis.

SUSY Models

There are very powerful constraints on the production of strongly interacting SUSY particles (squarks and gluinos) [31], and depending on the mechanism of SUSY breaking, it could be that these strongly interacting squarks and gluinos are too massive to be produced at the LHC. This motivates a separate consideration for electroweak SUSY particle production, i.e. direct production of colourless particles. The pair production cross section as a function of mass for the EWK processes: $\tilde{\nu}_e\tilde{\nu}_e$, $\tilde{\ell}_e\tilde{\ell}_e$, $\tilde{\chi}_2^0\tilde{\chi}_1^\pm$ and $\tilde{\chi}_2^0\tilde{g}$, is shown in Figure 2.4.

One of the most promising ways to discover EWK SUSY production at the LHC is through the detection of events with multiple charged leptons in the final state. Particularly, charginos and neutralinos can produce sleptons, gauge bosons or Higgs bosons as an intermediate particle in their decays into charged leptons, as shown in Figures 2.5-2.6. Charged sleptons may also be produced directly if they are sufficiently light. Chargino (or sleptons) decays can have one charged lepton in the final state and neutralino decays can have two charged leptons in the final state, which combined yield three leptons in the final state. It is for this reason that the EWK SUSY production mode of charginos and neutralinos, mediated by electroweak interactions is explored in this analysis.

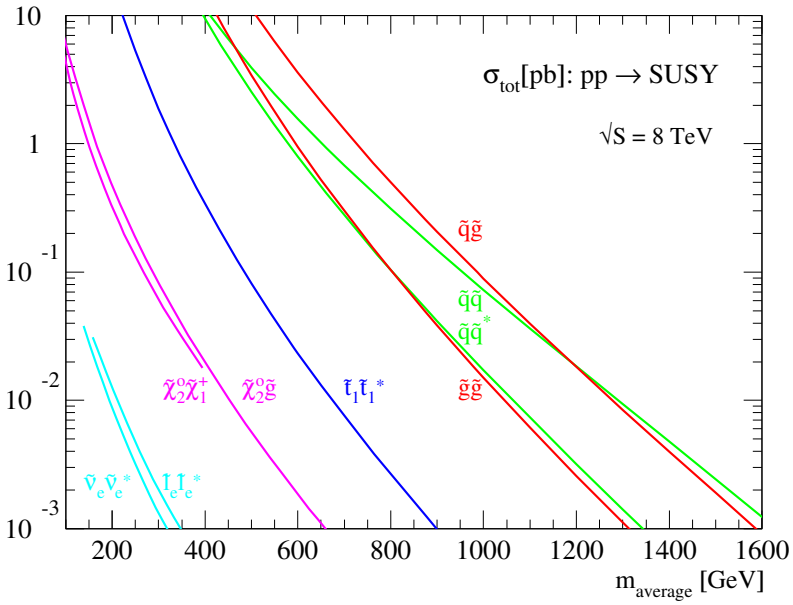

Figure 2.4: Production cross section for supersymmetric particles at the LHC energy of $\sqrt{s} = 8$ TeV as a function of mass [32].

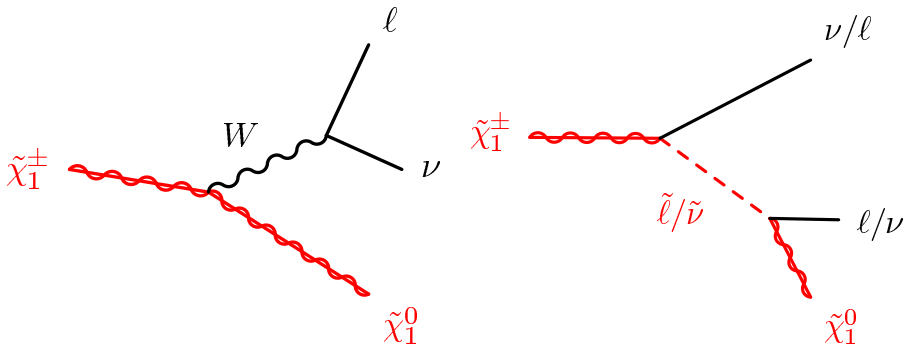

(a) $\tilde{\chi}_1^{\pm}$ decaying into a $W^{\pm}$ boson and the LSP.

(b) $\tilde{\chi}_1^{\pm}$ decaying into a $\tilde{\ell}/\tilde{\nu}$ and ν/ℓ.

Figure 2.5: Diagrams for the electroweak SUSY production of charginos with leptons in the final state. The symbols $\tilde{\ell}$ and ℓ refer to $\tilde{e}/\tilde{\mu}/\tilde{\tau}$ and $e/\mu/\tau$, respectively.

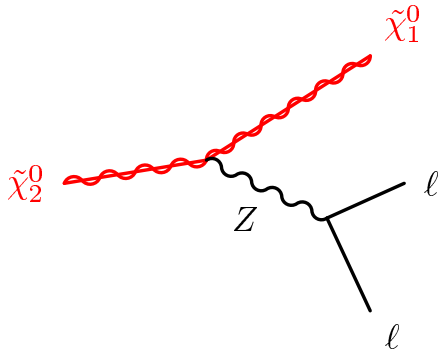

(a) $\tilde{\chi}_2^0$ decaying into a Z boson and the LSP.

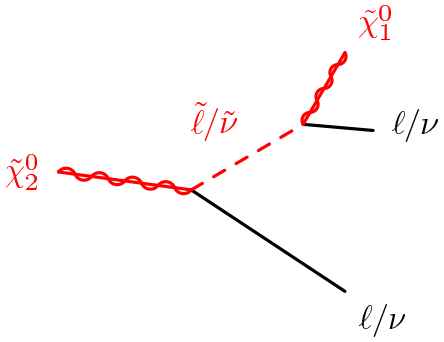

(b) $\tilde{\chi}_2^0$ decaying into a $\tilde{\ell}/\tilde{\nu}$ and ℓ/ν.

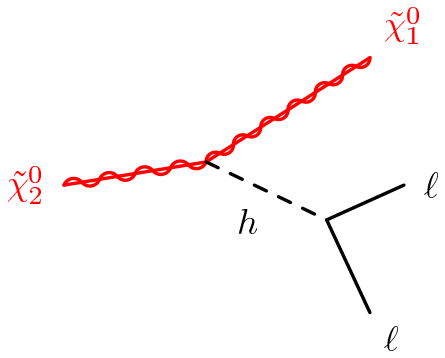

(c) $\tilde{\chi}_2^0$ decaying into a h boson and the LSP.

Figure 2.6: Diagrams for the electroweak SUSY production of neutralinos with leptons in the final state. The symbols $\tilde{\ell}$ and ℓ refer to $\tilde{e}/\tilde{\mu}/\tilde{\tau}$ and $e/\mu/\tau$, respectively.

2.2.2 *R*-Parity SUSY

Some terms in the "unconstrained" MSSM Lagrangian can lead to a violation of the baryon and lepton symmetries, unlike in the SM, where this was an accidental symmetry. A way to avoid these terms is to impose a discrete symmetry on the MSSM, under which all SM fields are even and all superpartners are odd. This symmetry is referred to as R-parity [33], and can be defined as a multiplicatively conserved quantum number

$$R = (-1)^{3(B-L)+2s}, \tag{2.19}$$

where B, L, s correspond the baryon, lepton and spin quantum numbers, respectively.

If the theory is R-parity conserving, SM particles have $R = 1$ and sparticles have $R = -1$. If R-parity conservation is imposed on MSSM models, the mixing between particles and sparticles is not allowed and at every interaction vertex the number of sparticles must be even. This has the effect that the Lightest Supersymmetric Particle (LSP) is stable and all other heavier sparticles can decay only to odd numbers of it and that all sparticles must be produced in pairs.

Dark Matter

In R-Parity conserving SUSY models, the LSP is stable and can be neutral and weakly interacting, therefore, fulfilling all features of a WIMP, which makes for a possible dark matter candidate. The fact that the LSP is weakly interacting means that it will appear as missing energy at the LHC.

In the analysis presented in this thesis, only R-parity conserving SUSY models are considered, where the lightest neutralino ($\tilde{\chi}_1^0$) is considered as the LSP.

2.2.3 Simplified Supersymmetric Models

A simplistic approach for SUSY breaking models is to focus on one or more SUSY production processes and their decay chain, which has the advantage of considering the minimal particle content necessary to reproduce such events. This approach is referred to as a "simplified" model.

Figure 2.7 shows a schematic representation of a simplified model process, where the red arrows highlight the decay chain of interest, in this case is $q\bar{q}' \rightarrow W^{\pm *} \rightarrow \tilde{\chi}_1^{\pm}\tilde{\chi}_2^0$ decaying into LSP with 100% branching ratio, where the out of all the allowed SUSY decays.

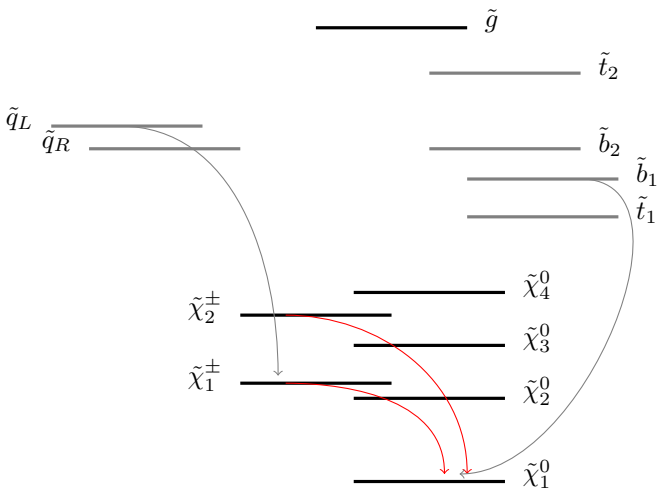

Figure 2.7: SUSY production process, with a simplified model decay chain highlighted by the red arrows.

Only simplified models for the associated production of the lightest chargino ($\tilde{\chi}_1^\pm$) and the second-lightest neutralino ($\tilde{\chi}_2^0$) are considered in this analysis, which are amongst some of the electroweak gaugino (also referred to as "electroweakino") pair-production processes that can lead to three leptons and missing transverse energy in the final state. In most of the MSSM parameter space $\tilde{\chi}_1^\pm\tilde{\chi}_2^0$ production has a higher cross section with respect to other EWK pair production modes such as which can lead to three leptons in the final state. The masses of the relevant particles in the decay chain are the only free parameters in these models. The following assumptions are made on the simplified models considered in this analysis: the $\tilde{\chi}_1^\pm$ and $\tilde{\chi}_2^0$ consist purely of the wino component and are degenerate in mass; the $\tilde{\chi}_1^0$ consists purely of the bino component; and in all cases, the squark and gluino masses are set as as high as a few hundreds of TeV.

The different scenarios for the decay of $\tilde{\chi}_1^\pm$ and $\tilde{\chi}_2^0$ are classified according to the particles (or sparticles) participating in an intermediate step of the decay chain. Four simplified models are explored in the analysis discussed in this thesis and are described in the following.

Simplified Models with Three Lepton Final States via Sleptons

In this simplified model scenario, the left-handed charged sleptons and sneutrinos are assumed to be light, whereas the right-handed charged sleptons are considered to be very heavy. Thus, the wino-like chargino and neutralino will dominantly decay through left-handed charged sleptons or sneutrinos as shown in the diagram in Figure 2.8. For these

models, the masses of $\tilde{\chi}_1^{\pm}, \tilde{\chi}_2^0, \tilde{l}_L, \tilde{\nu}, \tilde{\chi}_1^0$ are the free parameters. Degeneracy of $m_{\tilde{\ell}_L,\tilde{\nu}}$ for various flavours is assumed for simplicity, these are set such that $m_{\tilde{\ell}_L} = (m_{\tilde{\chi}_1^0} + m_{\tilde{\chi}_2^0})/2$. Both the branching ratio of the $\tilde{\chi}_1^{\pm}$ into $\ell\tilde{\nu}$ and the branching ratio into $\tilde{\ell}_L\nu$ are set equal to 50%. Also, both the branching ratio of the $\tilde{\chi}_2^0$ into $\ell\tilde{\ell}_L$ and the branching ratio into $\tilde{\nu}\nu$ are set equal to 50%.

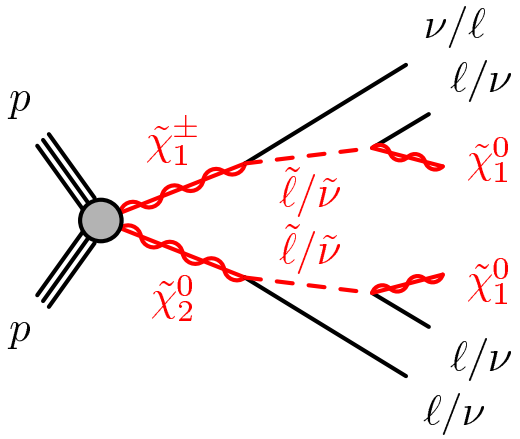

Figure 2.8: The diagrams for the $\tilde{\ell}_L$-mediated simplified models of the direct production of $\tilde{\chi}_1^{\pm}\tilde{\chi}_2^0$ studied in this analysis. The symbols $\tilde{\ell}$ and ℓ refer to $\tilde{e}/\tilde{\mu}/\tilde{\tau}$ and $e/\mu/\tau$, respectively.

Simplified Models with Three Lepton Final States via WZ

In the second simplified model scenario, all sleptons and sneutrinos are assumed to be heavy, and the $\tilde{\chi}_1^{\pm}$ and $\tilde{\chi}_2^0$ decay via $W^{(*)}$ and $Z^{(*)}$ bosons, respectively, with a branching fraction of 100%, leading to three leptons and missing transverse energy in the final state. The decay chain for this process is shown in the diagram in Figure 2.9.

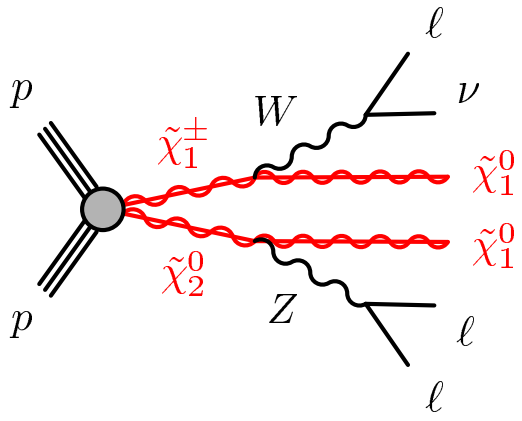

Figure 2.9: The diagrams for the WZ-mediated simplified models of the direct production of $\tilde{\chi}_1^{\pm}\tilde{\chi}_2^0$ studied in this analysis. The symbols ℓ refer to $e/\mu/\tau$.

Simplified Models with three lepton final states via staus

In the third simplified model considered for this analysis, the first- and second-generation sleptons and sneutrinos are assumed to be heavy, so that the $\tilde{\chi}_1^{\pm}$ and $\tilde{\chi}_2^0$ can decay into tau leptons with a 50% branching fraction via $\tilde{\tau}$ or $\tilde{\nu}$ with degenerate masses $m_{\tilde{\nu}} = m_{\tilde{\tau}} = (m_{\tilde{\chi}_1^0} + m_{\tilde{\chi}_2^0})/2$. For these models, the masses of $\tilde{\chi}_1^{\pm}, \tilde{\chi}_2^0, \tilde{\tau}_L, \tilde{\nu}_\tau, \tilde{\chi}_1^0$ are the free parameters.

The diagram representing the decay chain for this model is shown in Figure 2.10.

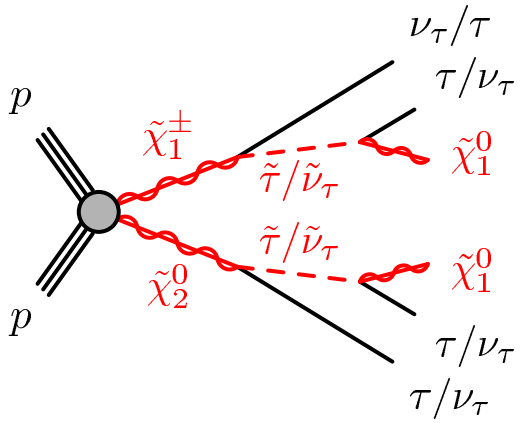

Figure 2.10: Diagram for the $\tilde{\tau}_L$-mediated simplified models of the direct production of $\tilde{\chi}_1^{\pm}\tilde{\chi}_2^0$ studied in this analysis.

Simplified Models with Three Lepton Final States via Wh

In the final simplified model scenario considered in this analysis, all sleptons and sneutrinos are assumed to be heavy, and the wino-like $\tilde{\chi}_1^{\pm}$ and $\tilde{\chi}_2^0$ decay via W and lightest Higgs boson (h), respectively, with a branching fraction of 100%. The Higgs boson considered

in this model is SM-like, meaning it has a mass of 125 GeV and decays into other SM particles with SM branching ratios.

The decay chain is shown on the diagram in Figure 2.11.

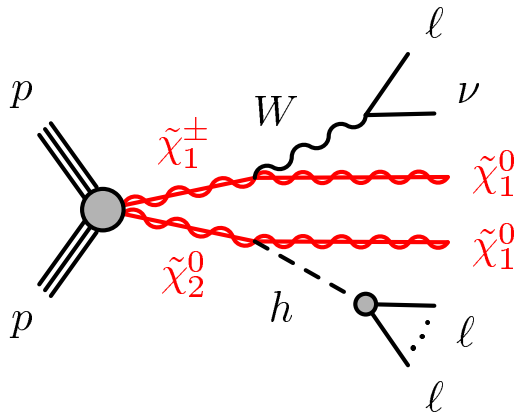

Figure 2.11: The diagrams for the Wh-mediated simplified models of the direct production of $\tilde{\chi}_1^{\pm}\tilde{\chi}_2^0$ studied in this analysis. The dots in the figure depict possible additional decay products of the lightest Higgs boson decaying via intermediate $\tau\tau$, WW or ZZ states. The symbols ℓ refer to $e/\mu/\tau$.

2.2.4 Phenomenological MSSM

The phenomenological MSSM (pMSSM) [30] is defined by making the following assumptions on the phenomenology of the free parameters of the MSSM theory: all the soft SUSY-breaking parameters are real and therefore there is no new source of CP-violation [34] generated; the matrices for the sfermion masses and for the tri-linear couplings are all diagonal (no flavour changing neutral currents at tree level); the soft SUSY-breaking masses and tri-linear couplings of the first- and second-generation sfermions are the same at low energy. Making these three assumptions will lead to the free parameters summarised in Table 2.5.

The Electroweak Sector

The electroweak sector within the pMSSM is mainly characterised by the following parameters [27]: the $U(1)$ gaugino (bino) mass parameter, M_1; the $SU(2)$ gaugino (wino) mass parameter, M_2; the higgsino mass parameter, μ; and the ratio of the VEVs of the two Higgs doublets, denoted as $\tan\beta$ in Table 2.5.

In the scenarios explored for this analysis, the pMSSM parameters are tuned in such a way that direct electroweak production is the dominant SUSY process. This is achieved

by setting the masses of the coloured sparticles (gluinos and squarks), the CP-odd Higgs boson (m_{A^0}), and the left-handed sleptons to high values at the TeV scale. The lightest Higgs mass is given by $m_h = m_Z cos^2 2\beta + \delta t^2$, where δt is a loop contribution from top quarks and stop squarks. Therefore, the mass of the SM-like Higgs can be tuned to 125 GeV (consistent with the mass of the observed Higgs boson [16, 17]) using mixing in the stop sector.

Figure 2.12 shows the mass hierarchy of the electroweakinos in three different MSSM scenarios, which are governed by $\tan\beta$, the gaugino mass parameters M_1 and M_2, and the higgsino mass parameter μ.

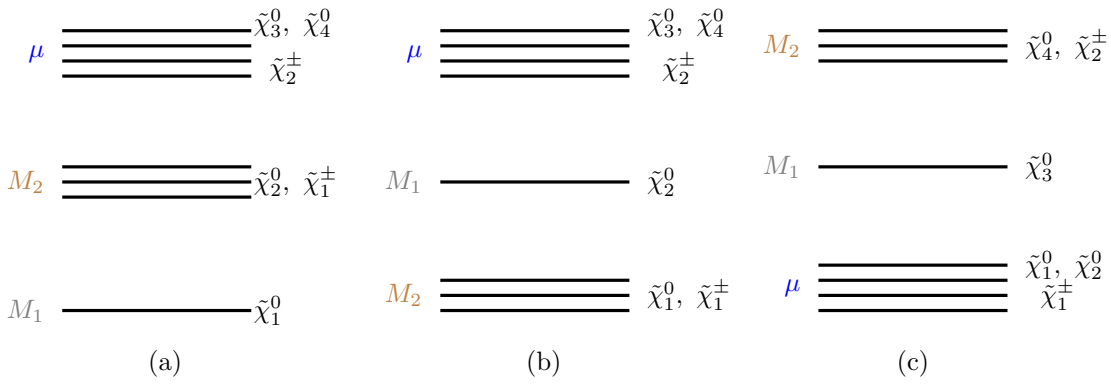

Figure 2.12: Three possible electroweak SUSY mass spectra and their dependency on the values of the parameters M_1 , M_2 and μ .

For instance, if $M_1 < M_2 < \mu$, case shown in Figure 2.12(a), the corresponding composition of the $\tilde{\chi}_1^0$ is driven by M_1 (bino-like) and the composition of $\tilde{\chi}_1^\pm$ and $\tilde{\chi}_2^0$ is driven by M_2 (wino-like). In this case, the dominant electroweakino production process with three leptons in the final state is $pp \to \tilde{\chi}_1^\pm \tilde{\chi}_2^0$. For cases shown in Figure 2.12(b)-(c), searches with three leptons in the final states offer less sensitivity than in case (a) because of the mass difference between $\tilde{\chi}_1^\pm$ and $\tilde{\chi}_2^0$.

The pMSSM scenarios described in the following paragraphs are parametrised in the μ–M_2 phase space and classified into three groups based on the masses of the right-handed sleptons.

pMSSM $\tilde{\ell}_R$

In this scenario, the right-handed sleptons ($\tilde{e}_R, \tilde{\mu}_R, \tilde{\tau}_R$) are degenerate in mass with a value set at midpoint between the LSP and next-to-lightest neutralino masses: $m_{\tilde{\ell}_R} = (m_{\tilde{\chi}_1^0} + m_{\tilde{\chi}_2^0})/2$. Setting the parameter $\tan\beta = 6$ yields comparable $\tilde{\chi}_2^0$ branching ratios

into each slepton generation.

There are many different EWK production modes available for this model, the dominant ones are shown in Figure 2.13, where process (a) has the highest cross section out of all the production modes that can lead to three-lepton final states, although, in some areas of the parameter space, sub-processes involving heavier sparticles can be important.

The $\tilde{\chi}_1^\pm$ decays predominantly via a W boson when kinematically allowed and to $\tilde{\tau}$ otherwise. The $\tilde{\chi}_2^0$ decays occur via $\tilde{\ell}\ell$, $\tilde{\chi}_1^0 h$ or $\tilde{\tau}\tau$.

To probe the sensitivity for different $\tilde{\chi}_1^0$ compositions, three values of M_1 are considered: 100 GeV (bino-like), 140 GeV (bino- and wino- like) and 250 GeV (higgsino-like).

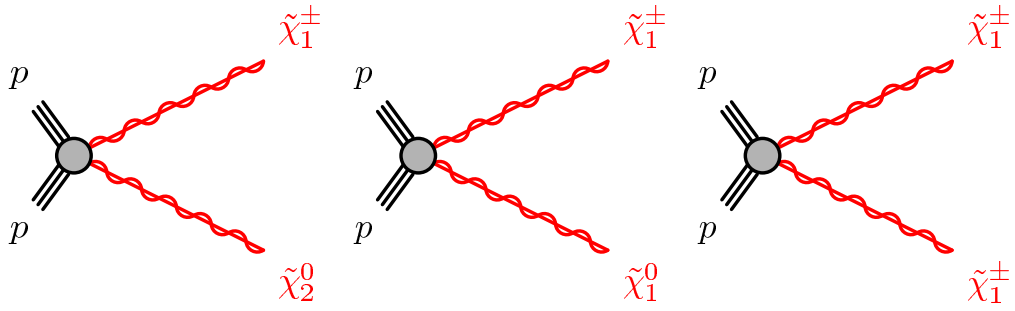

(a) $\tilde{\chi}_1^\pm$-$\tilde{\chi}_2^0$ pair production. (b) $\tilde{\chi}_1^\pm$-$\tilde{\chi}_1^0$ pair production. (c) $\tilde{\chi}_1^\pm$-$\tilde{\chi}_1^\pm$ pair production.

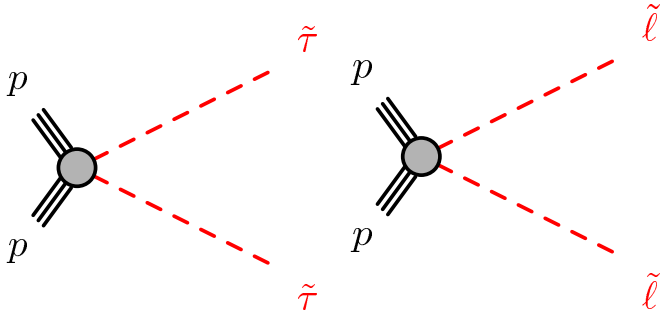

(d) $\tilde{\tau}$-$\tilde{\tau}$ pair production. (e) $\tilde{\ell}$-$\tilde{\ell}$ pair production.

Figure 2.13: Dominant diagrams for the electroweak SUSY production in the pMSSM model via $\tilde{\ell}_\mathrm{R}$. The symbols $\tilde{\ell}$ refer to $\tilde{e}/\tilde{\mu}/\tilde{\tau}$.

pMSSM $\tilde{\tau}_\mathrm{R}$

In the next pMSSM scenario, the selectrons and smuons are heavy, the $\tilde{\tau}_\mathrm{R}$ mass is set to $m_{\tilde{\tau}_\mathrm{R}} = (m_{\tilde{\chi}_1^0} + m_{\tilde{\chi}_2^0})/2$ and $\tan\beta = 50$, so that the decays via right-handed staus dominate. The parameter M_1 is set to 75 GeV resulting in a bino-like composition of $\tilde{\chi}_1^0$. There are four main production modes in this model, shown in Figure 2.14, where generally processes (b) and (d) have the highest cross section. For the purpose of the three lepton analysis

presented here, the production modes with the highest cross sections are (a) and (d). $\tilde{\chi}_1^\pm$ decays predominantly via a W boson when kinematically allowed and to $\tilde{\tau}$ otherwise. $\tilde{\chi}_2^0$ decays are mainly via $\tilde{\tau}\tau$ (where staus will decay to tau leptons and the LSP), with smaller branching ratios into $\tilde{\chi}_1^0 Z$ and $\tilde{\chi}_1^0 h$.

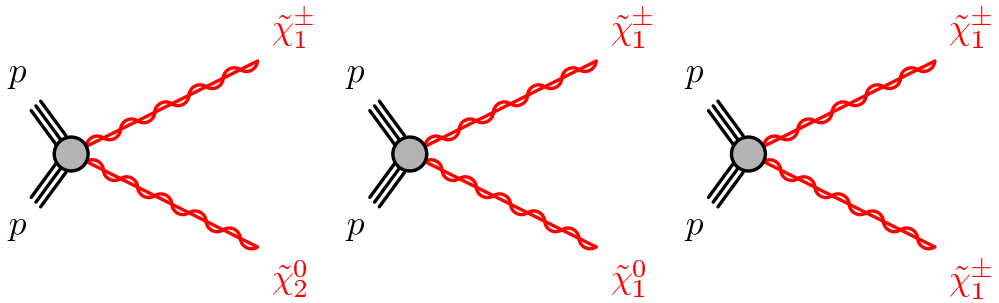

(a) $\tilde{\chi}_1^\pm$-$\tilde{\chi}_2^0$ pair production. (b) $\tilde{\chi}_1^\pm$-$\tilde{\chi}_1^0$ pair production. (c) $\tilde{\chi}_1^\pm$-$\tilde{\chi}_1^\pm$ pair production.

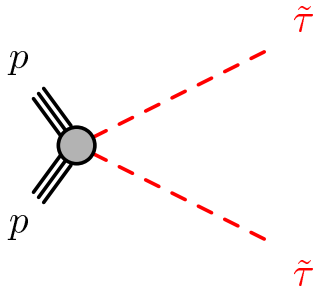

(d) $\tilde{\tau}$-$\tilde{\tau}$ pair production.

Figure 2.14: Dominant production of EWK SUSY processes in the pMSSM model via $\tilde{\tau}_\mathrm{R}$.

pMSSM no $\tilde{\ell}$

The final pMSSM scenario, assumes all sleptons to be heavy (set to 3 TeV) so that decays via W, Z or Higgs bosons dominate. The remaining parameters are set to $M_1 = 50$ GeV and $\tan\beta = 10$. There are three main production modes in this model, shown in Figure 2.15, where processes (a) has the highest cross section. The $\tilde{\chi}_1^\pm$ decays predominantly via a W boson, and the $\tilde{\chi}_2^0$ decays via $\tilde{\chi}_1^0 Z$ or $\tilde{\chi}_1^0 h$.

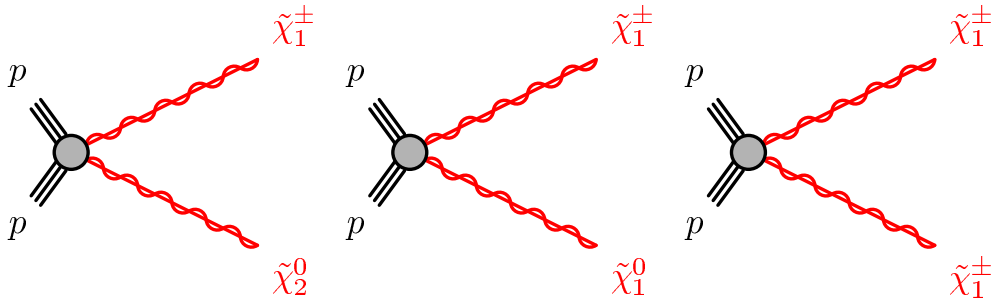

(a) $\tilde{\chi}_1^{\pm}$-$\tilde{\chi}_2^0$ pair production. (b) $\tilde{\chi}_1^{\pm}$-$\tilde{\chi}_1^0$ pair production. (c) $\tilde{\chi}_1^{\pm}$-$\tilde{\chi}_1^{\pm}$ pair production.

Figure 2.15: Dominant production of EWK SUSY processes in the pMSSM model via no-$\tilde{\ell}$.

Chapter 3

The ATLAS detector at the LHC

This chapter provides an overview of the ATLAS experiment at the Large Hadron Collider. The Large Hadron Collider particle accelerator is introduced in Section 3.1, followed by a detailed description of the various components of the ATLAS detector. Finally, a description of the trigger system used by ATLAS to cope with the high LHC event rate is discussed in Section 3.3.

3.1 The Large Hadron Collider

The Large Hadron Collider (LHC) [35] is the largest particle accelerator ever built, achieving the highest energies in proton-proton, lead-proton and lead-lead collisions yet. Situated 100 m underground inside the tunnel previously occupied by the Large Electron Positron Collider (LEP) [36], the LHC consists of a 27 km ring of superconducting magnets and accelerating elements, which support same-charge hadron beams circulating in opposite directions. These beams are forced to collide at four specific points around the ring as shown in Figure 3.1. In these points are located the experiments: LHCb [37], ALICE [38], ATLAS [39] and CMS [40].

The LHC magnetic system consists of 1232 superconducting dipole and 392 quadrupole magnets, with an average magnetic field of 8.3 T which are kept at a temperature of 1.7 k. The purpose of the dipole magnets is to bend the beam and keep it in circular motion while the purpose for the quadrupole magnets (and a few higher-moment magnets) is to keep the beam focused as it gets accelerated around the ring. There are two transfer tunnels (each around 2.5 km long) which connect the LHC to the rest of the CERN accelerator complex that acts as an injector.

Proton-proton collisions at the LHC begin with the extraction of protons from hydrogen

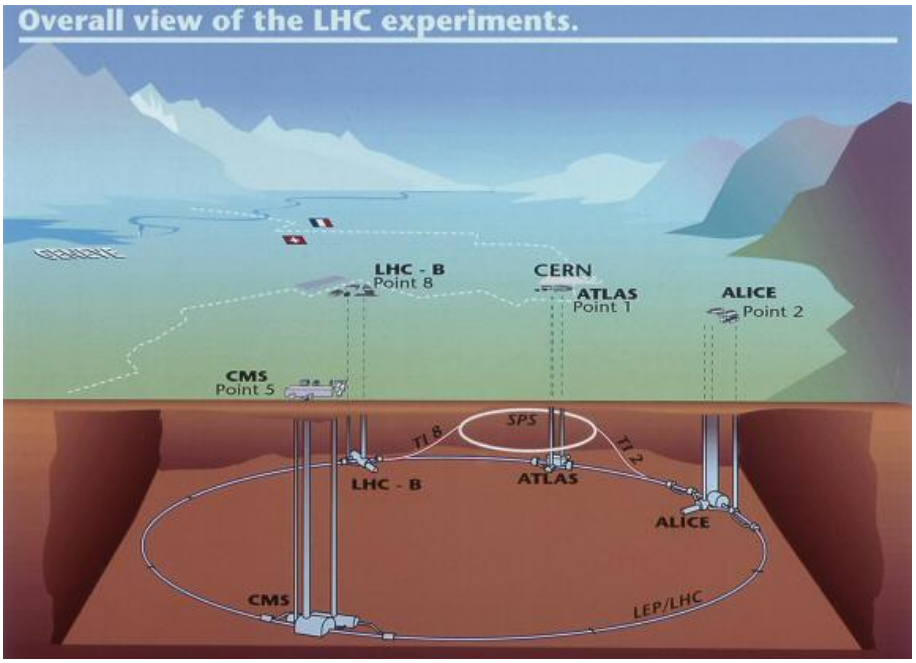

Figure 3.1: A schematic view of the LHC with the four main experiments [41].

gas, from which the electrons are stripped using an electric field, followed by acceleration and injection into successively larger storage rings. Figure 3.2 shows the acceleration and injection process, beginning with the extracted protons being accelerated to an energy of 50 MeV by a linear accelerator (LINAC2) and then further accelerated to 1.4 GeV by the Proton Synchrotron Booster (PSB). The beam then enters the Proton Synchrotron (PS) where its energy is increased to 25 GeV and finally gets accelerated up to an energy of 450 GeV by the Super Proton Synchrotron (SPS). The resulting beam is split into two parts which are accelerated around the LHC in opposite directions. The acceleration to the collision energy is carried out by eight superconductive RF cavities located at four different places around the the LHC itself. These RF cavities also provide longitudinal beam focusing to maintain the bunch structure within the beam.

Performance of the LHC

The "luminosity" of the LHC ($\mathcal{L}$) is defined as

$$\mathcal{L} = f \frac{n_b N_1 N_2}{4\pi\sigma_x\sigma_y}, \tag{3.1}$$

where f is the revolution frequency of the bunches, N_1 and N_2 the number of bunches per beam, n_b the amount of particles per bunch and σ_x and σ_y the physical size of the beams at the interaction point. The luminosity is related to the total number of collisions

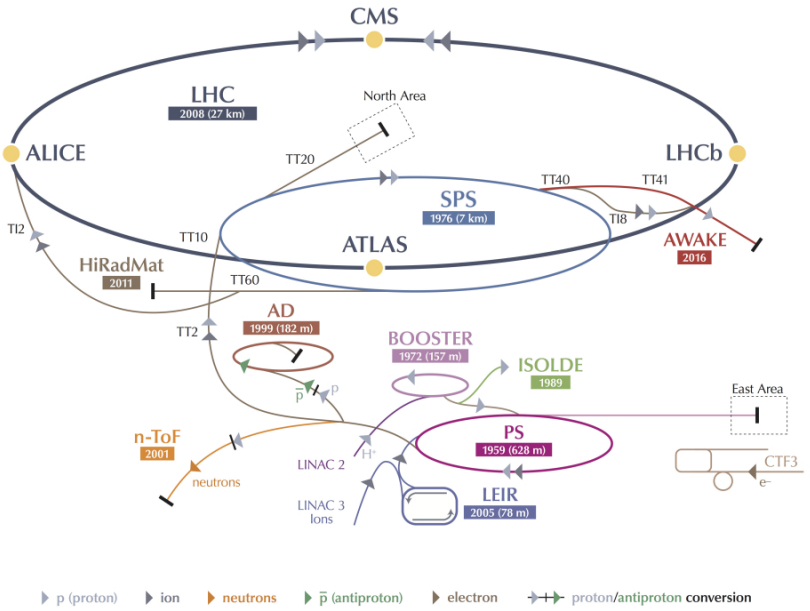

Figure 3.2: The CERN accelerator complex [42].

generated in the LHC collisions, given by

$$N_{event} = \mathcal{L}\sigma_{event} \tag{3.2}$$

where σ_{event} is the cross section for the process under study.

The nominal design of the LHC called for an energy of 7 TeV per beam corresponding to a centre-of-mass-energy of up to $\sqrt{s} = 14$ TeV at a frequency of 40 MHz. Inside the LHC, 2808 proton bunches of up to 10^{11} protons will collide every 25 ns to provide 14 TeV proton-proton collisions at a design peak luminosity of 10^{34} cm^{-2}s^{-1}. These running conditions are, however, expected to be achieved only at the start of the second run of the LHC in 2015. The luminosity for the first run of the LHC (Run1) increased over the years, starting from a centre-of-mass-energy of $\sqrt{s} = 900$ GeV in 2009, to $\sqrt{s} = 7$ TeV during 2010-2011 and finally to $\sqrt{s} = 8$ TeV at the beginning of 2012. This was achieved by improving with time several of the LHC parameters, such as increasing the number of protons per bunch, reducing the physical size of the bunch, and many more [35].

3.2 The ATLAS detector

ATLAS is one of two general-purpose experiments recording LHC collisions, designed to study many different physics signatures both to prove the validity of the SM, like searching for the Higgs boson, and to search for physics beyond the SM. It measures the particles and energy of particles produced as a result of the proton-proton collisions at the LHC with

high precision, offering a nearly 4π solid angle coverage which provides a full description for every collision.

Throughout this thesis, the standard ATLAS coordinate system is adopted for the spatial description of the various detector components and in kinematic measurements of physics processes. This coordinate system is defined by taking the beam direction as the z-axis, and the x-y plane as transverse to the beam direction. The azimuthal angle, ϕ, is measured around the beam axis and the polar angle, θ. A spacial coordinate is introduced to describe the angle of a particle with respect to the beam axis, this is known as pseudo-rapidity and is defined as $\eta \equiv -ln(tan(\theta/2))$. ATLAS (25 m high and 44 m long) has a forward-backward symmetric cylindrical geometry with respect to the interaction point. Therefore, detector components are described as being part of the barrel if they are in the central region of pseudorapidity or part of the end-caps if they are in the forward regions.

The overall ATLAS detector layout with its components is shown in Figure 3.3. ATLAS

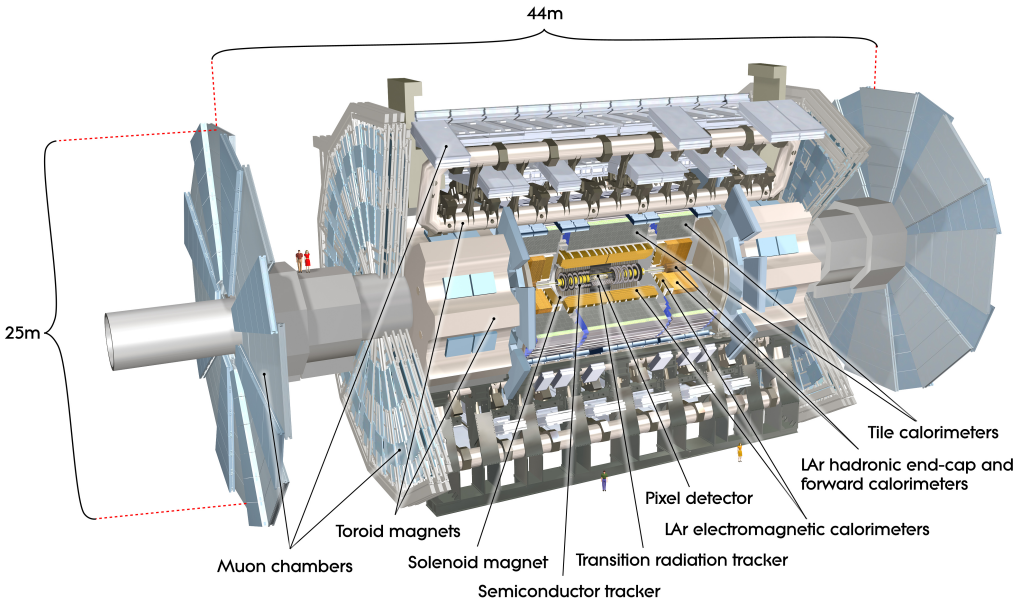

Figure 3.3: A cut-away view of the ATLAS detector [43].

innermost layer is the so-called "Inner Detector" (ID) which performs a fine grained tracking system for charged particles, and consists of a pixel and silicon micro-strip tracker and a transition radiation tracker. It is enclosed by a thin superconducting solenoid providing a magnetic field of 2 T which allows for measurement of the transverse momentum of charged particles. The following layers correspond to electromagnetic and hadronic calorimeters that jointly allow precise energy measurements of photons, electrons, and hadronic jets. The outermost layer corresponds to the Muon Spectrometer (MS), which

is embedded in a toroidal field, and designed to measure the position and momentum of muons.

The main ATLAS detector performance goals are summarised in Table 3.1.

Table 3.1: General performance goals of the ATLAS detector [39]. Pseudorapidity range used for the trigger system is specified in brackets if different to the range used for offline measurements. The units for E and p_{T} are in GeV.

System	Sub-detector	Resolution	Pseudorapidity Coverage
Tracking	ID	$\frac{\sigma_{p_{\mathrm{T}}}}{p_{\mathrm{T}}} = 0.05\%\ p_{\mathrm{T}} \oplus 1\%$	$\lvert\eta\rvert < 2.5$
	MS	$\frac{\sigma_{p_{\mathrm{T}}}}{p_{\mathrm{T}}} = 10\%$ at $p_{\mathrm{T}} = 1$ TeV %	$\lvert\eta\rvert < 2.7$ ($\lvert\eta\rvert < 2.4$)
Calorimetry	Electromagnetic	$\frac{\sigma_E}{E} = \frac{10\%}{\sqrt{E}} \oplus 0.7\%$	$\lvert\eta\rvert < 3.2$ ($\lvert\eta\rvert < 2.5$)
	Hadronic (central)	$\frac{\sigma_E}{E} = \frac{50\%}{\sqrt{E}} \oplus 3\%$	$\lvert\eta\rvert < 3.2$
	Hadronic (forward)	$\frac{\sigma_E}{E} = \frac{100\%}{\sqrt{E}} \oplus 10\%$	$3.1 < \lvert\eta\rvert < 4.9$

The various sub-detector systems are described in the following paragraphs.

3.2.1 Magnet System

The ATLAS magnet system (22 m in diameter and 26 m long) is formed by a thin central superconducting solenoid surrounding the ID system, and three large outer superconducting toroids arranged around the calorimeters that provide the field for the MS. These key components of the detector generate the bending power for the momentum measurement of charged particles. Figure 3.4 provides an overview of these components, which are discussed in the following.

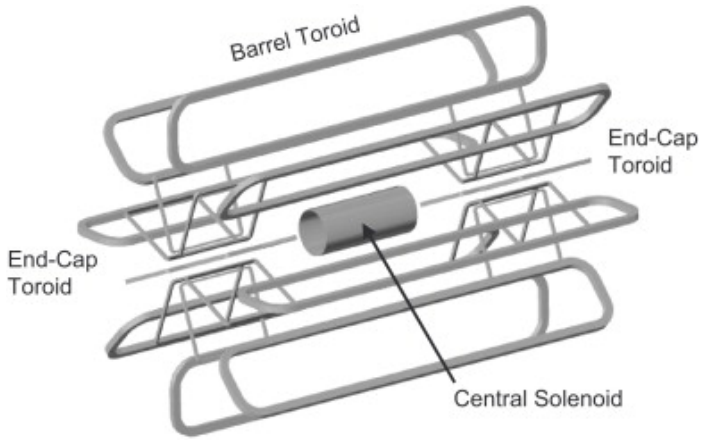

Figure 3.4: Schematic view of the layout of the four superconducting magnets forming the ATLAS magnetic system [44].

Central Solenoid

The central solenoid magnet is designed for bending charged particles going through the inner detector, and its geometry also takes into account the operational constrains of the calorimeters. This 2.3 m diameter and 5.3 m long component is aligned with the beam axis and provides a 2 T axial magnetic field, which allows for very accurate momentum measurements of charged particles with momenta up to 100 GeV [44]. The electromagnetic calorimeter of the experiment is situated outside this solenoid, which means that the winding must be as transparent as possible for the particles traversing the detector.

Barrel and End-cap Toroids

The toroid magnet system is a cylindrical volume surrounding the calorimeters. It consists of a long barrel and two end-caps toroids, each with eight superconducting coils (see Figure 3.4) . The toroidal system is surrounded by muon detectors. The barrel and two end-cap toroids produce a toroidal magnetic field of approximately 0.5 T and 1 T for the muon detectors in the central and end-cap regions, respectively. The toroidal magnetic fields enable the momentum measurement of low-p_{T} muons by a bending force acting in the θ-direction.

3.2.2 Inner Detector

The inner detector is the part of the ATLAS detector closest to the beam pipe and provides a tracking system for momentum and vertex measurements of charged particles. When a charged particle traverses the ID it will experience a force due to the 2 T magnetic field surrounding it, acting orthogonally to the direction of motion of the particle, causing its trajectory to curve. It is possible to calculate the momentum of a charged particle once this curvature is measured.

The ID is divided into three independent concentric sub-detectors: a pixel detector, the innermost sub-detector, consisting of three silicon pixel layers; the SemiConductor Tracker (SCT) or "silicon strip detector" as the central layer of the ID; and surrounding all ID sub-detectors is the Transition Radiation Tracker (TRT). Combining these three sub-detectors gives a tracking acceptance in the region $|\eta| < 2.5$ for tracks with $p_{\mathrm{T}} > 0.5$ GeV [45].

The following paragraphs provide a brief description of the ID sub-systems shown in Figure 3.5.

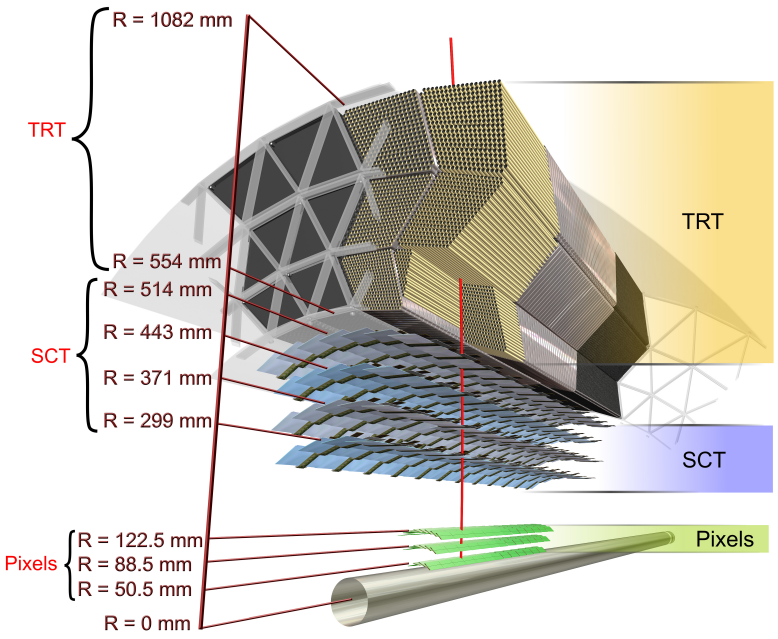

Figure 3.5: Diagram of the ATLAS inner detector and its components [46].

Silicon Pixel Tracker

The pixel detector [47] is equipped with 1750 identical sensorchip-hybrid modules, each covering an active area of 16.4×60.8 mm. The total number of modules correspond to approximately 80 million semiconductor silicon pixels ($50 \times 400\ \mu m^2$ rectangular segments of silicon sensors), to cope with high rate luminosity of the ATLAS detector. This is achieved by reading out every pixel with an independent electronics channel.

The silicon pixel detector is inside a cylindrical envelope of 48.4 cm diameter and approximately 6.2 m length providing a pseudorapidity coverage of $|\eta| < 2.5$. Figure 3.5 shows the composition of the pixel detector as three concentric barrel layers of radii: 50.5 mm (the so-called b-layer), 88.5 mm and 122.5 mm. It also consists of a total of six disk layers, three at each forward region. Particles will go through all three barrel layers of the pixel detector, making hits in each of them as they traverse the ID. The 2×3 end-cap disks are mounted perpendicularly to the beam axis to track the momentum of charged particles at high η. The main feature of the pixel detector is its fine granularity [1] which is essential for high resolution measurement and precise vertex reconstruction.

[1] The granularity is the size of each pixel, which determines the resolution of the detector since the finer granularities the more "detection area" giving a more accurate position.

SemiConductor Tracker

The SCT [45], the second innermost system in the ID, designed to measure four precision space points (corresponding to eight silicon layers) on the track of a charged particle over a range $|\eta| < 2.5$, which is mainly useful for precise momentum reconstruction, with intrinsic resolutions per module of 17 νm in the $R - \phi$ direction and 580νm in the z direction.

The SCT consists of 4088 modules of semi-conducting silicon micro-strip detectors arranged in four concentric barrel layers (as shown in Figure 3.6) with radii ranging from 299 mm to 514 mm and two end-cap layers. The silicon-strip sensors are read out by radiation-hard front-end chips, each chip reading out 128 channels. Due to the SCT larger radius from the beam pipe than the pixel detector, there is a reduced particle density expected upon the SCT which allows for a smaller pixel density (coarser granularity) to maintain the same levels of performance while using ∼6.3 million readout channels (∼ 2 million fewer than the pixel detector).

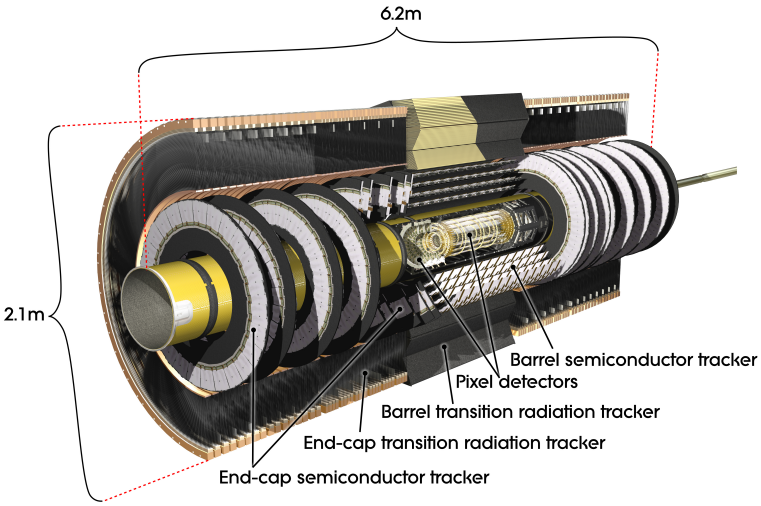

Figure 3.6: Schematic image of the sub-detectors within the ID tracker [46].

Transition Radiation Tracker

The TRT [48] is the outermost component of the ID which utilises layers of gaseous straw tube elements (4 mm in diameter) and transition radiation material. As a charged particle goes through the TRT it will ionise the gas (a mixture of xenon, carbon dioxide and oxygen) inside the straw tubes. It has an average of 36 hits per track in the central region, providing continuous tracking to enhance the pattern recognition and improve the momentum resolution over the pseudorapidity range $|\eta| < 2.0$, important feature for electron identification [49]. This design is complementary to the pixels detectors,

and aims to improve the p_{T} resolution for particles with longer track length. It also provides particle identification capability through the detection of transition radiation X-ray photons generated by high velocity particles traversing through various materials with different dielectric constants.

The TRT barrel section is arranged in three concentric layers each with 32 modules jointly containing approximately 50 000 straws of 1.44 m length in total, which are aligned parallel to the beam direction with independent readout at both ends. Each of the two end-cap sections are divided into 14 wheels, with around 320 000 straws that run in the R-direction. The transition radiator material surrounding the straws in the barrel (end-caps) consists of polypropylene fibres (polypropylene foils).

3.2.3 Calorimeter System

The ATLAS calorimeters, illustrated in Figure 3.7, consist of detectors with full ϕ-symmetry and η coverage of $|\eta| < 4.9$ around the beam axis. The inner layer corresponds to the electromagnetic (EM) calorimeter and the outer layer corresponds to the hadronic calorimeter.

The EM calorimeter is composed by one barrel (*LAr electromagnetic barrel*) and two end-cap (*EMEC*) sections using Liquid Argon (LAr) as sensing element, where the showers in the Argon liberate electrons that are collected and then recorded, these sections also referred to as "LAr calorimeters" [50].

The hadronic calorimeter contains one barrel (*Tile barrel* and *'Tile extended barrel*) and two end-cap (*HEC*) sections. The sensors used for the barrel sections of the hadronic calorimeter are tiles of scintillating plastic, which cause the plastic to emit light that gets detected and then recorded, these sections are known as "tile calorimeters" [39]. The end-cap sections use LAr as sensing element.

A LAr forward calorimeter (*FCal*) is also part of the calorimeter system, which aims to cover the region closest to the beam.

A brief overview of the two calorimeter sensing elements is provided below.

Liquid Argon Calorimeters: The LAr EM calorimeter covers a pseudorapidity range of $|\eta| < 1.475$ and $1.375 < |\eta| < 3.2$, with one barrel and two end-cap regions, respectively.

The LAr end-cap HEC covers a pseudorapidity range of $1.5 < |\eta| < 3.2$. It consists of two independent wheels for each end-cap, located directly behind the end-cap EM

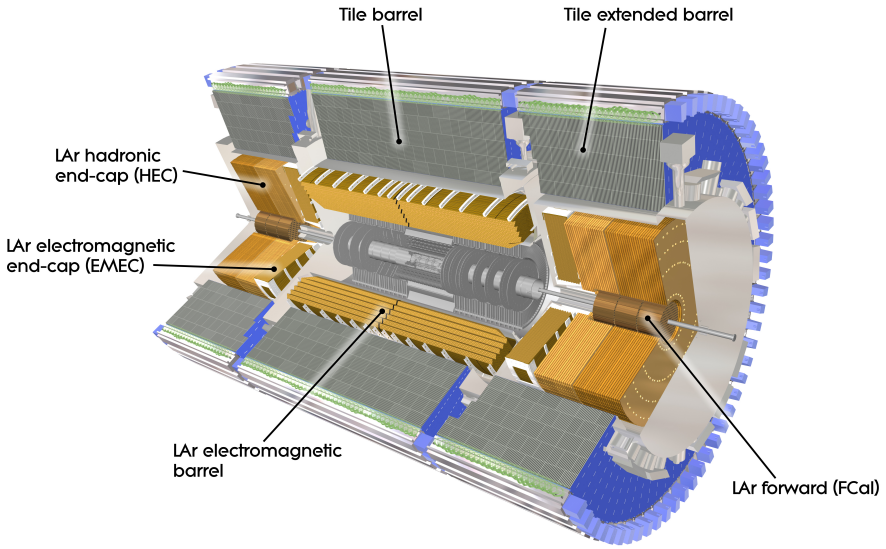

Figure 3.7: A cut-away view of the ATLAS electromagnetic and hadronic calorimeter layers [51].

calorimeter and sharing the same LAr cryostat. Its coverage overlaps with that of the forward calorimeter to ease transitions between regions.

The LAr FCal covers a pseudorapidity range of $3.1 < |\eta| < 4.9$ and it is formed by one EM layer with copper as passive material and two hadronic layers which use tungsten as absorbers.

These three sub-detectors share the same read-out electronics (182 468 channels in total) that can be individually calibrated.

Tile Calorimeter: The tile calorimeter is the central ATLAS Hadronic Calorimeter, surrounding the EM calorimeter system. Its main purpose is to provide hadronic energy measurements. This calorimeter is built out of steel and scintillating tiles coupled to optical fibres which are read out by photo-multipliers. It is is divided into three cylinders with an inner radius of 2.28 m and an outer radius of 4.23 m: a central barrel part that is 5.64 m long covering a region $|\eta| < 1.0$ and two "extended barrel" parts, which are 2.91 m long and cover the pseudorapidity range $0.8 < |\eta| < 1.7$. Each cylinder consists of 64 modules spread in ϕ. Radially, each module is further segmented in three layers with a cell (smallest calorimeter section) granularity of $\Delta\eta \times \Delta\phi = 0.1 \times 0.1$ for the two inner most layers and $\Delta\eta \times \Delta\phi = 0.2 \times 0.1$ for the outermost layer.

3.2.4 Muon Spectrometer

The MS [52] is the outermost part of the ATLAS detector which surrounds the calorimeters and measures muon paths to determine their momenta with high precision (specified in Table 3.1). The conceptual layout of the muon spectrometer is shown in Figure 3.8.

Its design is based on the magnetic deflection of muon tracks due to large superconducting air-core toroid magnets and high-precision tracking chambers.

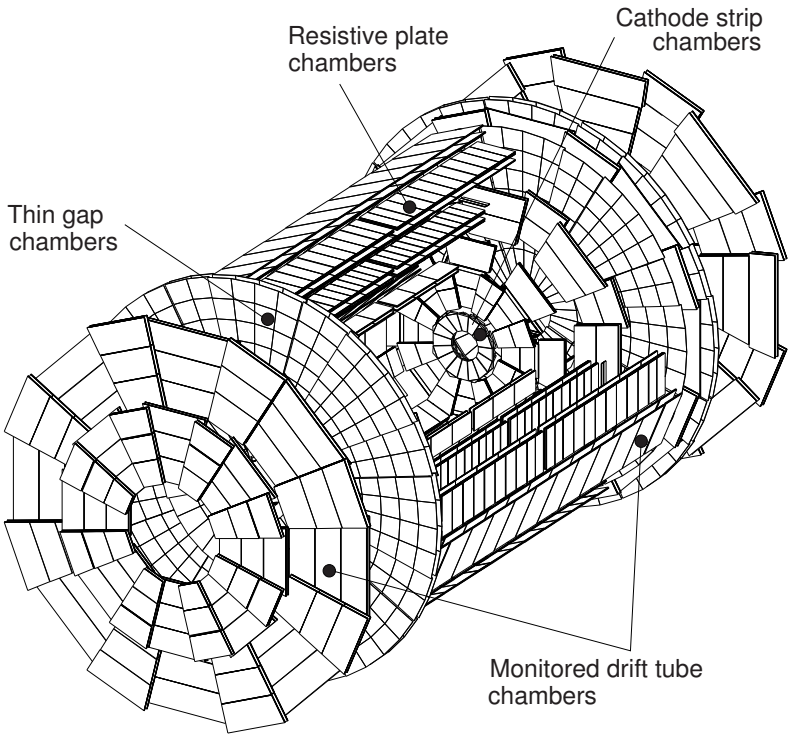

Figure 3.8: The ATLAS muon system [39].

The bending of the track is achieved by utilising one large barrel toroid to cover the rapidity region $|\eta| \leq 1.4$ and two end-cap magnets covering the rapidity regions $1.6 < |\eta| < 2.7$ inserted at both ends of the barrel toroid. In the barrel region, the toroidal field is produced by eight very large superconducting coils arranged in an open geometry, with a B-field varying from 0.5 to 2 T.

Tracks are measured using chambers arranged in three cylindrical layers around the beam axis in the barrel region; in the transition region ($1.4 < |\eta| < 1.6$) and end-cap regions, the chambers are installed in planes perpendicular to the beam, also in three layers. Over most of the η-range, a precision measurement of the track coordinates in

the principal bending direction of the magnetic field is provided by Monitored Drift Tubes (*MDTs*). At large pseudorapidities, Cathode Strip Chambers (*CSCs*), which are multiwire proportional chambers with cathodes segmented into strip with higher granularity, are used in a pseudorapidity region of $2 < |\eta| < 2.7$ to cope with demanding rates and background conditions.

The use of the Resistive-Plate Chambers (*RPCs*) in the barrel and the Thin-Gap Chambers (*TGCs*) in the end-caps is dedicated to the trigger system, this is described in Section 3.3.

3.3 ATLAS Trigger System

The purpose for the development of the ATLAS trigger system is to reduce the event rate taken from the LHC at 40 MHz bunch crossing[2] to a recordable size of approximately 200 Hz, which corresponds to an average data rate of $\sim$ 300 MB/s. This is achieved by a 3-level system, shown in Figure 3.9, which ensures high acceptance for low-p_{T} particles in the events, thus providing a high efficiency for most physics processes of interest at LHC.

The first level of the trigger system, Level 1 (L1), is a hardware-based system that uses information from the calorimeters and muon sub-detectors. The two subsequent levels: Level 2 (L2) and Event Filter (EF), are software-based systems that use information from all ATLAS sub-detectors, and together form the so-called the High Level Trigger (HLT). Each level refines the decisions made by the previous one and, where necessary, applies additional selection criteria.

The rest of this chapter is dedicated to the description of these three levels used by the ATLAS triggering system.

[2]The collision of two proton bunches is commonly referred to as a "bunch crossing". Most of the protons within each bunch will not interact with each other, therefore, an average for the number of interactions per bunch crossing ($\langle\mu\rangle$) is used.

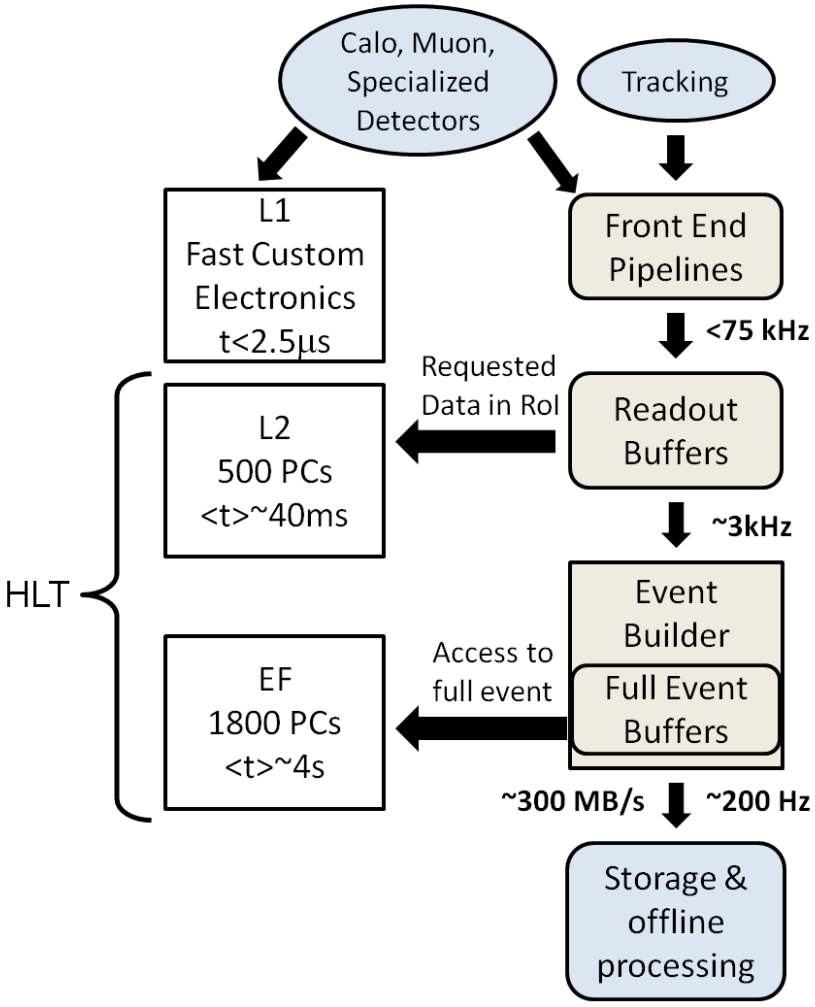

Figure 3.9: A schematic view of the ATLAS trigger system [53].

3.3.1 Level 1 Trigger

The L1 trigger system performs the first selection step by identifying Regions of Interest (ROIs), η-ϕ regions within the detector where its selection process has identified interesting event features. The identified RoIs within the detector will be subsequently investigated by the HLT. The selection made by L1 uses a limited amount of the total detector information in order to make a decision on whether or not to continue processing an event, which effectively reduces the input rate to a maximum of 75 kHz. In order to achieve a latency of less than 2.5 μs (time it would take to reach the front-end electronics), the L1 trigger system is implemented in fast custom electronics. Event data from the sub-detectors are stored in front-end pipeline memories awaiting a decision from the L1 trigger system. If the event passes the L1 trigger selection, the ReadOut Buffers (ROBs) processes the information in the RoIs, which will be passed onto the L2 trigger system.

The RoIs mainly focus on searching for high-p_{T} objects, such as: muons, electrons, photons, jets, and τ- leptons decaying into hadrons; as well as large missing and total transverse energy. Information used to identify high-p_{T} muons is provided to the L1 trigger system by the MS chambers: the RPCs in the barrel ($|\eta| < 1.05$) and the TGCs in the end-caps ($1.05 < |\eta| < 2.4$), which have a time resolution capable of identifying the bunch crossing, a key feature of the L1 trigger. The calorimeter sub-systems provide coarse granularity information used to select electromagnetic clusters, jets, τ-leptons, $E_{\mathrm{T}}^{\mathrm{miss}}$, and large total transverse energy.

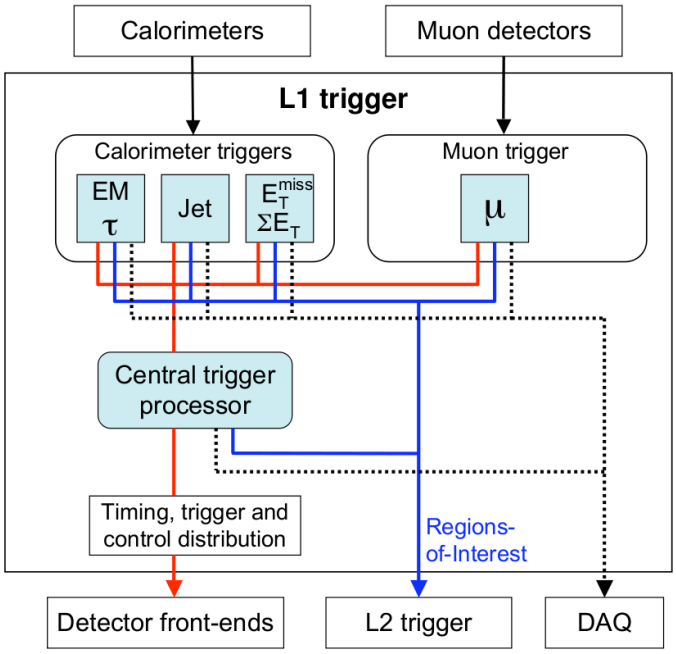

Figure 3.10: A schematic view of the ATLAS L1 trigger system [39]. The overall L1 trigger decision is made by the Central Trigger Processor (CTP), taking input from calorimeters and muon sub-detectors. The paths to the detector front-end electronics, L2 trigger, and data acquisition system are shown from left to right in red, blue and black, respectively.

3.3.2 High Level Trigger

The second trigger level, L2, has a selection seeded by the RoI information provided by the L1 trigger. Unlike L1, the L2 trigger system selection uses fine-granularity information available from all sub-detectors, including the inner detector. Meanwhile, the ROBs store the event data in fragments until the L2 decision is ready. The L2 selection is based on fast custom algorithms processing partial event data within the RoIs identified by the L1 triggers. The L2 trigger system uses processor farms, consisting of around 500 quad-core CPUs, and has an average latency of up to ~ 10 ms [39]. The L2 triggers are designed to

reduce the trigger rate to approximately 3.5 kHz, with an event processing time of about 40 ms, averaged over all events. All event fragments from the ROBs for events accepted by L2 trigger system are passed onto the Event Builder, which assembles all the information, providing full event information to the EF, the final level of the ATLAS trigger system.

The final online selection is performed by software algorithms running on the EF with a farm of processors consisting of 1800 dual quad-core CPUs [45]. The EF is designed to reduce the rate to $\sim$ 200 Hz with an average processing time of $\sim$ 4 s/event. Rejected events are not further processed while accepted events are stored for offline analyses.

Chapter 4

Event Simulation and Reconstruction

Monte Carlo (MC) simulation is used in ATLAS to mimic particle interactions or decays, each of them referred to as an "event". These simulated events provide a tool for comparison and validation with those events from real data taken by the detector. The process of generating an event using MC simulation can be categorised into two parts: event generation and detector simulation. This chapter describes event generation, detector simulation and the subsequent reconstruction of particles most relevant to the analysis presented in this thesis.

4.1 Event Generation

The main software framework used in ATLAS, Athena [54], provides the tools to run MC simulation of proton-proton collisions as well as the ATLAS detector response to such physics processes. Figure 4.1 illustrates the various levels of processing for ATLAS simulated data. This section describes the first step in the MC production chain: the event generation of the primary event from the proton-proton interaction.

Scattering processes at high energy hadron colliders can be classified as either hard (high energy) or soft, which can be theoretically described by QCD. Figure 4.2 provides a schematic representation of a hadronic scattering process. During event generation, MC generators are used to simulate the result of such interactions which can described by four-vectors.

In the following, a brief description of the basic simulation steps performed by generators is given: the initial state of the proton, where the momentum shared amongst the

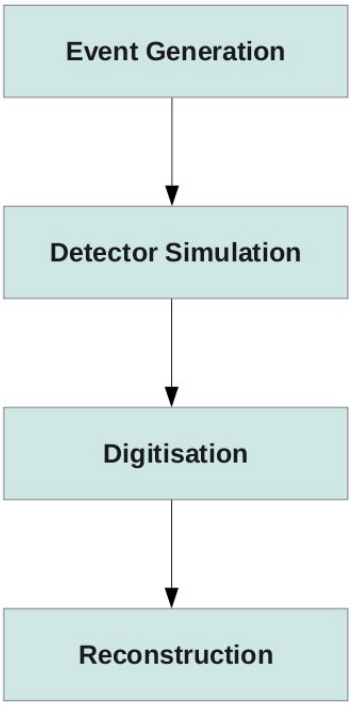

Figure 4.1: Full MC production chain.

partons is described by a so-called Parton Density Function (PDF); any activity outside the hard process, known as the "underlying event"; the final state parton showers; and the hadronisation. The MC generators used for the MC samples used in this thesis are listed in Section 5.1

Parton Density Function

PDFs [55] provide a measure of the partonic structure of hadrons, which is important for any process which involves colliding hadrons. Their main purpose is to simulate partons coming into the hard scatter process using matrix elements in lowest order perturbation theory to calculate a probabilistic distribution of the outgoing partons.

Parton Showers

Once a description of the outgoing partons is obtained, Parton Showers (PS) are used to describe the evolution of the partons involved in the hard collision, in this case coloured particles (quarks and gluons). Incoming and outgoing partons can radiate gluons, causing an extended shower and a loss in momentum of the incoming parton shower. This can be calculated using Sudakov form factors [55], which describe the probability that a parton evolves from an initial scale t_0 to a final scale t without radiating or splitting. The parton

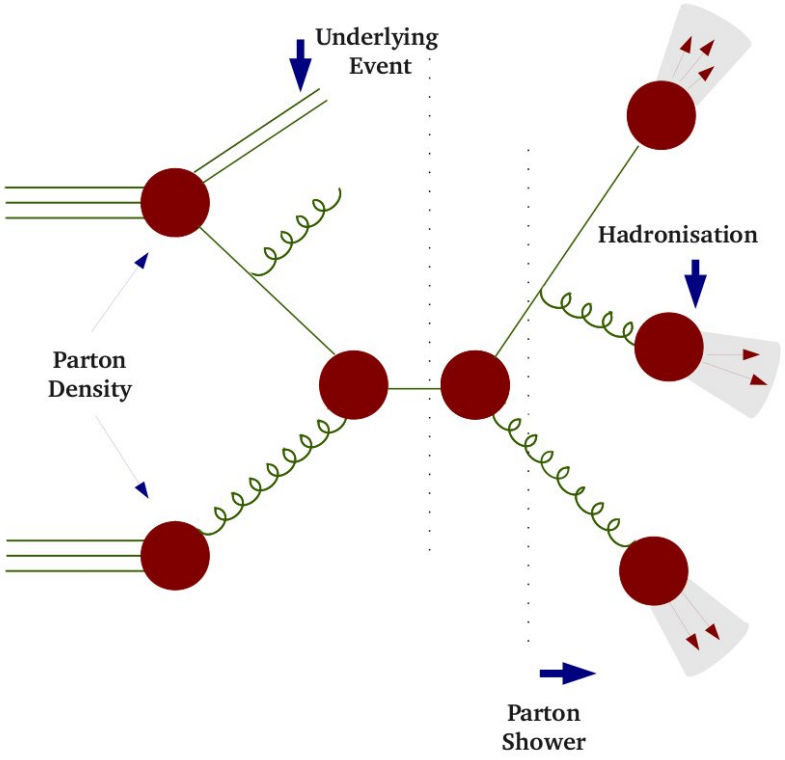

Figure 4.2: Diagram of a simulated high energy proton-proton collision process.

shower evolution starts from the hard process until a specific lower momentum scale is reached to a point where perturbation theory is no longer viable. This non-perturbative effect that causes the formation of hadrons from partons is called hadronisation.

Hadronisation and the Underlying Event

After the PS, hadronisation proceeds by using all partons which have been evolved and other soft gluons coming from partons themselves. Partons are combined with their neighbours to form colour singlets. After the hadronisation, the stable particles are passed to the detector simulation to interact with the detector material.

In hadron collisions there will be partons that do not take part in the hard interaction and which can interact among them and contribute to the final state. These form the underlying event and are also taken into account by the MC generators.

4.2 Detector Simulation

Generated events are passed through a detector simulation, which mimics the response of the real detector to the physics processes. In ATLAS, this is performed using the GEANT4 [56] simulation framework, integrated in the ATLAS offline software. The de-

tector simulation produces GEANT4 hits, which record positions in the tracking detectors and the energy deposits in the calorimeter cells. At this stage, output files containing data of the detector simulation, known as a "hit files", are generated. These are then "digitised" to produce voltages and currents in the detector. The simulation of electronic noise, pile-up (see Section 4.4), as well as other effects from the detector electronics will also be taken into account at digitisation stage. Data in "raw digits" format are known as Raw Data Object (RDO) which is the default format used by the ATLAS trigger and all reconstruction algorithms (described in Section 4.3). It is important to mention that the same detector geometry and simulation infrastructure is used for simulation, digitisation and reconstruction processes to ensure agreement between simulation and reconstruction. At the end of the detector simulation, the simulated data (in the form of digits) are in a format that is equivalent to the data recorded with the ATLAS detector. This is what is referred to as "full" MC simulation. Figure 4.3 shows a detailed MC simulation chain and the corresponding data format at every stage.

A faster simulation process can also be performed using the "ATLFAST-II" package [57], which takes the generated events and performs a parametrisation of the calorimeters response, which accounts for the missing simulation steps with respect to the full simulation, to produce a format equivalent to that obtained after the reconstruction stage. A fast simulation is important in cases when the total number of events simulated is a limiting factor for analysis. For the work reported in this thesis, this is the case for the production of $t\bar{t}$ events and some SUSY signal samples, discussed in Chapter 5.

The next section details how the simulated detector signals and the real data are processed in order to reconstruct the physics objects that are most relevant for the analysis discussed in Section 7.

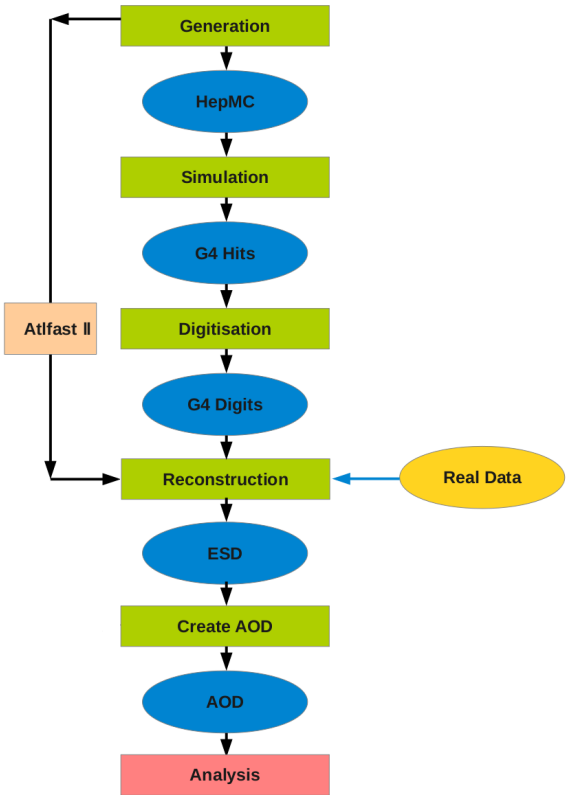

Figure 4.3: Schematic representation of the Full Chain Monte Carlo production. The orange boxes highlight the various stages in a "full" MC simulation; blue ovals correspond to the data format obtained at every stage of the MC simulation chain.

4.3 Reconstruction

The ATLAS offline reconstruction software processes the raw detector and simulated data to reconstruct the physics objects in each event. The building blocks of object reconstruction are ID and MS tracks (only in the case of muons), and energy deposits in the electromagnetic and hadronic calorimeters. The reconstruction of physics objects is done by dedicated algorithms which are specific to signals of different detector components. These algorithms are implemented within the Athena framework and their performance is detailed in ref. [45].

In the following sections, the reconstruction of physics objects relevant for the analysis presented in this thesis, such as, leptons and jets (narrow cone of hadrons), are discussed. A more refined identification procedure is performed on the reconstructed physics objects, combining calorimeter and track quantities to discriminate mis-reconstructed or background objects from the signal objects; details are discussed in Chapter 6.

4.3.1 Tracks

A collection of hits in the tracking sub-systems of the inner detector linked to a charged particle traversing the ID forms "tracks", which provide the information necessary to reconstruct the path of a charged particle. Generally, a track can be parametrised using variables which are defined relative to the position of the primary interaction point. In particular, the Primary Vertex (PV) of the event defines the reference point with respect to which impact parameters (d_0 and z_0) and vertex displacements are measured, it is defined as the interaction point (vertex) with associated tracks that have the highest sum of p_{T}^2. Impact parameters are track distance variables defined relative to an origin, hence, their sign provides a discriminator for tracks originating from b-hadron decays to those originating from the primary vertex. Track candidates are reconstructed in the ID using standard ATLAS track reconstruction algorithms [58]. In the analysis presented in this document, track selection refers to those originating from prompt particles (or from primary vertices), which satisfy the following quality criteria: $|\eta| < 2.5$, $|d_0| < 1.5$ mm and $|z_0| < 1.0$ mm, where the origin is taken to be the position of the primary vertex.

4.3.2 Electrons

As electrons traverse the detector, they will leave a track in the inner detector layer, continuing to deposit most of their energy in the electromagnetic calorimeters (ECAL) where they stop. A "calorimeter cluster" of an electron is defined as the energy deposit in a given $\eta - \phi$ region of the electromagnetic calorimeter. Electron candidates in a pseudo-rapidity range of $|\eta| < 2.47$ are reconstructed by matching ECAL clusters to charged particle tracks in the ID. To reconstruct calorimeter clusters, a "sliding-window" algorithm is used [59]. It starts from "seed" clusters with a fixed rectangular shape, usually a size corresponding to the granularity of the middle layer of the EM calorimeter (3×5 cells of size 0.025×0.025 in $\eta \times \phi$), and transverse energy of at least 2.5 GeV. Seed clusters are then matched to tracks reconstructed in the ID (as in Section 4.3.1), with tracks being extrapolated from their last hit in the ID to the middle layer of the ECAL. To form an electron candidate, at least one track must be within $\Delta|\eta| < 0.05$ of the reconstructed seed cluster. If more than one track is available, tracks with silicon hits are preferred, and the track with the smallest $\Delta R = \sqrt{\Delta\eta^2 + \Delta\phi^2}$ value is chosen.

Once seed clusters and ID tracks are matched, seed clusters are rebuilt using a cluster size of 3×7 (5×5) cells in the barrel (endcap), centred around the track-matched cluster centre to determine the energy of the electron candidate (detailed in ref [60]). The total

energy of the electron candidate is determined by two components: the measured cluster energy plus an estimate of any energy deposited outside the ECAL cluster (referred to as leakage, detailed in ref [60]).

At this stage, electron candidates are referred to as reconstructed electrons. The efficiency for central electrons to pass the cluster reconstruction and track matching requirements, shown in Figure 4.4, is above 96% in 2012.

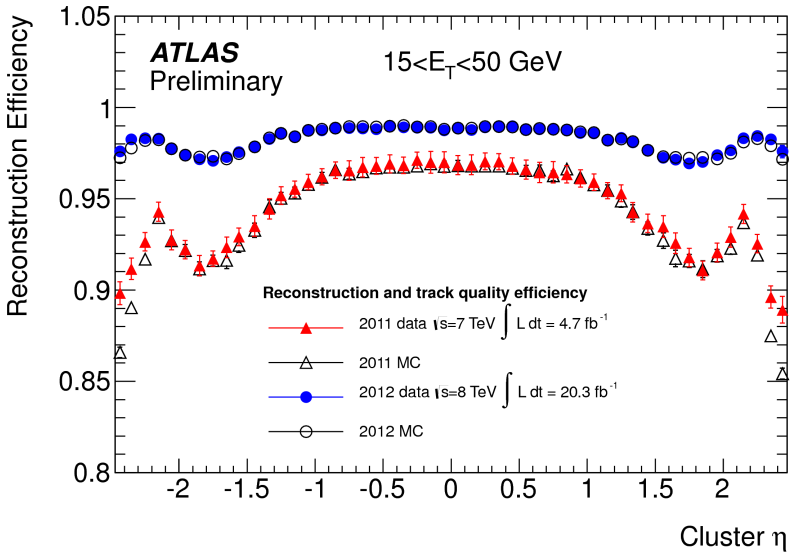

Figure 4.4: The 2011 (red) and 2012 (blue) electron reconstruction efficiency, including track quality criteria, is shown as a function of the pseudo-rapidity η for electrons with transverse energy $\vec{E}_{\mathrm{T}}^{\mathrm{miss}}$ between 15 and 50 GeV for data and MC. The reconstruction and track-quality efficiency shown in the figure is measured with Z$\rightarrow$ *ee* events in data and MC using the "tag-and-probe" method [61].

The direction of the reconstructed electron will be mainly determined by that of the track, however, if the track quality criteria discussed in Section 4.3.1 is not passed, the direction of the cluster will determine the one of the electron candidate.

4.3.3 Muons

Muons can go through all detector layers: ID, electromagnetic and hadronic calorimeters and MS. In general, muon candidates are reconstructed using the STAtistical COmbination (STACO) algorithm [62] combining inner detector and muon spectrometer track information, with three different procedures:

- "standalone" reconstruction, where the muon trajectory is reconstructed using only MS track segments, which are built from hits in each section of the MS are combined

to build track segments up to $|\eta| < 2.7$ and then get extrapolated to the beam line;

- "combined" muon reconstruction, where a standalone muon track and the ID track are reconstructed independently and afterwards matched (provided that the measured p_{T} for both tracks are compatible);

- "segment tagged"muon reconstruction, which identifies muon candidates with a track in the ID only if the trajectory extrapolated to the muon spectrometer can be associated with straight track segments in the MS.

Reconstruction algorithms that rely on both the MS and ID provide a better momentum measurement. Therefore, only combined and segment tagged muons are considered in this analysis.

The next and final stage of muon reconstruction determines the energy loss of muons in the calorimeters which causes the measured momentum in the MS to differ from the initial momentum of the muon. The energy of the reconstructed muon candidate will need corrections to take this into account, which is known as smearing. The p_{T} of the measured tracks in the MS is corrected in MC to match the resolution observed in data [63]. The muon reconstruction efficiency is found to be greater than 98% [64] using a tag-and-probe tool with Z$\rightarrow \mu\mu$ events. The muon candidates at this stage are referred to as "reconstructed muons".

4.3.4 Jets

As hadronic jets travel across the detector they can leave tracks in the ID layer and deposit energy in both electromagnetic and hadronic calorimeters. Therefore, clusters of calorimeter cells are the building blocks of jets. Jet reconstruction starts with the formation of topological clusters [59], which are a type of clustering algorithm with a variable number of cells (unlike the sliding-window algorithm described in 4.3.2). Topological clusters are seeded by calorimeter cells with large signal (S) to noise (N) ratio ($S/N \geq 4$), which grow by iteratively adding neighbouring cells with $S/N \geq 2$. The resulting topological clusters are taken as input by the anti-k_t jet algorithm [65] with a distance parameter $\Delta R = 0.4$ to form a jet candidate.

Calibration of the topological clusters is performed by weighting differently the energy deposits arising from electromagnetic showers (also known as "EM scale") to those from hadronic showers [66]. The jet reconstruction in the analysis presented in this thesis is performed using the "antiK_T4LCTopoJets" algorithm, which takes calibrated topological

clusters as jet constituents.

b-tagged jets

B quarks hadronise into *b*-hadrons which will then decay in cascades to lighter hadrons or leptons. These are commonly referred to as *b*-jets. *b*-jet algorithms are designed to identify heavy flavour content in reconstructed jets by taking advantage of specific properties of the *b*-hadrons such as high mass (of about 5 GeV) and long lifetime of the *b* quark (∼1.5 ps) with respect to the lighter quarks. The presence of a displaced secondary vertex is a characteristic of a *b*-jet, this is due to the long lifetime of the *b* quark which translates into a large decay length, L_{xy}. The secondary vertex will generate displaced vertex tracks, which are characterised by larger impact parameters than the ones defining the primary vertex (see Figure 4.5). Displaced vertices and charged tracks are key objects taken as

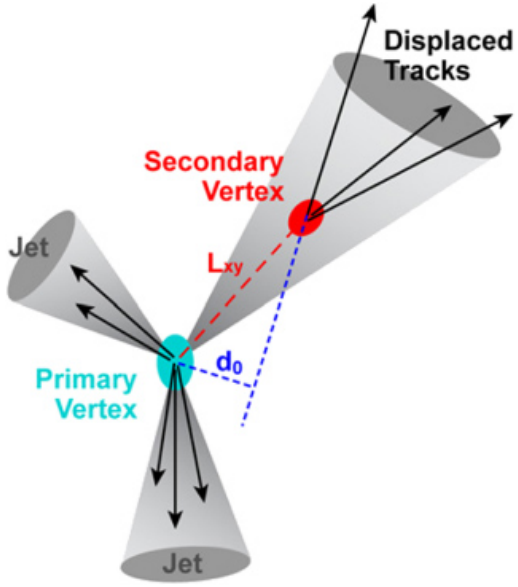

Figure 4.5: Representation of a *b*-jet accompanied by two light jets, where the distance of the secondary vertex (L_{xy}) and the impact parameter (d_0) of each track is illustrated in the figure [67].

input for the *b*-tagging algorithms. There is a wide variety of *b*-tagging algorithms, such as IP3D (impact parameter based), SV1 (secondary vertex based) and JetFitter (decay chain reconstruction based), which are discussed in [68]. The analysis discussed in this thesis makes use of the MV1 [69] algorithm, which is a multivariate technique[1], based on inputs from these three algorithms, and by combining them it achieves higher rejection of

[1]Multivariate techniques use physically motivated variables to generate a discriminant, a single number which summarises the final discriminatory performance of the variables when various cuts are applied.

light quark jets. In Section 6.2.3, the specifications on the operating point for the MV1 algorithm are detailed.

4.4 Pile-up Simulation

With high instantaneous luminosity (defined in Equation 3.1) the number of non-hard-scattering interactions for every beam crossing in an event will increase. This is known as pile-up. In general, the mean number of interactions per bunch crossing μ corresponds to the mean of the Poisson distribution on the number of interactions per crossing that can be derived from the instantaneous luminosity definition 3.1.

In order to match the pile-up conditions observed in data, simulated samples of both background and signal processes are overlayed with a Poissonian-distributed number of pile-up events and the resulting events are re-weighted such that the distribution of the number of interactions per bunch crossing agrees with the data. Figure 4.6 shows the luminosity-weighted mean number of interactions per bunch crossing μ for the 7 TeV and 8 TeV centre-of-mass luminosities.

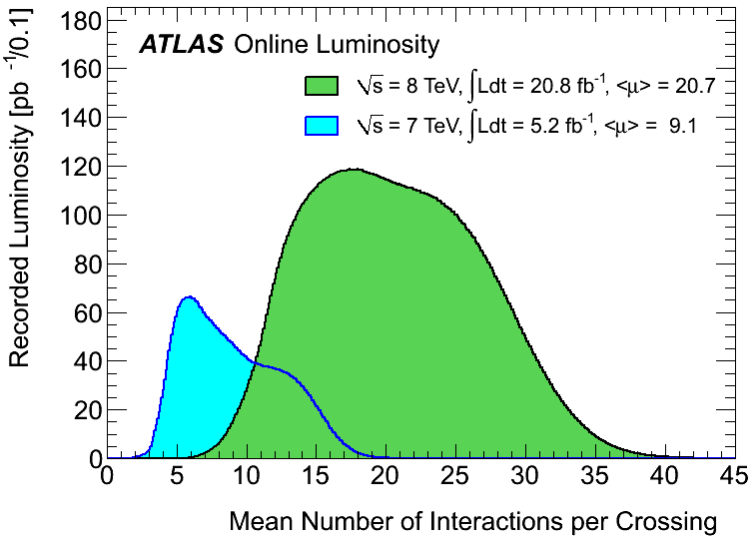

Figure 4.6: Luminosity-weighted distribution of the mean number of interactions per crossing for the 2011 and 2012 data. The mean number of interactions per bunch crossing (μ) corresponds the mean of the Poisson distribution on the number of interactions per crossing calculated for each bunch [70].

Chapter 5

MC samples

ATLAS simulated data are generated by a set of well known MC generators. This chapter provides a description of the relevant generators used to simulate the SM processes and new physics signals relevant for the SUSY searches described in this document.

5.1 MC Generators

The main features of the different types of MC generators employed in this thesis are described below.

General Purpose MC Generators

Pythia [71], Herwig [72] and Herwig++ [73] are general purpose MC event generators that use Matrix Element (ME) calculations at Leading Order (LO), which include the simulation of both hard and soft interactions. For the simulation of the underlying event, Herwig is interfaced with Jimmy [74]. Both Pythia and Jimmy simulate the Underlying Event (UE) as a scattering between proton remnants using matrix elements at LO.

Sherpa [75] is another multi-purpose event generator, interfaced with Pythia for the simulation of the parton shower, that uses a multiple parton scattering model for underlying event simulation.

Matrix Element MC Generators

The Alpgen [76], MadGraph [77] and AcerMC [78] generators simulate the hard process of a proton-proton collision using calculations at fixed order in perturbation theory.

Events are generated with different multiplicities of outgoing partons, and cross sections are calculated at LO. For the parton shower and hadronisation, these generators are

interfaced with PYTHIA or HERWIG because they can only provides generation of events at parton-level. The addition of parton shower introduces a double-counting of events. This is because the effect of parton shower on a sample with n-partons can produce additional jets that are already taken into account in the n+1-partons sample. When more than two generators are interfaced, matching techniques, such as CKKW [79] and MLM [80], are used to remove double counting the matrix element and parton shower emissions.

Next-to-Leading Order MC Generators

MC@NLO [81] and POWHEG [82] provide alternative simulation methods which combine lowest-multiplicity Next-to-Leading Order (NLO) matrix elements with parton showers without double counting. MC@NLO and POWHEG produce hard scattering processes at NLO, the difference lying on the fact that former includes negative weighted events in the method used to prevent double counting. The MC@NLO generated events are typically used as input to HERWIG for the parton shower and hadronisation, and to JIMMY for the underlying event. POWHEG generated events are interfaced with PYTHIA to include parton shower and underlying event effects.

5.2 Background MC Samples

Several background samples have been considered in this analysis and can be grouped in different categories, as detailed in the following.

Dibosons: WW, WZ and ZZ processes are generated with the NLO generator POWHEG. These samples correspond to all SM diboson diagrams leading to $\ell\nu\ell'\nu'$, $\ell\ell\ell'\nu'$ and $\ell\ell\ell'\ell'$, respectively, with $\ell, \ell' = e/\mu/\tau$ and $\nu, \nu' = \nu_e/\nu_\mu/\nu_\tau$. The SHERPA generator is used for the $Z/W + \gamma$ processes.

Tribosons: $pp \to WWW \to l\nu l\nu l\nu$, $pp \to ZWW \to lll\nu l\nu$ and $pp \to ZZZ \to llll\nu\nu$ processes (collectively referred to as VVV) were generated with MADGRAPH to LO in QCD.

$t\bar{t}$+boson: $t\bar{t}$+Z(+jets) and $t\bar{t}$+W(+jets) samples were generated using the LO generator ALPGEN, while the $t\bar{t}$+WW and tZ samples were generated using MADGRAPH. All $t\bar{t}$+boson samples are collectively referred to as $t\bar{t}V$ and have at least one of the top quarks is decaying semi-leptonically ($t \to Wb \to b\ell\nu$).

Top: pair-production, $t\bar{t}$, was generated with POWHEG (+PYTHIA for simulating the parton shower, hadronisation and the underlying event); single top production in the t-channel ($bq \to tq'$ and $b\bar{q}' \to t\bar{q}$) was generated with MC@NLO (+HERWIG for the simulation of parton shower and hadronisation); and single top production processes in the s-channel ($q\bar{q} \to W^* \to t\bar{b}$) and the associated production of a top quark and a W boson, Wt, was generated with ACERMC (+PYTHIA). All samples are produced using a top quark mass of 172.5 GeV and have been re-normalised to Next-to-Next-to Leading Order (NNLO).

Boson+jets: samples of Z/γ^* production and W production in association with jets (light and heavy flavour jets are taken into account) are produced with ALPGEN (+PYTHIA). For simplicity, these samples are referred to as "V+jets". The W and Z/γ^* ALPGEN LO cross sections are re-normalised to NNLO.

Standard Model Higgs: production samples, where the Higgs decays are via taus or via W/Z bosons, are generated with PYTHIA. $H \to \tau\tau$, $H \to WW^*$ and $H \to ZZ^*$ decaying into leptonic final states are considered, as these are expected to be the most important sources of Higgs background in this analysis. Five production mechanisms are included: gluon Fusion (ggF), Vector Boson Fusion (VBF), associated production with a W (WH) or Z boson (ZH), and associated production with a $t\bar{t}$ pair ($t\bar{t}H$). All cross sections are calculated at NNLO, except $pp \to t\bar{t}H$, which is calculated at NLO QCD precision.

For all simulated processes, the propagation of particles through the ATLAS detector is modelled with GEANT4 using the full ATLAS detector simulation, except the $t\bar{t}$ POWHEG sample, for which ATLFAST-II simulation is used.

Simulated events are weighted to match the distribution of the number of interactions per bunch crossing observed in data, as discussed in Section 7.6.

Free parameters for the different PS, UE and hadronisation models are tuned to data. The three different parameter tunes used for the underlying event generation in all MC samples are the ATLAS Underlying Event Tune 2B (AUET2B), AU2 and PERUGIA2011C, which are discussed in detail in [83].

Dedicated calculations are used to provide a re-normalisation of the total cross sections for each SM processes at NLO or NNLO, these have been specified in Table 5.1. The choice of parton density function depends on the generator and for this analysis the CTEQ6L1 [84] PDFs are used with MADGRAPH, ALPGEN, ACERMC, and PYTHIA and the CT10 [85]

PDFs with MC@NLO, POWHEG and SHERPA.

The choice of the generator type and the order of cross section calculations used for yield normalisation for the SM processes are summarised in Table 5.1

Table 5.1: MC samples used in this analysis for background estimates, the generator type and the order of cross section calculations used for yield normalisation are also reported.

Process	Generator	Cross section
Dibosons		
WW, WZ, ZZ	POWHEG + PYTHIA 8	NLO QCD with MCFM [86, 87]
Tribosons		
WWW, ZZZ, WWZ	MADGRAPH +PYTHIA	NLO[88]
Top+Boson		
$t\bar{t}$ W/Z	ALPGEN +HERWIG	NLO [89, 90]
$t\bar{t}$ WW	MADGRAPH +PYTHIA	NLO [90]
t Z	MADGRAPH +PYTHIA	NLO [91]
Top-quark pair-production		
$t\bar{t}$	POWHEG +PYTHIA	NNLO+NNLL [92]
Single top		
t-channel	ACERMC +PYTHIA	NNLO+NNLL [93]
s-channel, Wt	MC@NLO +HERWIG	NNLO+NNLL [94, 95]
W/Z+jets	ALPGEN +PYTHIA	DYNNLO [96]
Higgs		
via gluon fusion	POWHEG +PYTHIA 8	NNLL QCD, NLO EW [97]
via vector-boson fusion	POWHEG +PYTHIA 8	NNLL QCD, NLO EW [97]
associated W/Z production	PYTHIA 8	NNLL QCD, NLO EW [97]
associated $t\bar{t}$ production	PYTHIA 8	NNLO QCD [97]

5.3 Signal MC Samples

Signal samples referring to the models considered in this analysis (Section 2.2.3) are generated with Herwig++, using the CTEQ6L1 PDFs. Signal cross sections are calculated to NLO+NLL using PROSPINO2 [98]. Lepton or hadronic tau filters are applied during event generation to enhance decays into a particular final state. In particular, a generator-level filter was applied to the simplified model with staus requiring at least one hadronic tau ("tau filter") with visible $p_{\mathrm{T}} > 15$ GeV and $|\eta| < 2.7$. Moreover, a "light lepton filter"

(electron/muon) with the additional requirement of an electron/muon with $p_{\mathrm{T}} > 5$ GeV, $|\eta| < 2.7$ is applied to explore final states with and without hadronic taus.

The list the signal samples used in this thesis can be found in Table 5.2.

Table 5.2: MC signal samples used in this analysis.

Signal Grid	Remarks	Dataset ID
simplified model	via sleptons	144871-144896, 157461-157968, 176531-176557
	via WZ	164274-164323, 174663-174678, 174835-174840
	via staus	176776-176852 (tau filter), 179223-179299 (light lepton filter)
	via Higgs	176641- 176707
pMSSM	$\tilde{\ell}_{\mathrm{R}}$, $\tan\beta = 6$, $M_1 = 100\,\mathrm{GeV}$	164949-165230
	$\tilde{\ell}_{\mathrm{R}}$, $\tan\beta = 6$, $M_1 = 140\,\mathrm{GeV}$	165239-165519
	$\tilde{\ell}_{\mathrm{R}}$, $\tan\beta = 6$, $M_1 = 250\,\mathrm{GeV}$	165525-165740
	$\tilde{\tau}_{\mathrm{R}}$, $\tan\beta = 50$, $M_1 = 75\,\mathrm{GeV}$	183236-183335
	no $\tilde{\ell}$, $\tan\beta = 10$, $M_1 = 50\,\mathrm{GeV}$	186100-186199

Chapter 6

Object Selection

The process of identifying the reconstructed particles in the analysis presented in this thesis is detailed in this chapter. The particle identification criteria will be classified as "baseline" and "signal", where the former provides a basic description of a particle and the latter satisfies a tighter selection criteria, which is analysis dependent.

6.1 Overlap Removal

It often occurs that the same objects are reconstructed by more than one of the particle identification algorithms described in Section 4.3. To avoid double counting objects, a preference to one of the objects needs to be defined. The preference of one object over another can be based on the level of efficiencies or on the "purity" of the object, which is enhanced by suppressing background events or wrongly reconstructed objects as the corresponding object. The so-called "overlap removal" is performed between loosely identified objects (defined as "baseline" objects in Section 6.2) and is applied in the order presented in Table 6.1. The following describes the procedure of the overlap removal scheme.

Whenever two electron candidates are found geometrically close to each other in a cone of $\Delta R < 0.05$, this can be an indicator that two calorimeter clusters were matched to the same ID track, in this case, the lowest p_{T} electron candidate is removed from the event. In case where two muon candidates overlap due to shared tracks ($\Delta R_{\mu,\mu}$ <0.05), then both muon candidates are removed from the event. Electron candidates may also be found by jet algorithms (used for jet and hadronic tau reconstruction), but due to the higher efficiency and purity of the electron reconstruction algorithms, the jet and hadronic tau candidates are rejected if the overlap with an electron within $\Delta R < 0.2$. Similarly, if a tau candidate is close-by ($\Delta R < 0.2$) to a muon candidate, the tau is

Table 6.1: Overlap removal criteria for objects used in the analysis presented in this thesis. The indices refer to the object pair being evaluated, where the first object will take precedence over the second object.

Overlap Removal Cuts	**Definition**
$\Delta R_{electron1,electron2}$ <0.05	Discard lowest p_{T} electron to remove duplicated electrons with different calorimeter clusters and shared tracks.
$\Delta R_{electron,jet}$ <0.2	Discard jet to remove electron duplication coming from the jets.
$\Delta R_{electron,\tau}$ <0.2	Discard tau to remove electron duplication coming from the taus.
$\Delta R_{\mu,\tau}$ <0.2	Discard tau to remove muon duplication coming from the tau.
$\Delta R_{jet,electron}$ <0.4	Discard electron to remove electrons within jets.
$\Delta R_{jet,\mu}$ <0.4	Discard muon to remove muons within jets.
$\Delta R_{electron,\mu}$ <0.01	Discard both electron and muon candidates due to muons undergoing Bremsstrahlung.
$\Delta R_{\mu,\mu}$ <0.05	Discard both muons due to shared tracks.
Δm_{SFOS} <12 GeV	Discard leptons pairs with same flavour and opposite charge to suppress background from low mass resonances.
$\Delta R_{signal\ \tau,jet}$ <0.2	Discard jets to remove "signal taus" (defined in Section 6.2.4) duplicated among the jets.

rejected. Jets may contain leptons from semi-leptonic b- and c-quark decays, and they can reconstructed as light leptons (e/μ). To remove such leptons from jet candidates, and additional ΔR requirement is imposed on electrons and muons. Another possible scenario is if a high-p_{T} muon candidate undergoes Bremsstrahlung (radiates a photon), the resulting photon may be wrongly reconstructed as an electron (jet overlap removal has already been applied at this point). Both mis-reconstructed objects are removed if close-by to each other ($\Delta R_{electron,\mu}$ <0.01). Hadronic taus are reconstructed using jets as building blocks, hence, any overlapping jet with a "signal" tau candidate (defined in Section 6.2.4) is discarded.

6.2 Object Identification

A detailed description of the physics objects used in this analysis is of primary importance to understand the results in this thesis. The rest of this chapter focuses on the description of the object identification criteria that follows from reconstruction, used for electrons, muons, taus, jets and missing transverse energy.

6.2.1 Electrons

Electron identification criteria rely on a cut-based[1] selection using tracking and calorimeter information which are applied to the reconstructed electron described in Section 4.3.2. This is performed to reduce the number of non-prompt ("fake") electrons. Three reference sets of requirements are used [60]: "loose", "medium" or "tight", in order of decreasing efficiency and increasing background rejection power. Some of these requirements include: shower shape variables of the EM calorimeter middle layer are used in the loose selection; track quality requirements and track-cluster matching added on top of the loose requirements for the medium selection; and the tight selection adds requirements on the track matching (i.e. ratio of the cluster energy, E, to the track momentum, p), uses information from the TRT (i.e. number of hits in the TRT), and discriminates against photon conversions using hit information in the ID.

The electron candidates passing the cuts listed in Table 6.2 and the overlap removal requirements in Table 6.1 are considered as baseline electrons.

Table 6.2: Baseline selection criteria for electrons.

Baseline Cuts	**Definition**
Medium++	Medium ID selection in the egamma algorithm.
$\lvert\eta^{cl}\rvert$ <2.47	Cluster pseudorapidity requirement.
E_{T} >10 GeV	The electron energy in Monte Carlo is smeared to reproduce the resolution observed in data.
author == 1 or *author* == 3	*author* selects only electrons reconstructed by the egamma-algorithm optimised for high p_{T} electrons.

Signal electrons are selected starting from baseline electrons with additional (tighter) quality requirements listed in Table 6.3. These include impact parameter requirements to remove tracks associated to pile up interactions and isolation requirements to discriminate against heavy flavour decays. This selection is designed to reject "fake" electrons coming from non-isolated electrons, photon conversion produced electrons, and jets faking electrons.

A tag-and-probe method is performed using $Z \to ee$ and $J/\Psi \to ee$ events to measure the efficiency of electron identification [60]. Figure 6.1 shows the efficiencies obtained using Z$\to$ ee events for the various levels of identification cuts as a function of transverse energy.

[1] Cut-based techniques use a set of criteria motivated by physical considerations and cut values are determined by analysing samples of signal and background objects. The cuts can be applied independently.

Table 6.3: Signal selection criteria for electrons.

Signal Cuts	**Definition**
$Tight{+}{+}$	Tight ID selection within the egamma algorithm.
	Impact Parameter Requirements
Unbiased $\lvert d_0\rvert/\sigma(d_0)$ <5	Distance of closest track to the reconstructed primary vertex in the transverse plane.
Unbiased $\lvert z_0 sin(\theta)\rvert$ <0.4 mm	z_0 is the longitudinal distance of closest track to PV.
	Isolation Requirements
$p_{\mathrm{T}}cone30/E_{\mathrm{T}} < 0.16$	Transverse momentum of all tracks $p_{\mathrm{T}} > 1$ GeV within $\Delta R \leq 0.3$ around the electron track and E_{T} is the electron transverse energy.
$e_{\mathrm{T}}cone30^{corrected}/E_{\mathrm{T}} < 0.18$	$e_{\mathrm{T}}cone30^{corrected} = e_{\mathrm{T}}cone30 - A \times N_{vtx}$ with $A = 20.15$ MeV (17.94 MeV) in data (MC), N_{vtx} is the number of vertices with at least 5 tracks, and $e_{\mathrm{T}}cone30$ is the p_{T} and energy-density corrected isolation.

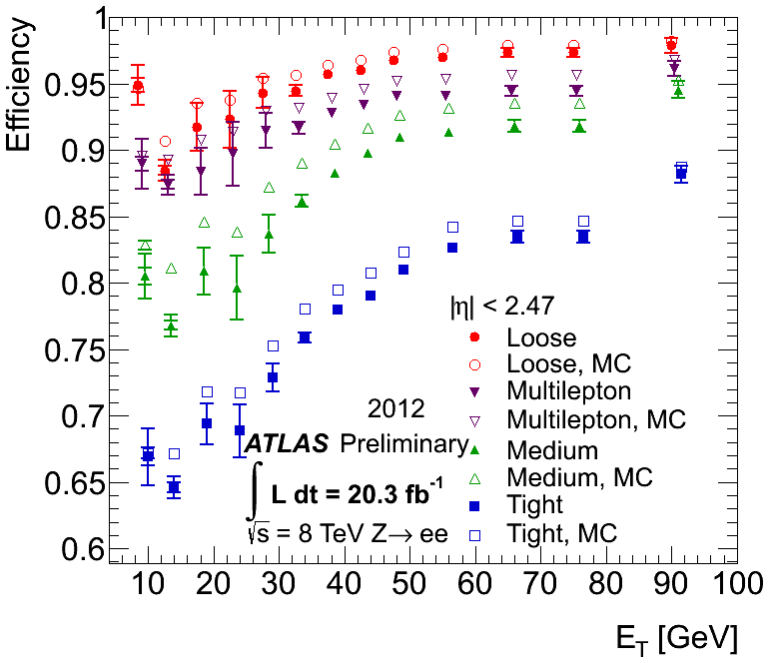

Figure 6.1: 2012 Electron identification efficiency as a function of E_T. Four sets of cut-based identification criteria are employed for the 2012 analyses. Data and MC efficiencies are reported [61].

6.2.2 Muons

Muon identification is performed on all the tracks where the MS tracks are associated to ID tracks. This is done by requiring high quality track selection (as defined in Section 4.3.1) and track-based isolation criteria. A summary of the requirements for a baseline muon is in Table 6.4, where candidates have also passed the overlap removal described in Table 6.1.

Additional isolation requirements to define a signal muon are described in Table 6.5. These signal requirements use isolation parameters to help discriminate signal muons from background ones, this is to avoid jets coming from heavy flavour decays that can be mis-identified for prompt muons. Also, impact parameters with constraints placed on the muon origin (with respect to the primary vertex of the event) are used to reject muons from cosmic rays.

Corrections to the reconstructed muon momentum have been derived by comparing the reconstructed muon momentum in experimental and simulated data [99]. For these corrections, $Z \to \mu\mu$ and J/Ψ events have been used by comparing the invariant mass line-shape of the resonances and, in case of Z events reconstructed with muons in the MS, also the difference between transverse momentum reconstructed in the ID and in the MS.

Table 6.4: Baseline selection criteria for muons.

Baseline Cuts	**Definition**
loose id	Minimal ID tracking information for the combined and segment tagged muons within the STACO algorithm [45].
$\|\eta\|$ <2.5	Pseudorapidity requirement.
p_{T} >10 GeV	The muon p_{T} is shifted and smeared in MC to better reproduce the resolution in data (as recommended by the Muon Combined Performance Group).
b-layer hit ≥ 1, pixel hit ≥ 1 and SCT hits≥ 6, less than 3 holes in the pixel and SCT, $n > 5$ and $\mathrm{n}_{TRT}^{outliers} < 0.9 \times n$	ID track requirements. ($n = n_{TRT}^{hits} + n_{TRT}^{outliers}$)

Table 6.5: Signal selection criteria for muons.

Signal Cuts	**Definition**
unbiased $\|d_0\|/\sigma(d_0)$ <3 Unbiased $\|z_0 sin(\theta)\|$ significance $\leq$1 mm	Impact Parameter requirements.
$p_{\mathrm{T}}cone30^{\mathrm{corrected}}/p_{\mathrm{T}} < 0.12$	Isolation Requirements $p_{\mathrm{T}}cone30^{\mathrm{corrected}} = p_{\mathrm{T}}cone30 - A \times N_{vtx}$ with $A = 10.98$ MeV (6.27 MeV) in data (MC).

6.2.3 Jets

The baseline jet identification criteria is based on kinematic requirements which aim to efficiently reject background jets while keeping the highest efficiency selection for jets produced in proton-proton collisions. All selected jets must: have high transverse momentum, $p_{\mathrm{T}} > 20$ GeV; be within the pseudorapidity coverage of the calorimeters, $|\eta| < 4.5$; and pass the overlap removal scheme explained in Section 6.1.

Signal jets are selected from baseline jets, which are required to cover a pseudorapidity range of $|\eta| < 2.5$ and that the fraction of jet transverse energy associated to tracks coming from the primary vertex, the so-called Jet Vertex Fraction (JVF) is greater than 0.5. Large JVF values suppresses jets from a different (not primary) interaction in the same beam bunch crossing.

B-tagged jets

Classification of signal jets as *b*-jet candidates is done using a multivariate tagging algorithm, the MV1 algorithm [69]. This algorithm has various levels of identification based

on the tagging efficiency. Signal jets are identified as b-jets if the output of the MV1 algorithm is greater than 0.3511. This corresponds to an average b-tagging efficiency of 80% [69], with a light-flavour jet mis-identification probability of about 4%.

6.2.4 Taus

Tau leptons are much heavier than any other lepton and have a very short lifetime ($\tau_\tau = 1.9 \times 10^{-13}$ s equivalent to a path length of 87 μm). This means that they will decay in the beam pipe. Taus can decay either leptonically ($\tau \to \ell\nu_\ell\nu_\tau$, $\ell = e/\mu$) with a 35% probability, or hadronically ($\tau \to \pi\nu_\tau$) 64.7% of the times. The hadronic decay modes are classified as either "1-prong" or "3-prong" decays, where the number of prongs or tracks is determined by the number of charged decay products (pions) in the tau decays.

Figure 6.2 shows the description of the reconstruction cone of a three-prong hadronic tau.

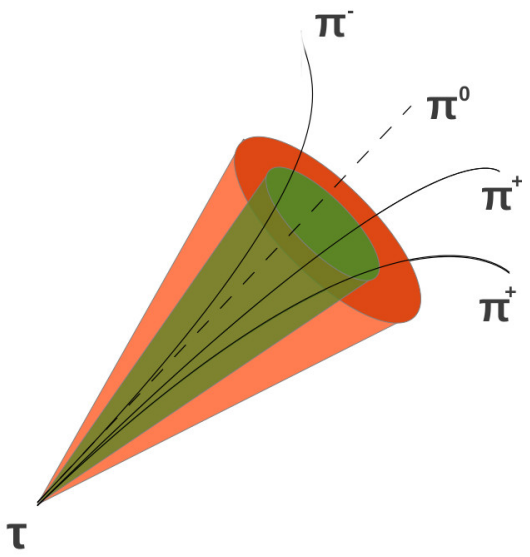

Figure 6.2: Three-prong (3 charged pions and one neutral pion) tau reconstruction cone. In the illustration, the green cone represents the tau "core" cone.

The signature of a jet is very similar to that of a hadronic tau, therefore, hadronic tau reconstruction is seeded by jets (as discussed in Section 4.3.4) reconstructed with the anti-k_t algorithm , with a distance parameter R=0.4, $p_{\mathrm{T}} > 10$ GeV and $|\eta| < 2.5$ (which corresponds to the $\eta-$coverage in the tracking system). Electromagnetic and hadronic cluster shapes in the calorimeters as well as tracks in a cone within $\Delta R < 0.2$ of the seed jet are key properties of the tau identification algorithm, which help differentiate tau from jet candidates.

The identification of hadronic taus requires further discriminating variables to reject fake taus from jets. This can be achieved using both a set of requirements and a Boosted Decision Tree (BDT)[2] multi-variate technique [100].

The following paragraphs show some of the discriminators used for tau identification, a full list of variables can be found in [101]. The working points for the different selection of variables used in the analysis are summarised in Table 6.7.

Jet BDT Discriminators

The discrimination of hadronic taus against jets is based on a BDT, which relies on seven or more discriminating track and cluster variables depending on the number of tau prongs, see [100]. The distribution of some of the discriminating variables are computed for τ-rich events and quark- or gluon-jets are shown in 6.3. These variables are the fraction of the total tau energy contained in the core cone defined by $\Delta R < 0.1$, f_{core}^{corr}, the track distance from the tau axis, R_{track}, in case of 1-prong taus and the maximum distance between two reconstructed tracks within a cone around the tau candidate, $\Delta R_{\max}$, in case of 3-prong taus. Also, the significance of a reconstructed secondary vertex, $S_{\mathrm{T}}^{\mathrm{flight}}$.

The signal and background efficiencies for tau identification are defined as

$$\varepsilon_{Signal}^{n-prong} = \frac{\#\text{ of identified } \tau \text{ candidates with } n \textit{ reco} \text{ tracks}}{\#\text{ of true decays with } n \text{ prongs}} \tag{6.1}$$

$$\varepsilon_{Background}^{n-prong} = \frac{\#\text{ of identified } \tau \text{ candidates with } n \textit{ reco} \text{ tracks}}{\#\text{ of reconstructed taus with } n \text{ tracks}} \tag{6.2}$$

Jet BDT working points are defined to target signal efficiencies of 70(65)%, 60(55)% and 40(35)% for 1(3)-prong, respectively. Background rejection factors of 10-40 for signal efficiencies of 70% are achieved, going up to 500 for 35% signal efficiencies for 1- and 3-prong taus [101].

The 2012 signal and background jet BDT identification efficiencies for 1- and 3-prong tau candidates in all BDT working points as a function of the number of vertices is shown in Figure 6.4.

Electron BDT Discriminators

The characteristic signature of 1-prong hadronic taus can also be mimicked by prompt electrons. There are several properties that can be used to discriminate between electrons

[2] Decision trees apply cuts on multiple variables in a recursive manner to classify objects as signal or background. It produces a continuous score between 0 (background-like) and 1 (signal-like), on which a user may cut to yield the desired signal or background efficiency.

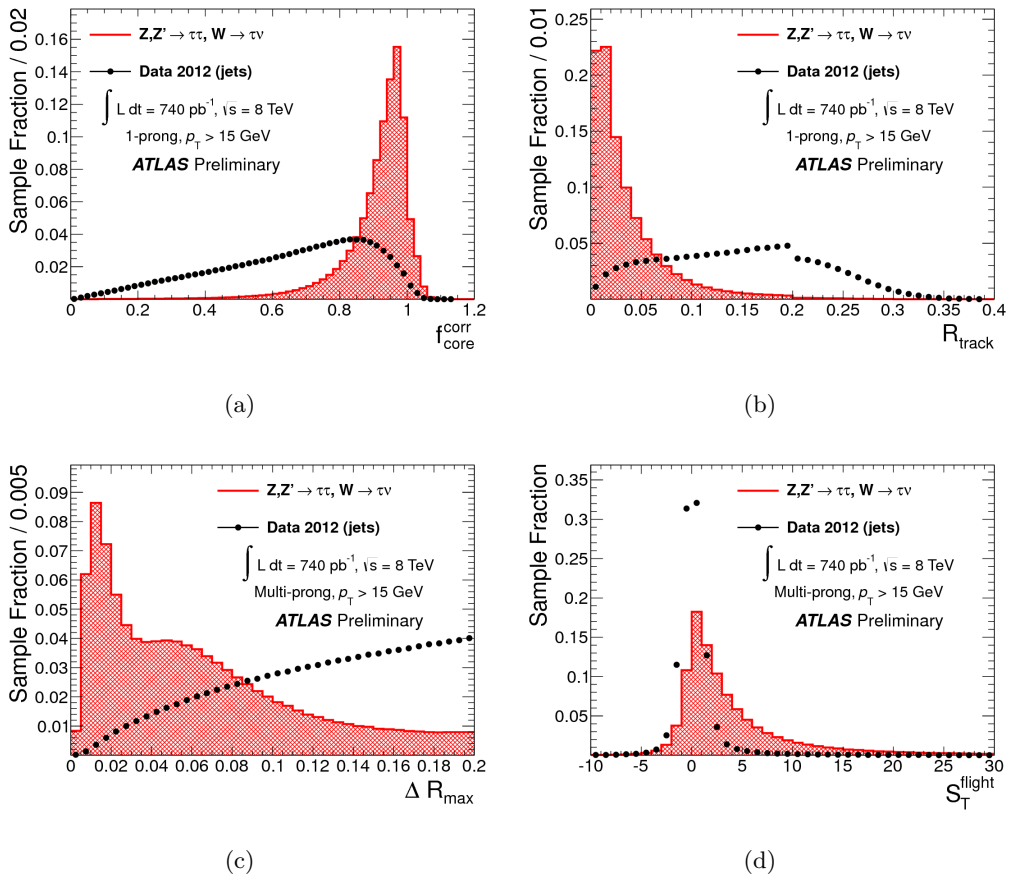

Figure 6.3: Distributions of a selection of jet discriminating variables for simulated $Z \to \tau\tau$ and $W \to \tau\nu$ MC signal samples and a jet background sample selected from 2012 data. The sudden discontinuity in (b) at 0.2 is due to a pile-up correction applied below this threshold to reduce pile-up dependence of the calorimeter variables. The distributions are normalised to unity [101].

and 1-prong taus, such as, the emission of transition radiation of the electron track and the longer and wider shower produced by the hadronic tau decay products in the calorimeter, compared to the one created by an electron. These properties are used to define tau identification discriminants specialised in the rejection of electrons mis-identified as hadronically decaying tau leptons. An electron veto based on BDTs makes use of these discriminants and is optimised using simulated $Z \to \tau\tau$ events for the signal and $Z \to ee$ events for the background. The dependence of the signal and background efficiency of the electron veto on transverse momentum is shown in Figure 6.5. The e-veto BDT working points target signal efficiencies of 95%, 85% and 75%, respectively. Background rejection factors of 1/10 for signal efficiencies of 95% are achieved for 1-prong taus [101].

The tau candidates passing the cuts listed in Table 6.6 and the overlap removal scheme explained in Section 6.1 are considered as baseline taus.

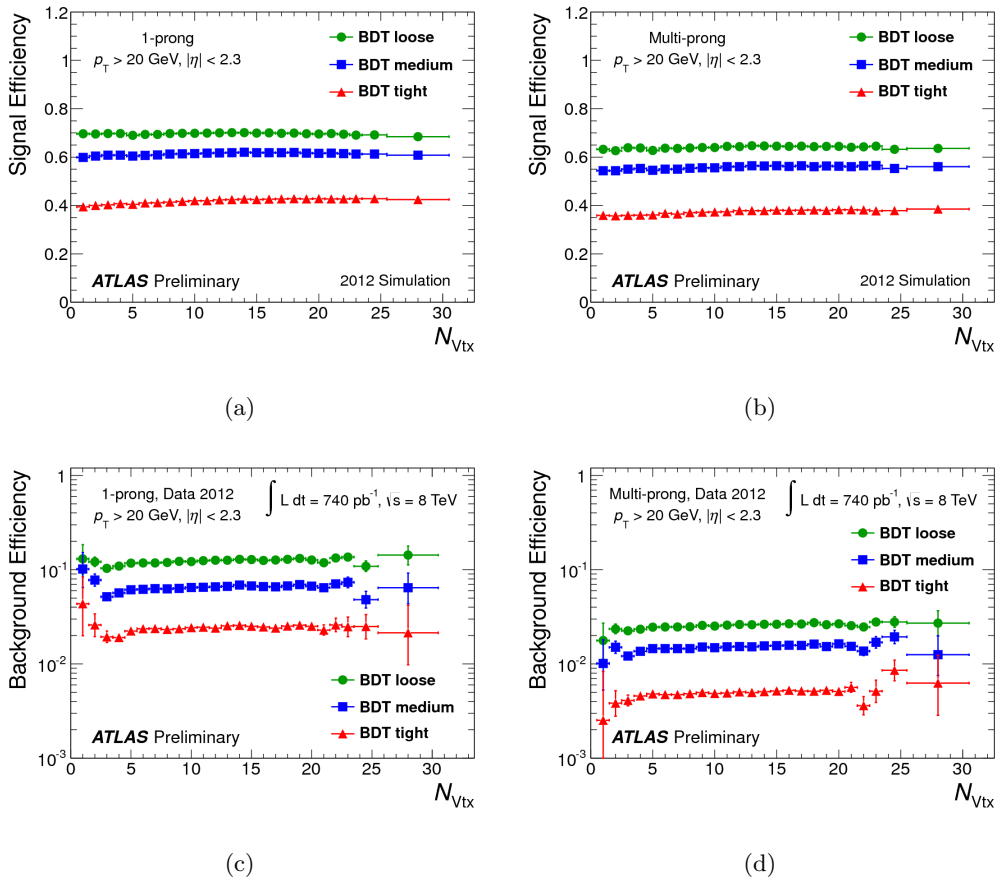

Figure 6.4: Signal (top) and background (bottom) efficiencies for 1-prong (left) and multi-prong (right) τ_{had} using simulated $Z \to \tau\tau$ and $W \to \tau\nu$ as signal samples and a jet background sample selected from 2012 data [101].

The BDT method explained previously is used to provide further discrimination against jets and electrons. Moreover, a cut-based muon veto is used to reject candidates with hits in the MS. The set of requirements used to define signal taus are summarised in Table 6.7.

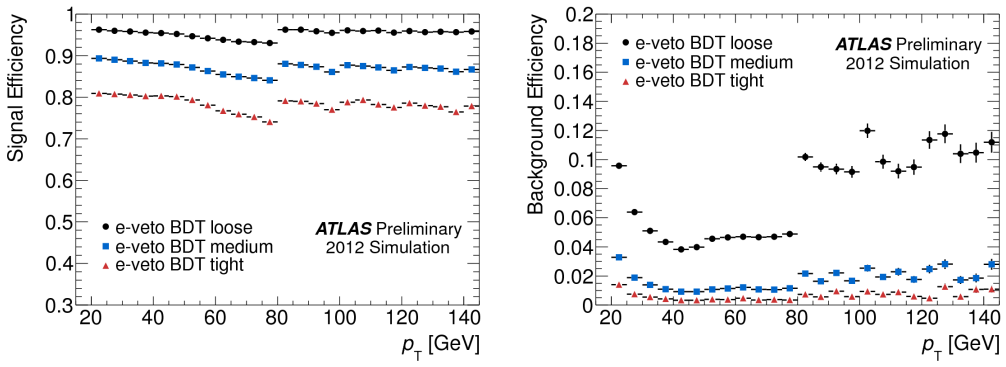

(a) (b)

Figure 6.5: Signal (left) and background (right) efficiencies for 1-prong τ_{had} using simulated $Z \to \tau\tau$ as signal sample and $Z \to ee$ as background sample selected from 2012 data [101]. The sudden change of the efficiency at 80 GeV is due to a different pile-up correction applied to one of the calorimeter variables below and above this threshold.

Table 6.6: Baseline selection criteria for hadronic taus.

Baseline Cuts	**Definition**
$p_{\mathrm{T}} > 20$ GeV	Tau transverse momentum requirement.
$\lvert\eta\rvert < 2.5$	Pseudorapidity range for the calorimeters.
$n_{tracks} = 1$ *or* 3	Number of associated charged tracks.
the tau charge must be ± 1	Charge (derived from the tracks) requirement on the tau candidate.

Table 6.7: Signal selection criteria for hadronic taus.

Signal Cuts	**Definition**
JetBDTSigMedium=1	"Medium" jet BDT score.
EleBDTLoose=0,	"Loose" electron veto BDT score (only for 1-prong tau candidates).
muonVeto=0	muon veto

6.2.5 Missing Transverse Energy

The missing transverse energy, $\vec{E}_{\mathrm{T}}^{\mathrm{miss}}$, is defined as the momentum imbalance in the plane transverse to the beam axis due to neutrinos and other weakly-interacting particles:

$$E_{\mathrm{T}}^{\mathrm{miss}} = \sqrt{\left(E_{(\mathrm{x})}^{\mathrm{miss}}\right)^2 + \left(E_{(\mathrm{y})}^{\mathrm{miss}}\right)^2}. \tag{6.3}$$

The calculation of $\vec{E}_{\mathrm{T}}^{\mathrm{miss}}$ uses the reconstructed physics objects discussed in Section 4.3.

The vector sum of transverse energy in the calorimeters, as well as tracks measured in the muon spectrometer defines the missing transverse energy of the event:

$$E_{(\mathrm{x,y})}^{\mathrm{miss}} = E_{(\mathrm{x,y})}^{\mathrm{miss,\ calo}} + E_{(\mathrm{x,y})}^{\mathrm{miss,\ }\mu}, \tag{6.4}$$

where the muon component is calculated by summing over muon track momenta (within $|\eta| < 2.7$):

$$E_{(\mathrm{x,y})}^{\mathrm{miss,\ }\mu} = -\sum p_{(x,y)}^{\mu}. \tag{6.5}$$

The calorimeter term, $E_{(\mathrm{x,y})}^{\mathrm{miss,\ calo}}$, is defined as

$$\begin{aligned} E_{(\mathrm{x,y})}^{\mathrm{miss,\ calo}} = E_{(\mathrm{x,y})}^{\mathrm{miss,\ }e} + E_{(\mathrm{x,y})}^{\mathrm{miss,\ }\gamma} + E_{(\mathrm{x,y})}^{\mathrm{miss,\ }\tau} + E_{(\mathrm{x,y})}^{\mathrm{miss,\ jets}} \\ + E_{(\mathrm{x,y})}^{\mathrm{miss,\ }cellOut} + E_{(\mathrm{x,y})}^{\mathrm{miss,\ }\mu(\mathrm{calo})}, \end{aligned} \tag{6.6}$$

where the $E_{(\mathrm{x,y})}^{\mathrm{miss,\ }e}$, $E_{(\mathrm{x,y})}^{\mathrm{miss,\ }\gamma}$ and $E_{(\mathrm{x,y})}^{\mathrm{miss,\ }\tau}$ terms are calculated from energy deposits in the calorimeter cells associated to electrons, photons and hadronic taus, respectively. The muon term $E_{(\mathrm{x,y})}^{\mathrm{miss,\ }\mu(\mathrm{calo})}$ is calculated from the energy loss of all muons in the calorimeters (the energy deposits from isolated muons are not taken into account to avoid double-counting of the muon energy). The jet term $E_{(\mathrm{x,y})}^{\mathrm{miss,\ jets}}$ is calculated using jets with local calibration applied, and with $p_{\mathrm{T}} > 20$ GeV. Any cells in clusters associated to jets with softer p_{T} (7 GeV$< p_{\mathrm{T}} <$ 20 GeV) and the remaining low energy calorimeter deposits (within $|\eta| < 4.9$) not associated with any of the above objects form the cell out term ($E_{(\mathrm{x,y})}^{\mathrm{miss,\ }cellOut}$) [102].

Hadronic taus are not distinguished from jets, hence, they are accounted in the $\vec{E}_{\mathrm{T}}^{\mathrm{miss}}$ calculation as jets, which provides a stable $\vec{E}_{\mathrm{T}}^{\mathrm{miss}}$ description, corresponding to "Egamma10NoTau RefFinal", which takes as input all baseline objects (without overlap removal being performed on them) defined previously in this chapter. This is defined as

$$\begin{aligned} E_{(\mathrm{x,y})}^{\mathrm{miss}} = E_{(\mathrm{x,y})}^{\mathrm{miss,\ }e} + E_{(\mathrm{x,y})}^{\mathrm{miss,\ }\gamma} + E_{(\mathrm{x,y})}^{\mathrm{miss,\ jets}} \\ + E_{(\mathrm{x,y})}^{\mathrm{miss,\ }cellOut} + E_{(\mathrm{x,y})}^{\mathrm{miss,\ }\mu(\mathrm{calo})} - \sum p_{(x,y)}^{\mu}. \end{aligned} \tag{6.7}$$

Chapter 7

SUSY Searches in Three Lepton Final States

Direct electroweak production of charginos ($\tilde{\chi}^{\pm}_{i=1,2}$) and neutralinos ($\tilde{\chi}^{0}_{j=1,2,3,4}$) can lead to leptons in the final state, missing energy and very low hadronic activity.

This chapter presents the search strategies developed in this thesis which particularly focus on direct production of $\tilde{\chi}^{\pm}_1\tilde{\chi}^0_2$ decaying to three leptons and missing energy using the complete ATLAS dataset collected during the 2012 LHC run at 8 TeV centre-of-mass energy. Each of the intermediate particles in the decay chain of $\tilde{\chi}^{\pm}_1\tilde{\chi}^0_2$ pair production into three leptons ($e/\mu/\tau$) can provide different SUSY scenarios. All scenarios described in Section 2.2.1 are considered for this search, where the $\tilde{\chi}^{\pm}_1\tilde{\chi}^0_2$ decays are mediated by production of WZ, Wh, $\tilde{\ell}$ or $\tilde{\tau}$ particles.

7.1 The 2012 Data

In 2012, the LHC delivered pp collisions at a centre-of-mass energy of $\sqrt{s} = 8$ TeV, corresponding to a total integrated luminosity of 22.8 fb^{-1}, and a total luminosity recorded by the ATLAS detector equivalent to 21.3 fb^{-1}. "Data-quality" criteria are imposed to the 2012 data collected by ATLAS [1], which take into account possible hardware and data-taking problems by the various ATLAS sub-systems. The resulting data used for this analysis corresponds to a total integrated luminosity of 20.3 fb^{-1}. The evolution of the 8 TeV cumulative integrated ATLAS luminosity as a function of time is shown in Figure 7.1.

The improvements to the instantaneous luminosity from year to year were due to increases in the number of proton bunches in each beam, increases in the number of

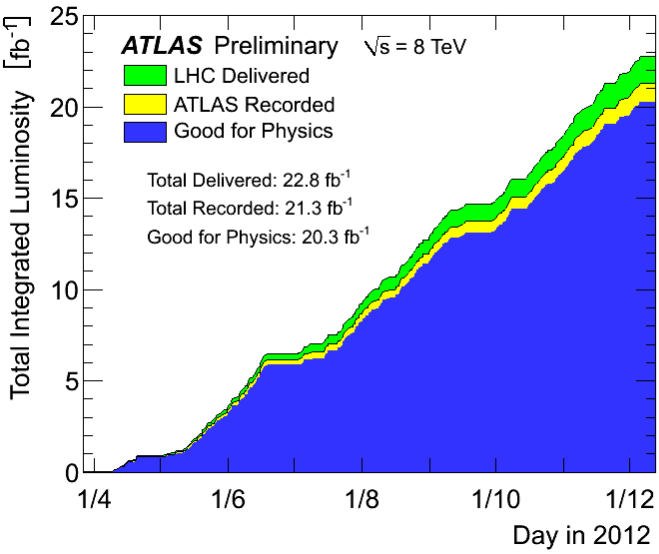

Figure 7.1: Total integrated luminosity in the 2012 LHC run. Cumulative luminosity versus time delivered to the LHC (green), recorded by ATLAS (yellow), and certified to be "good quality" data for ATLAS analyses (blue) during stable beams and for pp collisions at 8 TeV centre-of-mass energy in 2012.

protons per bunch, and improvements in beam focusing.

7.2 Analysis Strategy and Personal Contribution

The three lepton search is designed to select events containing charginos and neutralinos from events due to SM processes. Trilepton events are selected based on the object identification criteria discussed in Chapter 6. Events are required to pass further quality selection criteria (detailed in Section 7.3), as well as the trigger requirements described in Section 7.3.1. After all quality requirements are satisfied, the search for "interesting" events begins by defining "signal regions" where signal events are maximised over contribution from SM background events (see Section 7.4). At the same time, "validation regions" are identified, dominated almost exclusively by SM backgrounds, where the contribution of the different SM events are estimated. The results are discussed in Chapter 8.

Throughout this document, signal electrons and muons are labelled as ℓ or ℓ' where the flavour of ℓ and ℓ' is assumed to be different, whereas signal hadronic taus are denoted as τ for simplicity.

Personal contribution

I had the responsibility within the ATLAS multilepton SUSY analysis to add the hadronic tau final states as part of the three lepton analysis, which have been proven to be very important for an increase in sensitivity with respect to channels with only light leptons (e/μ) previously studied [103, 104, 105].

I was responsible for defining new signal regions (defined in Section 7.4 as SR0τb, SR1τ, SR2τa/b) with the purpose of enhancing the signal contribution of the newly explored SUSY scenarios with $\tilde{\chi}_1^{\pm}\tilde{\chi}_2^0$ pair production with decays into three leptons mediated by Wh or $\tilde{\tau}$. I also contributed to the MC-based estimation and modelling of the main SM backgrounds in the signal regions mentioned above and in dedicated Validation Regions (VR) where the signal contamination is low, defined in Section 7.5 as VR1τa/b and VR2τa/b. Details of the thorough modelling of the event kinematics in these VRs can be found in Section 7.5. I evaluated the main systematic uncertainties, e.g. theoretical cross section uncertainty and lepton identification systematics, on the SM backgrounds for the signal regions stated above, as well as those related to the PDF sets for all signal regions, and the experimental systematics. I have been responsible for the setting of the mass exclusion limits for four new SUSY models: two simplified models (the $\tilde{\tau}$- and Wh-mediated) and two pMSSM models (dominated by no-$\tilde{\ell}$ and $\tilde{\tau}$ decays). These results are detailed in Chapter 8.

A paper summarising the results of these searches was published in the Journal of High Energy Physics (JHEP) in April 2014 [1]. This paper contains the first SUSY results from the ATLAS collaboration which include the SM Higgs.

7.3 Event pre-selection

7.3.1 Triggers

This analysis makes use of single-isolated light lepton triggers as well as di-lepton triggers, listed in Table 7.1. The selected events in this analysis are required to pass any of these light-lepton trigger chains. A logical OR of the triggers is used to enhance the trigger selection efficiencies. To ensure that trigger efficiency is independent of the p_{T} of the leptons, events are required to have a p_{T} above a specific threshold for each trigger chain, also listed in Table 7.1. Figure 7.2 shows an example of the "turn-on curve" for one of the single-muon triggers used in this trigger menu, where the plateau is reached at $\sim$25 GeV, which is the threshold selected for this trigger chain. The p_{T} thresholds are also chosen

such that the overall trigger efficiency with respect to the selected events is above 90%, and is independent of the lepton p_{T} [106].

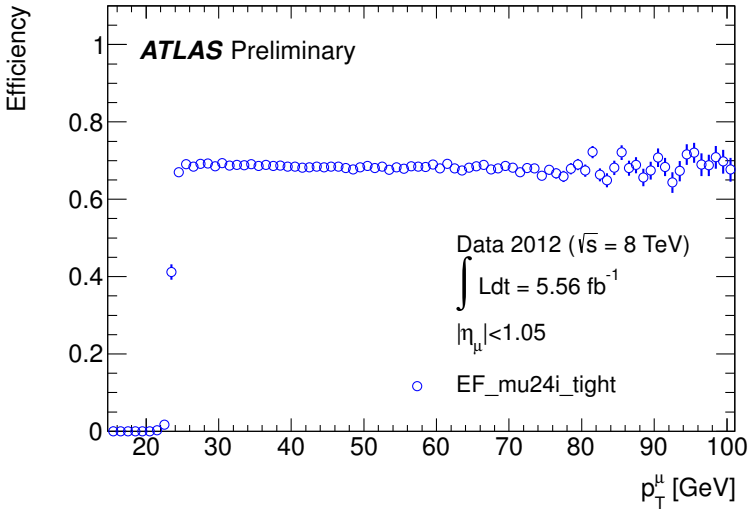

Figure 7.2: Efficiency of the single muon trigger (EF_mu24i_tight) with respect to offline reconstructed isolated muons as a function of p_{T} for the barrel region. The tag-and-probe method in $Z \to \mu\mu$ events was used to derive these efficiencies. The vertical error bars in the figure represent the statistical errors. The amount of data used corresponds to 5.56 fb^{-1} [107].

Any event overlap in the data streams is removed by requiring that events in the "EGamma" stream were triggered by the "EGamma-triggers" (specified in table 7.1) and any events in the "Muons" stream fail to pass the "EGamma-triggers" and pass the "Muons-triggers" instead. The same requirements are applied to the MC-simulated events (in MC simulated data events are not duplicated so no overlap removal is needed).

The ATLAS hadronic tau triggers use a tau identification criteria that is tighter than the signal tau selection used in this analysis, see Section 6.2.4. Therefore, only triggers based on light leptons are used to trigger events.

The trigger performance has been studied in detail in ref. [106], where the electron (muon) trigger efficiencies are measured by using the tag-and-probe method on $Z \to ee$ ($Z \to \mu\mu$) events. In particular, the three-lepton analysis team performed similar studies to show the agreement between the trigger performance in data and MC simulation for all single and double triggers, where it is seen that discrepancies are smaller than 2%. A conservative systematic of 5% is applied to account for these differences seen between the trigger in data and simulation.

Table 7.1: The trigger chains used and the offline p_{T} threshold used ensuring that the lepton(s) triggering the event are in the plateau region of the trigger efficiency.

Trigger	Detail	Stream	offline threshold [GeV]
Single Isolated e	e24vhi_medium1	EGamma	25
Single Isolated μ	mu24i_tight	Muons	25
Double e	2e12Tvh_loose1	EGamma	14,14
	e24vh_medium1_e7_medium1	EGamma	25,10
Double μ	2mu13	Muons	14,14
	mu18_tight_mu8_EFFS	Muons	18,10
Combined $e\mu$	e12Tvh_medium1_mu8	EGamma	14,10
	mu18_tight_e7_medium1	Muons	18,10

Event Quality Requirements

All events must have exactly three signal leptons ($e/\mu/\tau$), as in Chapter 6. Data are selected if one or more of the signal light leptons in the event matches one of the light lepton triggers and is within $\Delta R < 0.15$ from the relevant trigger object. Furthermore, there are requirements which are applied to reject events that might suffer from reconstruction problems, such as, jets which do not originate from hard scattering events [108] and fake missing transverse energy in the event originating from instrumental effects (e.g. detector noise), cosmic ray muons, non-operational detector parts. All events are required to have a primary vertex with five or more associated good tracks. In addition, well-isolated muons in the event which also satisfy $|z_0| < 1$ mm or $|d_0| < 0.2$ mm are required to suppress cosmic rays; and events with muons that may be mis-measured in charge (q) and/or momentum (p) in the ID are discarded if they satisfy: $\frac{\sigma_{q/p}}{|q/p|} \geq 0.2$.

7.4 Signal Region Definition and Optimisation

Five main signal regions (SR) are defined according to the flavour and charge of the leptons surviving pre-selection. The hadronic tau multiplicity drives the categorisation of the signal regions in: $3\ell + 0\tau$, $2\ell + 1\tau$ and $1\ell + 2\tau$ channels, where ℓ refers to electrons and muons only. Since no b-jets are expected in the final states studied, a veto on events containing b-tagged jets is applied in all signal regions. All signal regions have a high missing transverse energy requirement of at least 50 GeV.

Signal regions are defined by varying the requirements on selected kinematic variables to maximise the signal significance, Z_N [109], defined as:

$$Z_N = \sqrt{2}\mathrm{erf}^{-1}(1 - 2p(S, B, \sigma_B)). \tag{7.1}$$

In this formula p indicates the probability to observe more data than the background-only hypothesis prediction (see Section 8.1 for more details); S and B are the number of expected signal and background events, respectively, in a given region; and σ_B corresponds to the uncertainty associated to the background yields. The uncertainty choice is driven by the available statistics for the dominating background in a given region, in the case of SR2τa, the backgrounds is largely dominated by reducible SM processes with poor statistics, hence a conservative 100% is used, and 30% is used for all other signal regions.

The requirements on the kinematic variables used to define the SRs are shown in Table 7.2. The optimisation process focuses on fixing a requirement of one of the kinematic variable at a time and varying the others in order to reduce SM background processes and preserve the signal events denoted throughout this document as "SM WH/staus $(m_{\tilde{\chi}_1^\pm}, m_{\tilde{\chi}_1^0})$" which refer to selected simplified model via $Wh/\tilde{\tau}$ benchmark points with various masses of $\tilde{\chi}_1^\pm$ and $\tilde{\chi}_1^0$. These requirements are chosen such that the significance value (z_N) for most signal benchmark points is optimal without statistical bias. For this reason, it is important to show the kinematic variable distribution before a requirement has been applied and also, the signal significance of a few benchmark points as the requirement on the variable itself is varied. The definition of signal regions and optimisation studies performed using MC-simulated data are detailed in the following paragraphs.

Table 7.2: Summary of the selection requirements for the signal regions. The SR0τa bin definitions are shown in Table 7.3. Energies, momenta and masses are given in units of GeV. The signal models targeted by the selection requirements are also shown.

Signal region	SR0τa	SR0τb	SR1τ	SR2τa	SR2τb
Flavour/sign	$\ell^+\ell^-\ell$, $\ell^+\ell^-\ell'$	$\ell^\pm\ell^\pm\ell'^\mp$	$\tau^\pm\ell^\mp\ell^\mp$, $\tau^\pm\ell^\mp\ell'^\mp$	$\tau\tau\ell$	$\tau^+\tau^-\ell$
b-tagged jet	veto	veto	veto	veto	veto
$\vec{E}_{\mathrm{T}}^{\mathrm{miss}}$	binned	> 50	> 50	> 50	> 60
Other	m_{SFOS} binned m_{T} binned	$p_{\mathrm{T}}^{3^{\mathrm{rd}}\ell} > 20$ $\Delta\phi_{\ell\ell'}^{\mathrm{min}} \leq 1.0$	$p_{\mathrm{T}}^{2^{\mathrm{nd}}\ell} > 30$ $\sum p_{\mathrm{T}}^{\ell} > 70$ $m_{\ell\tau} < 120$ m_{ee} Z veto	$m_{\mathrm{T2}}^{\mathrm{max}} > 100$	$\sum p_{\mathrm{T}}^{\tau} > 110$ $70 < m_{\tau\tau} < 120$
Target model	$\tilde{\ell}$,WZ-mediated	Wh-mediated	Wh-mediated	$\tilde{\tau}_L$-mediated	Wh-mediated

7.4.1 $3\ell + 0\tau$ channel

SR0τa ($\ell^+\ell^-\ell$, $\ell^+\ell^-\ell'$)

The presence of one same-flavour and opposite-charge (SFOS) light lepton pair is the first requirement for the definition of this SR. This is motivated by the expected final state of $\tilde{\chi}_1^\pm$ and $\tilde{\chi}_2^0$ decays shown in 7.2- 7.3 where the decay chains are mediated by $\tilde{\ell}_L$ and WZ particles, respectively.

$$\tilde{\chi}_1^\pm \tilde{\chi}_2^0 \to W^\pm \tilde{\chi}_1^0 Z \tilde{\chi}_1^0 \to \ell^\pm \nu \tilde{\chi}_1^0 \ell^\mp \ell^\pm \tilde{\chi}_1^0 \tag{7.2}$$

$$\tilde{\chi}_1^\pm \tilde{\chi}_2^0 \to \tilde{\ell}^\pm \nu \tilde{\ell}^\pm \ell^\mp \to \ell^\pm \tilde{\chi}_1^0 \nu \ell^\pm \tilde{\chi}_1^0 \ell^\mp \tag{7.3}$$

These decay modes have been studied in previous searches [103, 104, 105], where it was found that $E_{\mathrm{T}}^{\mathrm{miss}}$ and the "transverse" mass (m_{T}) are the most powerful discriminators. The variable m_{T} is defined using the p_{T} of the light lepton not part of the SFOS pair (with invariant mass closest to the mass of the Z boson) and the $E_{\mathrm{T}}^{\mathrm{miss}}$:

$$m_{\mathrm{T}}(\vec{p}_{\mathrm{T}}^{\,\ell}, \vec{p}_{\mathrm{T}}^{\,\mathrm{miss}}) = \sqrt{2 p_{\mathrm{T}}^{\ell} E_{\mathrm{T}}^{\mathrm{miss}} - 2 \vec{p}_{\mathrm{T}}^{\,\ell} \cdot \vec{p}_{\mathrm{T}}^{\,\mathrm{miss}}}. \tag{7.4}$$

A requirement on m_{T} will suppress the background from WZ SM processes, where it is expected that $m_{\mathrm{T}} \leq m_W$. This signal region is further subdivided in bins defined by the invariant mass of the SFOS lepton pair (m_{SFOS}) closest to the Z boson mass, the transverse mass m_{T}, and $E_{\mathrm{T}}^{\mathrm{miss}}$. Furthermore, events with trilepton invariant mass, $m_{3\ell}$, close to the Z boson mass ($|m_{3\ell} - m_Z|$ <10 GeV) are vetoed in bins 5, 9 and 13 to suppress contributions from Z boson decays with converted photons from final-state radiation, this is denoted in Table 7.3 as "3ℓ Z veto". The total list of bins considered is shown in Table 7.3.

The first step in the optimisation of this region consists of defining five bins in the m_{SFOS} as shown in the second column of Table 7.3. The chosen values of the selection requirements on m_{SFOS} have been found most favourable in a previous optimisation [103].

The first three and fifth m_{SFOS} bins are defined in order to maximise the sensitivity of the analysis to the $\tilde{\ell}_L$-mediated model as well as the WZ-mediated model where the Z boson is produced virtually (off-shell), analogous to the Z-depleted region in [103]. The fourth bin is defined to be sensitive to the WZ-mediated model, in analogy to the Z-enriched region in [103]. The WZ and $t\bar{t}$ backgrounds generally dominate the SR0τa bins in varying proportions, with WZ mainly dominating the bins for which m_{SFOS} is in the

Table 7.3: Summary of the bins in m_{SFOS}, m_{T}, and $E_{\text{T}}^{\text{miss}}$ for SR0τa.

SR0τa bin	m_{SFOS} [GeV]	m_{T} [GeV]	$E_{\text{T}}^{\text{miss}}$ [GeV]	3ℓ Z veto
1	12–40	0–80	50–90	no
2	12–40	0–80	> 90	no
3	12–40	> 80	50–75	no
4	12–40	> 80	> 75	no
5	40–60	0–80	50–75	yes
6	40–60	0–80	> 75	no
7	40–60	> 80	50–135	no
8	40–60	> 80	> 135	no
9	60–81.2	0–80	50–75	yes
10	60–81.2	> 80	50–75	no
11	60–81.2	0–110	> 75	no
12	60–81.2	> 110	> 75	no
13	81.2–101.2	0–110	50–90	yes
14	81.2–101.2	0–110	> 90	no
15	81.2–101.2	> 110	50–135	no
16	81.2–101.2	> 110	> 135	no
17	> 101.2	0–180	50–210	no
18	> 101.2	> 180	50–210	no
19	> 101.2	0–120	> 210	no
20	> 101.2	> 120	> 210	no

81.2 − −101.2 GeV range. Additionally, bins 5, 9, and 13 veto events with $m_{\ell\ell\ell}$ within 10 GeV of the Z boson mass in order to suppress SM background from $Z \to \ell\ell\ell$ processes where one lepton arises from a converted photon from final state radiation.

The values considered for the requirements on the m_{T} and $E_{\text{T}}^{\text{miss}}$ shown in Table 7.3 (third and fourth column, respectively) were found to be optimal in studies done within the trilepton analysis group.

SR0τb ($\ell^{\pm}\ell^{\pm}\ell'^{\mp}$)

This signal region is designed to be sensitive to the Wh-mediated scenario where the Higgs decays which can lead to light lepton final states are via intermediate WW and $\tau\tau$:

$$\tilde{\chi}_1^{\pm}\tilde{\chi}_2^0 \to W^{\pm}\tilde{\chi}_1^0 h\tilde{\chi}_1^0 \to \ell^{\pm}\tilde{\chi}_1^0\ell^{\mp}\ell^{\pm}\tilde{\chi}_1^0 + E_{\text{T}}^{\text{miss}}(\nu) \tag{7.5}$$

Figure 7.3 shows that the SM Higgs branching ratios (BR) of $h \to WW$ or $h \to \tau\tau$ processes is very low compared to others, such as $h \to bb$.

Events with a SFOS light lepton pair are vetoed to suppress WZ background, which is the main SM background process in this scenario. The optimisation process begins by

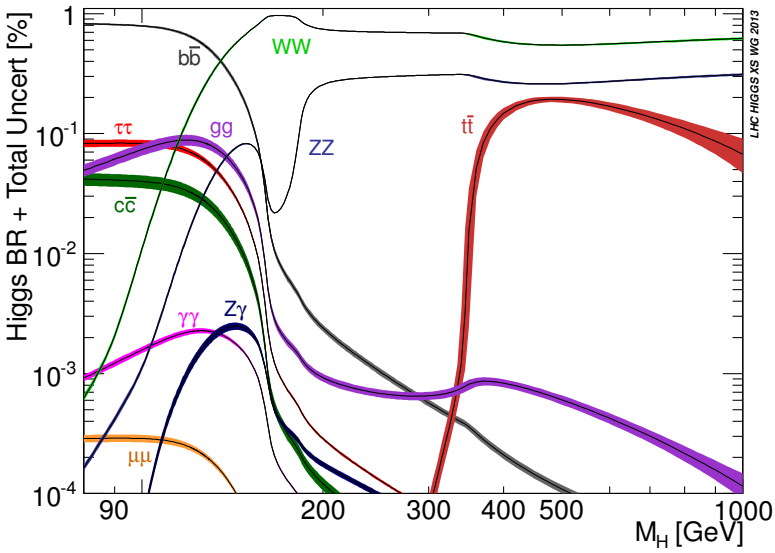

Figure 7.3: Standard Model Higgs boson decay branching ratios [110]

requiring high missing transverse energy to reduce WZ and $t\bar{t}$ contamination. Figure 7.4 shows the distribution of $E_{\mathrm{T}}^{\mathrm{miss}}$, which clearly peaks at around 50 GeV.

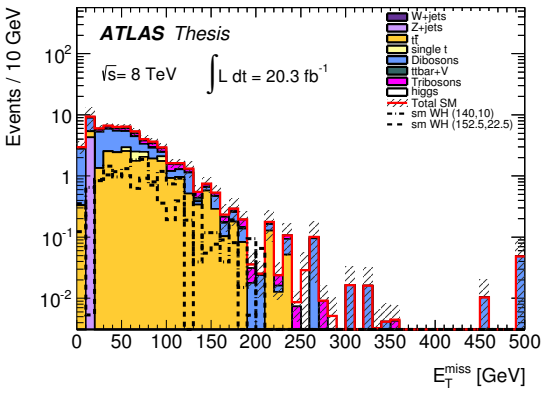

(a) SR0τb: $E_{\mathrm{T}}^{\mathrm{miss}}$

Figure 7.4: The $E_{\mathrm{T}}^{\mathrm{miss}}$ distribution after SFOS veto and a b-jet veto are applied. The chosen signal benchmark points shown correspond to simplified models via Wh with masses: $m_{\tilde{\chi}_1^\pm} = 140, 152.5$ GeV and $m_{\tilde{\chi}_1^0} = 10, 22.5$ GeV.

After the $E_{\mathrm{T}}^{\mathrm{miss}}$ requirement, the majority of the background is due to $t\bar{t}$ events, which have a low-p_{T} third-leading lepton from a leptonic b decay. The p_{T} distribution for the third-leading lepton is shown in Figure 7.5(a) alongside a plot 7.5(b) which shows that a cut at $p_{\mathrm{T}}^{3rd\ \ell} > 20$ GeV is optimal based on the Z_N values calculated for various signal benchmark points shown, which have been chosen based on their expected yields. Lastly, the $\Delta\phi$ angle between two opposite-sign (OS) light leptons (coming from the Higgs decay

according to the model) is studied. The minimum value out of all possible $\Delta\phi$ combinations between OS light-lepton pairs, $\Delta\phi_{\ell\ell'}^{\min}$, is shown in Figure 7.5(c). The signal events have opposite-sign leptons closer in ϕ space than the SM background events, which is relatively flat in $\Delta\phi_{\ell\ell'}^{\min}$. Therefore, a requirement of $\Delta\phi_{\ell\ell'}^{\min} \leq 1.0$ shows to be optimal (see Figure 7.5(d)).

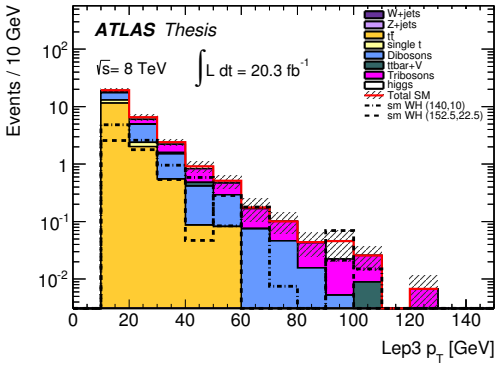

(a) SR0τb: $p_{\mathrm{T}}^{3rd\ \ell}$

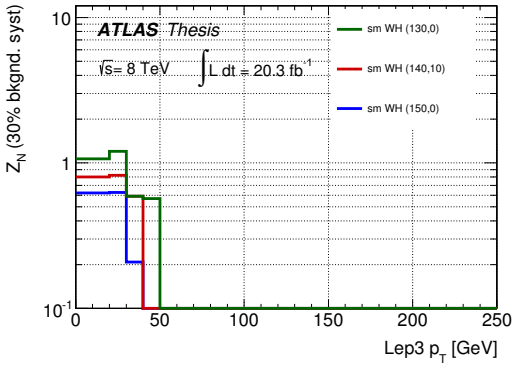

(b) SR0τb: $p_{\mathrm{T}}^{3rd\ \ell}$ optimisation

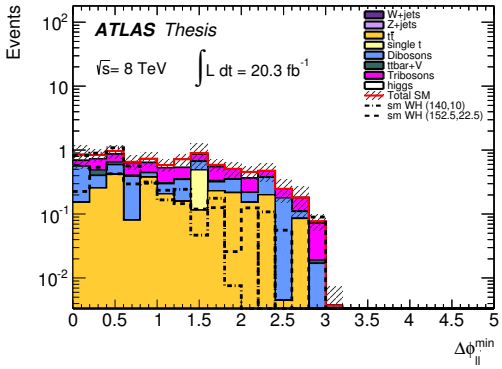

(c) SR0τb: $\Delta\phi_{\ell\ell'}^{\min}$

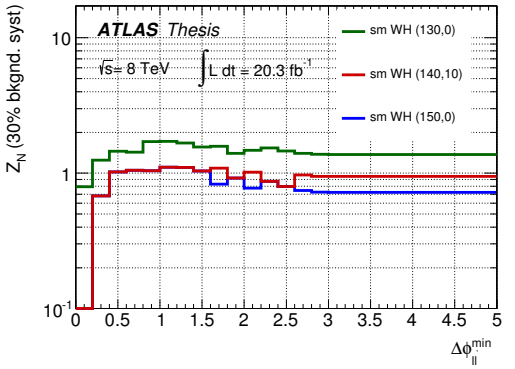

(d) SR0τb: $\Delta\phi_{\ell\ell'}^{\min}$ optimisation

Figure 7.5: The $p_{\mathrm{T}}^{3rd\ \ell}$ distribution after SFOS veto, b-jet veto and $E_{\mathrm{T}}^{\mathrm{miss}} > 50\,\mathrm{GeV}$ are applied (a). The $\Delta\phi_{\ell\ell'}^{\min}$ distribution after a veto on SFOS lepton pair, b-jet veto, $E_{\mathrm{T}}^{\mathrm{miss}} > 50\,\mathrm{GeV}$ and $p_{\mathrm{T}}^{3rd\ell} > 20$ GeV are applied (c). The signal significance is also shown for Wh SUSY benchmark points as the lower cut on $p_{\mathrm{T}}^{3rd\ \ell}$ (b) and upper cut on $\Delta\phi_{\ell\ell'}^{\min}$ (d) are varied. The chosen signal benchmark points shown correspond to simplified models via Wh with masses: $m_{\tilde{\chi}_1^\pm} = 140, 152.5(130, 140, 150)$ GeV and $m_{\tilde{\chi}_1^0} = 10, 22.5(0, 10, 0)$ GeV on the left (right) plots.

The remaining processes come from $t\bar{t}$ and VVV production and are estimated as discussed Section 7.5.

7.4.2 $2\ell + 1\tau$ channel

SR1τ ($\tau^{\pm}\ell^{\mp}\ell^{\mp}$, $\tau^{\pm}\ell^{\mp}\ell'^{\mp}$)

This signal region is designed to be sensitive to the Wh-mediated scenario, where one of the taus decays hadronically and the other leptonically:

$$\tilde{\chi}_1^{\pm}\tilde{\chi}_2^0 \to W^{\pm}\tilde{\chi}_1^0 h\tilde{\chi}_1^0 \to \ell^{\pm}\nu\tilde{\chi}_1^0\tau^{\mp}\tau^{\pm}\tilde{\chi}_1^0 \tag{7.6}$$

Because of the expected final state, the selection requires two same-sign (SS) signal electrons/muons and one signal hadronic tau with opposite charge.

A requirement on the invariant mass of the $\ell\tau$ pair, $m_{\ell\tau}$, closest to the Higgs boson mass of 125 GeV is made. Same-sign electron pairs with invariant mass consistent with a Z boson mass (81.2 GeV $< m_{ee} <$ 101.2 GeV) are vetoed to suppress events in which the charge of an electron is wrongly assigned due to a converting photon. This effect is rare in di-muon events due to the higher performance of combined-track information from the ID and MS at reconstruction level and also because muons undergo far less Bremsstrahlung than electrons. Figure 7.6 shows the effect of the Z-veto on the background yields, mainly coming from Z+jets processes.

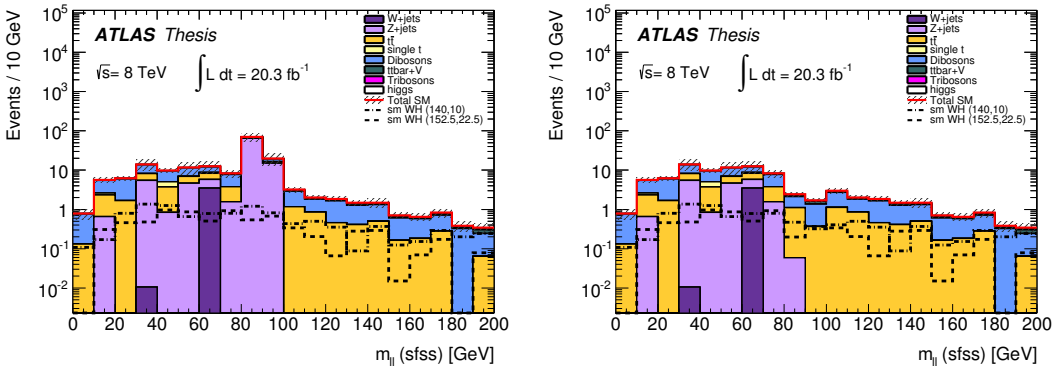

(a) SR1τ: $m_{\ell\ell}$ before $Z(\to ee)$ veto

(b) SR1τ: $m_{\ell\ell}$ after $Z(\to ee)$ veto

Figure 7.6: The $m_{\ell\tau}$ distribution (a) before and (b) after applying $Z(\to ee)$ veto for $\ell^{\pm}\ell^{\pm}\tau^{\mp}$ events, with $\ell = e/\mu$. The chosen signal benchmark points shown correspond to simplified models via Wh with masses: $m_{\tilde{\chi}_1^{\pm}} = 140, 152.5$ GeV and $m_{\tilde{\chi}_1^0} = 10, 22.5$ GeV on the plots.

Further signal optimisation is done by exploring the scalar sum of p_{T} of the two same-sign leptons, shown in Figure 7.7(a). A requirement on the sum of p_{T} of the light leptons ($\sum p_{\mathrm{T}}^{\ell} > 70$ GeV) seems to discriminate well against the SM processes, where the effect on the selected signal benchmark points can be seen in Figure 7.7(b).

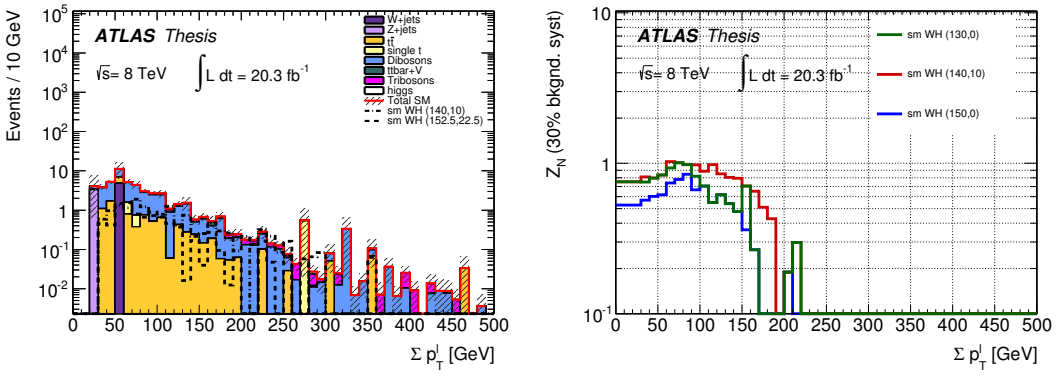

(a) SR1τ: $\sum p_{\mathrm{T}}^{\ell}$

(b) SR1τ: $\sum p_{\mathrm{T}}^{\ell}$ optimisation

Figure 7.7: The sum of the lepton p_{T} where b-jet veto, $Z(\rightarrow ee)$ veto and $E_{\mathrm{T}}^{\mathrm{miss}}$ requirements have been applied. The signal significance is also shown for Wh SUSY benchmark points as the lower cut on $\sum p_{\mathrm{T}}^{\ell}$ is varied.The chosen signal benchmark points shown correspond to simplified models via Wh with masses: $m_{\tilde{\chi}_1^{\pm}} = 140, 152.5(130, 140, 150)$ GeV and $m_{\tilde{\chi}_1^0} = 10, 22.5(0, 10, 0)$ GeV on the left (right) plots.

Once all of these requirements have been applied, the p_{T} of the sub-leading light lepton is investigated, as shown in Figure 7.8(a). The remaining contribution to the SM background, are mainly coming from diboson and $t\bar{t}$ processes, which have soft sub-leading leptons compared to the SUSY events considered. Therefore, the sub-leading light lepton in the event is required to have $p_{\mathrm{T}} > 30\,\mathrm{GeV}$ to discriminate against these SM backgrounds.

Due to missing neutrinos from the tau decays and the two LSP ($\tilde{\chi}_1^0$) in the event, the Higgs mass cannot be accurately measured. This can be seen in the distribution of the invariant mass of the hadronic tau and the leptonic tau candidate, assuming that the second leading light lepton comes from the $h \rightarrow \tau\tau$ decay, shown in Figure 7.9(a). A upper limit on the invariant mass of the lepton-tau pair ($m_{\ell\tau} < 120$ GeV) is chosen as the optimal requirement to remove SM contributions, mainly from diboson processes.

After these requirements are imposed, the diboson and $t\bar{t}$ processes dominate the remaining SM background.

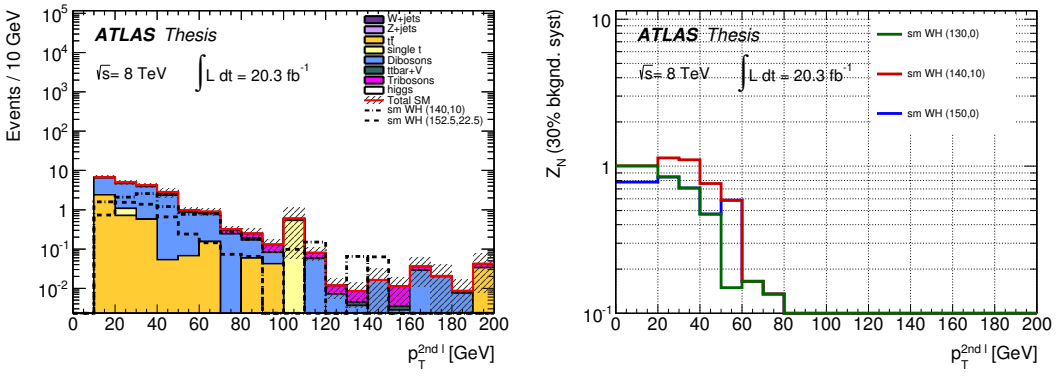

(a) SR1τ: $p_{\mathrm{T}}^{2^{\mathrm{nd}}\ell}$ (b) SR1τ: $p_{\mathrm{T}}^{2^{\mathrm{nd}}\ell}$ optimisation

Figure 7.8: The p_{T} of the sub-leading lepton in $\ell^{\pm}\ell^{\pm}\tau^{\mp}$ events where the b-jet veto, $Z(\rightarrow ee)$ veto, $E_{\mathrm{T}}^{\mathrm{miss}}$, $\sum p_{\mathrm{T}}^{\ell}$ requirements are applied. The distribution is shown in (a), while (b) shows the signal significance as a lower cut on $p_{\mathrm{T}}^{2^{\mathrm{nd}}\ell}$ is varied. The chosen signal benchmark points shown correspond to simplified models via Wh with masses: $m_{\tilde{\chi}_1^{\pm}} = 140, 152.5(130, 140, 150)$ GeV and $m_{\tilde{\chi}_1^0} = 10, 22.5(0, 10, 0)$ GeV on the left (right) plots.

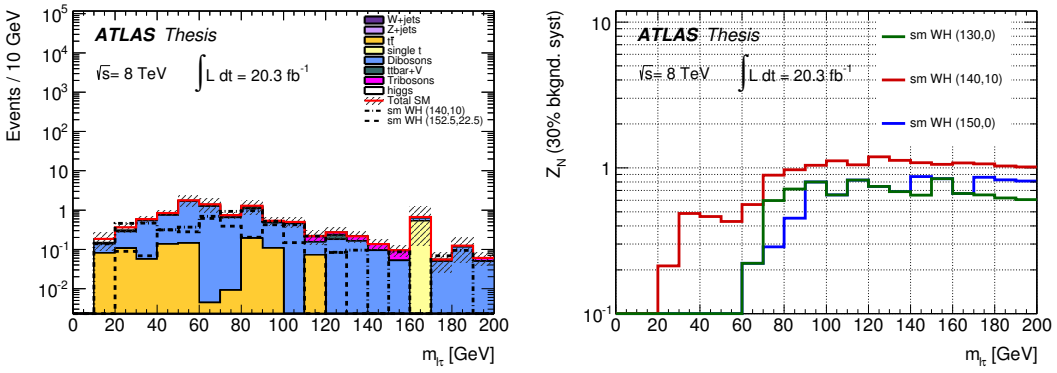

(a) SR1τ: $m_{\ell\tau}$ (b) SR1τ: $m_{\ell\tau}$ optimisation

Figure 7.9: The $m_{\ell\tau}$ distribution in $\ell^{\pm}\ell^{\pm}\tau^{\mp}$ events where the b-jet veto, $Z(\rightarrow ee)$ veto, $E_{\mathrm{T}}^{\mathrm{miss}}$ and $\sum p_{\mathrm{T}}^{\ell}$ and $p_{\mathrm{T}}^{2^{\mathrm{nd}}\ell}$ requirements are applied. The signal significance Z_N for Wh SUSY benchmark points as the upper threshold on $m_{\ell\tau}$ is varied (b). The chosen signal benchmark points shown correspond to simplified models via Wh with masses: $m_{\tilde{\chi}_1^{\pm}} = 140, 152.5(130, 140, 150)$ GeV and $m_{\tilde{\chi}_1^0} = 10, 22.5(0, 10, 0)$ GeV on the left (right) plots.

7.4.3 $1\ell + 2\tau$ channel

SR2τa ($\tau_{had}\tau_{had}\ell$)

This signal region is sensitive to the $\tilde{\tau}_L$-mediated scenario, where the two tau leptons decay hadronically:

$$\tilde{\chi}_1^{\pm}\tilde{\chi}_2^0 \rightarrow \tilde{\tau}^{\pm}\nu_\tau\tilde{\tau}^{\pm}\tau^{\mp} \rightarrow \tau^{\pm}\tilde{\chi}_1^0\nu_\tau\tau^{\mp}\tilde{\chi}^0\tau^{\pm}. \tag{7.7}$$

In this SUSY scenario there are three leptons that can originate from the staus or directly from the $\tilde{\chi}_2^0$, making them indistinguishable.

Discrimination between SUSY signal and main SM backgrounds, such as, top and W+jets, is achieved using the "stransverse mass" variable, m_{T2} [111, 112]. This variable is designed to select events where there are particles decaying to one visible and one invisible object, e.g. $WW \rightarrow \ell\nu\ell\nu$ and $\tilde{\chi}_1^{\pm}\tilde{\chi}_2^0$ decays as in Equation 7.7.

The stransverse mass is defined as

$$m_{\mathrm{T2}} = \min_{\vec{q}_{\mathrm{T}}} \left[\max \left(m_{\mathrm{T}}(\vec{p}_{\mathrm{T},1},\, \vec{q}_{\mathrm{T}}), m_{\mathrm{T}}(\vec{p}_{\mathrm{T},2},\, \vec{p}_{\mathrm{T}}^{\,\mathrm{miss}} - \vec{q}_{\mathrm{T}}) \right) \right], \tag{7.8}$$

where $\vec{p}_{\mathrm{T},1}$ and $\vec{p}_{\mathrm{T},2}$ are the transverse momenta of the two visible objects and $\vec{q}_{\mathrm{T}}$ correspond to the transverse vector that minimises the larger of the two transverse masses. For signal events the m_{T2} end-point is correlated to the mass difference between the lightest chargino or next-to-lightest neutralino and the LSP. For large values of this difference, the m_{T2} distribution for signal events extends significantly beyond the distributions of the SM background events which have in this case have a kinematic upper end-point at around the mass of the decaying particle. Therefore, events in this SR are selected requiring that they have high $E_{\mathrm{T}}^{\mathrm{miss}}$ and high "maximum stransverse mass" $m_{\mathrm{T2}}^{\mathrm{max}}$, where $m_{\mathrm{T2}}^{\mathrm{max}}$ is formed by taking the largest m_{T2} value out of all possible combinations of $\ell, \tau, E_{\mathrm{T}}^{\mathrm{miss}}$ and $\tau, \tau, E_{\mathrm{T}}^{\mathrm{miss}}$ taken as input for the calculation. No charge requirement is made on any of the three leptons.

The optimisation process is done by looking at the $E_{\mathrm{T}}^{\mathrm{miss}}$ and $m_{\mathrm{T2}}^{\mathrm{max}}$ distributions, as shown in Figure 7.10. The chosen SUSY signal points shown on the plots, characterise the main features of the $\tilde{\tau}_L$-mediated scenario. This signal region is defined by having a minimum requirement on the $E_{\mathrm{T}}^{\mathrm{miss}}$ ($E_{\mathrm{T}}^{\mathrm{miss}} > 50\,\mathrm{GeV}$) and a large $m_{\mathrm{T2}}^{\mathrm{max}}$ cut ($m_{\mathrm{T2}}^{\mathrm{max}} >$ 100 GeV), in order to reduce background events coming from V+jets processes, which lie at values below ~100 GeV.

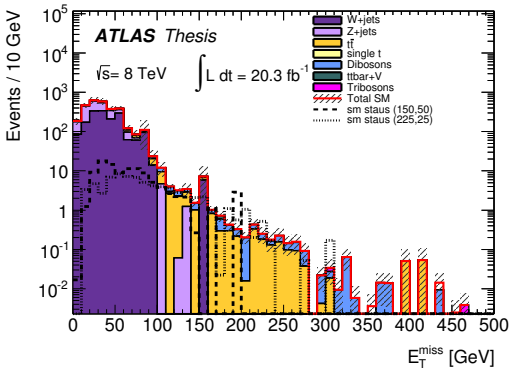

(a) SR2τa: $E_{\mathrm{T}}^{\mathrm{miss}}$

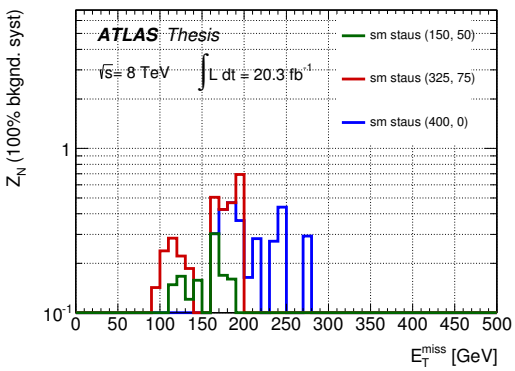

(b) SR2τa: $E_{\mathrm{T}}^{\mathrm{miss}}$ optimisation

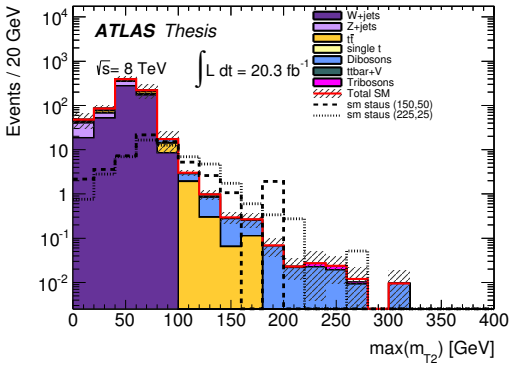

(c) SR2τa: $m_{\mathrm{T2}}^{\mathrm{max}}$

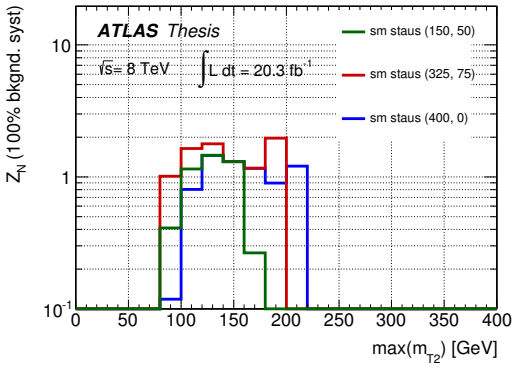

(d) SR2τa: $m_{\mathrm{T2}}^{\mathrm{max}}$ optimisation

Figure 7.10: The $E_{\mathrm{T}}^{\mathrm{miss}}$ distribution in $1\ell{+}2\tau$ events where b-jet veto is applied (a). The $m_{\mathrm{T2}}^{\mathrm{max}}$ distribution in $1\ell{+}2\tau$ events where a b-jet veto and $E_{\mathrm{T}}^{\mathrm{miss}} > 50$ GeV is applied (c). The signal significance for $\tilde{\tau}$ SUSY benchmark points as a lower cut on $E_{\mathrm{T}}^{\mathrm{miss}}$ (b) and $m_{\mathrm{T2}}^{\mathrm{max}}$ (d) is varied. The chosen signal benchmark points shown correspond to simplified models via $\tilde{\tau}$ with masses: $m_{\tilde{\chi}_1^{\pm}} = 150, 225(150, 325, 400)$ GeV and $m_{\tilde{\chi}_1^0} = 50, 25(50, 75, 0)$ GeV on the left (right) plots.

SR2τb ($\tau^+\tau^-\ell$)

This signal region is sensitive to the Wh-mediated scenario shown in Equation 7.6, where the two tau leptons decay hadronically. Therefore, selected events are required to have two opposite-sign hadronic taus and one light signal lepton.

A high $E_{\mathrm{T}}^{\mathrm{miss}}$ requirement of 60 GeV is used to reduce contributions from V+jets processes. The missing transverse energy for events with $\ell\tau^+\tau^-$ and a b-jet veto is shown in Figure 7.11(a). The effect on the signal significance can be seen in Figure 7.11(b), where a cut of $E_{\mathrm{T}}^{\mathrm{miss}} > 60$ GeV is shown to be optimal for the SUSY benchmark points with highest yields.

The di-tau invariant mass, $m_{\tau\tau}$, is calculated for events passing the $E_{\mathrm{T}}^{\mathrm{miss}}$ requirement

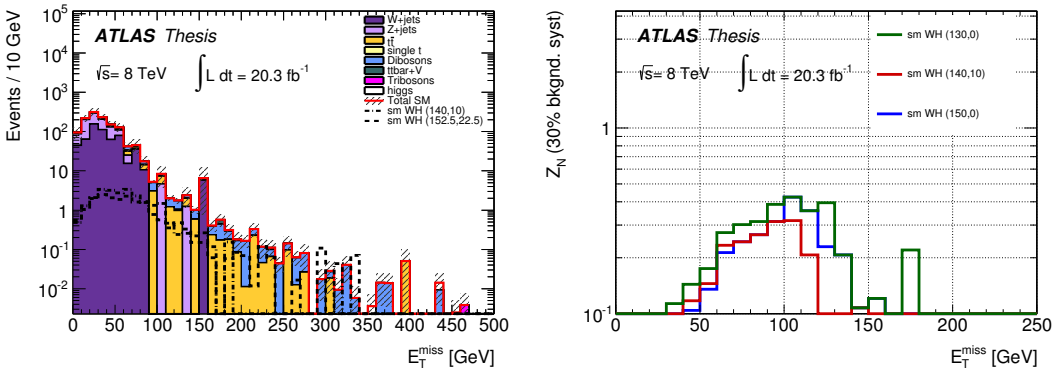

(a) SR2τb: $E_{\mathrm{T}}^{\mathrm{miss}}$ (b) SR2τb: $E_{\mathrm{T}}^{\mathrm{miss}}$ optimisation

Figure 7.11: The $E_{\mathrm{T}}^{\mathrm{miss}}$ distribution in $\ell\tau^{+}\tau^{-}$ events where b-jet veto is applied (a). The signal significance Z_N for Wh SUSY benchmark points as a lower cut on $E_{\mathrm{T}}^{\mathrm{miss}}$ is varied (b). The chosen signal benchmark points shown correspond to simplified models via Wh with masses: $m_{\tilde{\chi}_1^{\pm}} = 140, 152.5(130, 140, 150)$ GeV and $m_{\tilde{\chi}_1^0} = 10, 22.5(0, 10, 0)$ GeV on the left (right) plots.

(see Figure 7.12). Due to escaping neutrinos in the event, the peak of the $m_{\tau\tau}$ is lower than the Higgs mass at 125 GeV. The WZ and ZZ backgrounds have broad $m_{\tau\tau}$ values below the Z mass. Upper and lower requirements on $m_{\tau\tau}$ can reduce contamination from backgrounds with Z bosons due to the mass difference between Z and H boson (~ 30 GeV). This signal region is required to have $m_{\tau\tau}$ in the mass window 70–120 GeV to mainly reduce such diboson background contributions. Furthermore, the scalar sum of p_{T} of the two hadronic taus in the event is investigated and its distribution shown in Figure 7.13. The SUSY events tend to have larger total energy than the SM events, due to the higher mass of the particles, and result in particles with large momenta in the final state for SUSY signals. A requirement on the sum of p_{T} of the two hadronic taus ($\sum p_{\mathrm{T}}^{\tau} > 110$ GeV) discriminates well against SM background coming from V+jets processes.

The remaining backgrounds surviving the SR2τb selection are due to diboson and $t\bar{t}$ processes.

7.5 Background Estimation

Several SM processes can lead to events with three leptons in the final state and therefore enter the signal regions as background contamination. All lepton candidates ($e/\mu/\tau$) in the events entering the SR can be categorised according to the process they originate

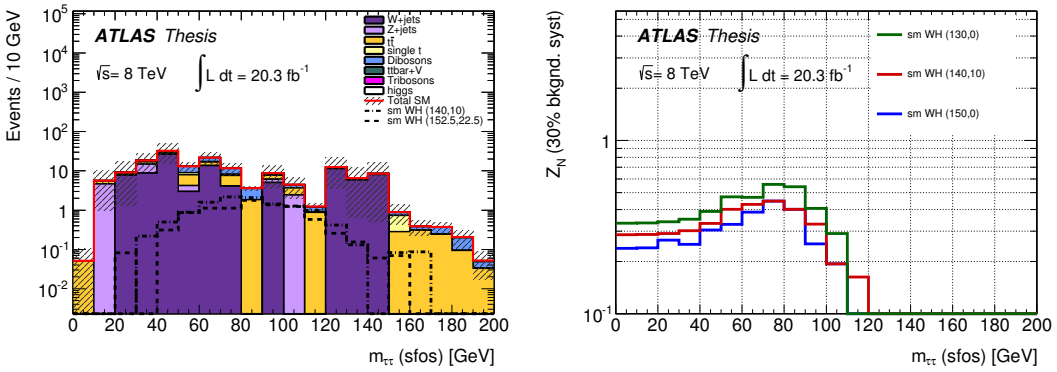

(a) SR2τb: $m_{\tau\tau}$

(b) SR2τb: $m_{\tau\tau}$ optimisation

Figure 7.12: The $m_{\tau\tau}$ distribution in for $\ell\tau^+\tau^-$ events where the b-jet veto and $E_{\mathrm{T}}^{\mathrm{miss}}$ requirements are applied. The signal significance Z_N for Wh SUSY benchmark points as the lower threshold on $m_{\tau\tau}$ is varied (b). The chosen signal benchmark points shown correspond to simplified models via Wh with masses: $m_{\tilde{\chi}_1^\pm} = 140, 152.5(130, 140, 150)$ GeV and $m_{\tilde{\chi}_1^0} = 10, 22.5(0, 10, 0)$ GeV on the left (right) plots.

from using MC-simulated data. These categories are: "real" leptons, which are prompt and isolates, and originate from W, Z, h and τ decays; and "fake" leptons, which can originate from a mis-identified light-flavour quark or gluon jet. Real leptons that are non-prompt are considered as fake leptons since they can originate from a semi-leptonic decay of a heavy-flavour quark, or an electron from a Bremsstrahlung photon conversion.

Figure 7.14 shows the origin of the lepton candidates passing signal regions selection using MC simulated background processes categorised as either "Top" or "Boson". "Boson" processes accounts for contributions coming from dibosons, tribosons, W/Z+jets and Higgs (ggF/VBF/WH/ZH) backgrounds; and the "Top" processes accounts for contributions coming from $t\bar{t}$, $t\bar{t}+V$, single-t and Higgs ($t\bar{t}H$). Electrons and muons mainly originate from a prompt decay, whereas hadronic taus are mainly fakes originating from heavy flavour and light flavour jet decays.

Based on whether leptons are real or fake, SM processes are classified into *irreducible background* (all leptons in the events are real) and *reducible background* (events with at least one fake lepton). This section describes how the background contribution in the signal regions is estimated, by using data-driven techniques for the reducible processes and MC-based techniques for the irreducible processes. The predictions for irreducible and reducible backgrounds, discussed in 7.5.1 and 7.5.2 respectively, are tested in validation regions (section 7.5.3) by comparing them to what is seen directly from the real data in kinematic regions that are close yet disjoint from SRs.

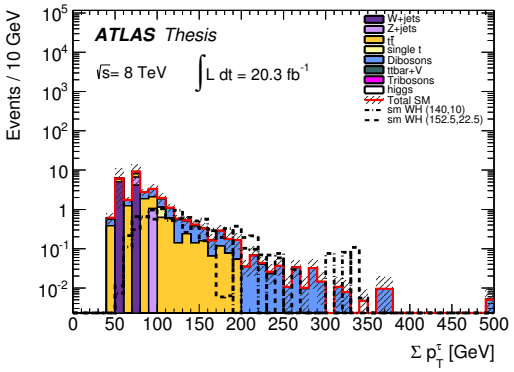

(a) SR2τb: $\sum p_{\mathrm{T}}^{\tau}$

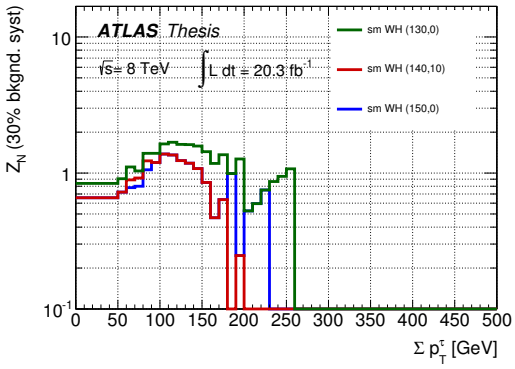

(b) SR2τb: $\sum p_{\mathrm{T}}^{\tau}$ optimisation

Figure 7.13: The $\sum p_{\mathrm{T}}^{\tau}$ distribution in for $\ell\tau^{+}\tau^{-}$ events where the b-jet veto, $E_{\mathrm{T}}^{\mathrm{miss}}$ and $m_{\tau\tau}$ requirements are applied (a). The signal significance Z_N for Wh SUSY benchmark points as the lower $\sum p_{\mathrm{T}}^{\tau}$ threshold is varied (b). The chosen signal benchmark points shown correspond to simplified models via Wh with masses: $m_{\tilde{\chi}_1^{\pm}} = 140, 152.5(130, 140, 150)$ GeV and $m_{\tilde{\chi}_1^0} = 10, 22.5(0, 10, 0)$ GeV on the left (right) plots.

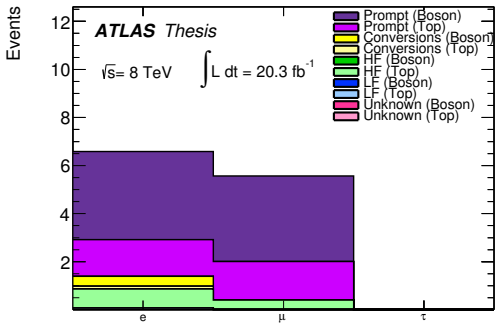

(a) SR0τb: e/μ

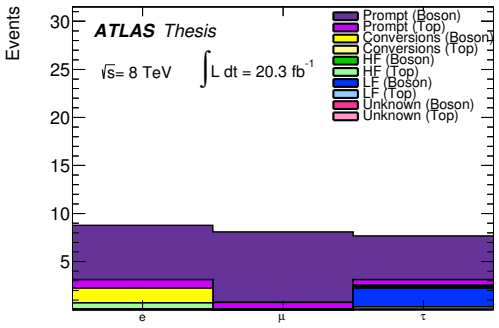

(b) SR1τ: $e/\mu/\tau$

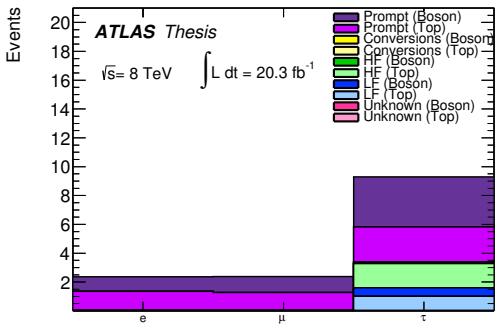

(c) SR2τa: $e/\mu/\tau$

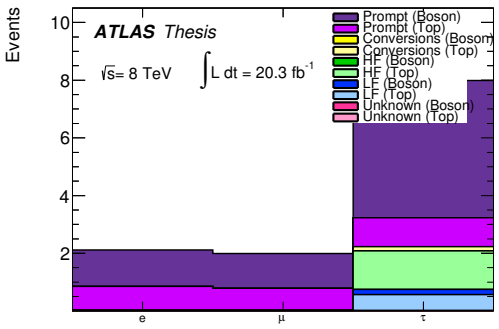

(d) SR2τb: $e/\mu/\tau$

Figure 7.14: Sources of electrons, muons and taus obtained from MC after all cuts in the signal regions.

7.5.1 Irreducible Background

The processes that form the irreducible background for this analysis are $WZ(/\gamma^*)$, $ZZ(/\gamma^*)$, $t\bar{t}+Z(/W/WW)$, tZ, VVV and Higgs boson production (ggF/VBF/WH/ZH). The MC-based estimates are shown in table 7.4 and indicate that WZ dominates the irreducible background in all SRs, except in SR0τb (where the optimisation uses a SFOS veto to specifically reject WZ events). In this SR is the VVV background is the one that dominates. All background estimates are determined using corresponding MC-simulated data, for which lepton ($e/\mu/\tau$) and b-jet selection efficiencies are corrected to account for differences with respect to the real data (more details in Section 7.6).

Table 7.4: Total irreducible background yields in the signal regions. The different components are derived purely from MC. All background contributions are normalised to 20.3 fb^{-1}. Uncertainties are statistical and systematic, as described in Section 7.6.

Sample	WZ	ZZ	$top + V$	VVV	Higgs
SR0τa-bin01	$13.2^{+3.4}_{-3.2}$	$1.4^{+0.6}_{-0.5}$	$0.14^{+0.05}_{-0.05}$	$0.33^{+0.33}_{-0.33}$	$0.66^{+0.26}_{-0.26}$
SR0τa-bin02	$3.0^{+1.4}_{-1.4}$	$0.12^{+0.06}_{-0.06}$	$0.07^{+0.04}_{-0.04}$	$0.0982^{+0.1015}_{-0.1016}$	$0.15^{+0.08}_{-0.08}$
SR0τa-bin03	$7.8^{+1.6}_{-1.6}$	$0.40^{+0.14}_{-0.14}$	$0.035^{+0.046}_{-0.047}$	$0.19^{+0.19}_{-0.19}$	$0.64^{+0.22}_{-0.22}$
SR0τa-bin04	$4.5^{+1.1}_{-1.0}$	$0.20^{+0.18}_{-0.18}$	$0.14^{+0.13}_{-0.13}$	$0.6^{+0.6}_{-0.6}$	$0.46^{+0.18}_{-0.17}$
SR0τa-bin05	$6.3^{+1.6}_{-1.6}$	$1.5^{+0.5}_{-0.5}$	$0.11^{+0.08}_{-0.08}$	$0.26^{+0.27}_{-0.27}$	$0.36^{+0.14}_{-0.15}$
SR0τa-bin06	$3.7^{+1.6}_{-1.6}$	$0.25^{+0.14}_{-0.11}$	$0.047^{+0.022}_{-0.021}$	$0.24^{+0.24}_{-0.24}$	$0.33^{+0.13}_{-0.12}$
SR0τa-bin07	$7.6^{+1.3}_{-1.3}$	$0.55^{+0.16}_{-0.14}$	$0.04^{+0.15}_{-0.15}$	$0.9^{+0.9}_{-0.9}$	$0.98^{+0.29}_{-0.30}$
SR0τa-bin08	$0.30^{+0.25}_{-0.24}$	$0.012^{+0.008}_{-0.007}$	$0.12^{+0.13}_{-0.13}$	$0.13^{+0.14}_{-0.14}$	$0.13^{+0.06}_{-0.06}$
SR0τa-bin09	$16.2^{+3.2}_{-3.1}$	$1.43^{+0.32}_{-0.28}$	$0.16^{+0.09}_{-0.12}$	$0.23^{+0.24}_{-0.23}$	$0.32^{+0.11}_{-0.11}$
SR0τa-bin10	$13.1^{+2.5}_{-2.6}$	$0.60^{+0.12}_{-0.13}$	$0.12^{+0.10}_{-0.10}$	$0.4^{+0.4}_{-0.4}$	$0.22^{+0.10}_{-0.11}$
SR0τa-bin11	19^{+4}_{-4}	$0.7^{+1.2}_{-1.2}$	$0.41^{+0.24}_{-0.22}$	$0.6^{+0.6}_{-0.6}$	$0.28^{+0.12}_{-0.12}$
SR0τa-bin12	$3.7^{+1.2}_{-1.2}$	$0.14^{+0.09}_{-0.09}$	$0.12^{+0.11}_{-0.11}$	$0.6^{+0.6}_{-0.6}$	$0.12^{+0.06}_{-0.06}$
SR0τa-bin13	613^{+65}_{-64}	29^{+4}_{-4}	$2.9^{+0.7}_{-0.6}$	$1.3^{+1.3}_{-1.3}$	$2.2^{+0.7}_{-0.7}$
SR0τa-bin14	207^{+33}_{-32}	$5.5^{+1.5}_{-1.5}$	$2.0^{+0.7}_{-0.6}$	$0.8^{+0.8}_{-0.8}$	$0.98^{+0.20}_{-0.20}$
SR0τa-bin15	58^{+12}_{-13}	$3.5^{+1.1}_{-1.0}$	$0.67^{+0.29}_{-0.28}$	$1.0^{+1.0}_{-1.0}$	$0.31^{+0.11}_{-0.11}$
SR0τa-bin16	$3.9^{+1.6}_{-1.4}$	$0.12^{+0.08}_{-0.07}$	$0.08^{+0.10}_{-0.10}$	$0.33^{+0.33}_{-0.33}$	$0.033^{+0.018}_{-0.018}$
SR0τa-bin17	50^{+7}_{-6}	$2.4^{+0.7}_{-0.6}$	$0.8^{+0.5}_{-0.5}$	$3.2^{+3.2}_{-3.2}$	$0.95^{+0.29}_{-0.29}$
SR0τa-bin18	$2.3^{+1.3}_{-1.3}$	$0.08^{+0.04}_{-0.04}$	$0.15^{+0.16}_{-0.16}$	$0.5^{+0.5}_{-0.5}$	$0.05^{+0.04}_{-0.04}$
SR0τa-bin19	$0.9^{+0.4}_{-0.4}$	$0.021^{+0.019}_{-0.019}$	$0.0023^{+0.0032}_{-0.0019}$	$0.08^{+0.08}_{-0.08}$	$0.007^{+0.006}_{-0.006}$
SR0τa-bin20	$0.12^{+0.11}_{-0.11}$	$0.009^{+0.009}_{-0.009}$	$0.012^{+0.016}_{-0.016}$	$0.07^{+0.08}_{-0.07}$	$0.0009^{+0.0004}_{-0.0004}$
SR0τb	$0.68^{+0.20}_{-0.20}$	$0.028^{+0.009}_{-0.009}$	$0.17^{+0.32}_{-0.32}$	$0.997^{+1.001}_{-1.001}$	$0.49^{+0.17}_{-0.17}$
SR1τ	$4.6^{+0.6}_{-0.6}$	$0.36^{+0.08}_{-0.08}$	$0.16^{+0.18}_{-0.18}$	$0.5^{+0.5}_{-0.5}$	$0.28^{+0.12}_{-0.12}$
SR2τa	$1.51^{+0.35}_{-0.33}$	$0.049^{+0.016}_{-0.014}$	$0.21^{+0.27}_{-0.29}$	$0.09^{+0.09}_{-0.09}$	$0.02052^{+0.00988}_{-0.00979}$
SR2τb	$2.09^{+0.30}_{-0.31}$	$0.135^{+0.025}_{-0.025}$	$0.023^{+0.015}_{-0.018}$	$0.031^{+0.033}_{-0.033}$	$0.08^{+0.04}_{-0.04}$

7.5.2 Reducible Background

For the analysis presented in this thesis, the processes that form the reducible background in the case of two real leptons are $t\bar{t}$, single top (Wt), WW, Z/γ^*, accompanied by a fake lepton, which originates from heavy flavour decay (HF), light flavour jet (LF), or a converted photon (CO). In the case of 1 real lepton, the main background comes from single top (s-channel, t-channel) processes, W accompanied by two fake leptons originating from HF decay, LF decay, or a conversion.

A data-driven technique is used to model the reducible background component. This data-driven technique is known as "matrix method" (MM) and exploits differences in object characteristics between real and fake leptons on a statistical basis. Leptons are first classified as "loose" (L) or "tight" (T) depending on isolation criteria and/or quality of the reconstruction. For this analysis, baseline leptons are considered loose leptons and signal leptons are considered tight leptons, as defined in Chapter 6.

The principle on which the method is based on is that the number of events with different proportions of the number of L and T leptons can be expressed as a linear combination of the number of events with real and fake leptons in a given region. In a three lepton final state, an 8×8 matrix is built to account for all possible combinations of real and fake leptons.

MC studies reported in Figure 7.15 show that the composition of the highest-p_{T} light lepton in signal regions SR0τb, SR1τ,SR2τa and SR0τb is real in the majority of the events, particularly for fake lepton background processes. By assuming that the highest p_{T} light lepton is always real, the dimension of the matrix is reduced from 8×8 to 4×4, which can be rewritten in terms of the remaining sub-leading leptons ($e/\mu/\tau$):

$$\begin{pmatrix} N_{TT} \\ N_{TL'} \\ N_{L'T} \\ N_{L'L'} \end{pmatrix} = \begin{pmatrix} \epsilon_1\epsilon_2 & \epsilon_1 f_2 & f_1\epsilon_2 & f_1 f_2 \\ \epsilon_1(1-\epsilon_2) & \epsilon_1(1-f_2) & f_1(1-\epsilon_2) & f_1(1-f_2) \\ (1-\epsilon_1)\epsilon_2 & (1-\epsilon_1)f_2 & (1-f_1)\epsilon_2 & (1-f_1)f_2 \\ (1-\epsilon_1)(1-\epsilon_2) & (1-\epsilon_1)(1-f_2) & (1-f_1)(1-\epsilon_2) & (1-f_1)(1-f_2) \end{pmatrix} \cdot \begin{pmatrix} N_{RR} \\ N_{RF} \\ N_{FR} \\ N_{FF} \end{pmatrix}, \quad (7.9)$$

where:

- ϵ is the probability that a real-loose lepton is identified as a tight lepton, referred to as "real efficiencies";
- f is the probability that a fake-loose lepton is mis-identified as a tight lepton, referred to as "fake rates" or "fake efficiencies";

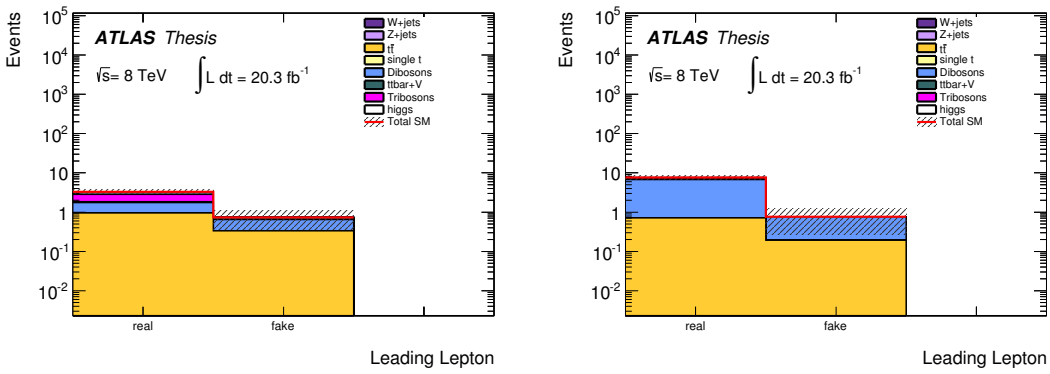

(a) SR0τb: e/μ (b) SR1τ: e/μ

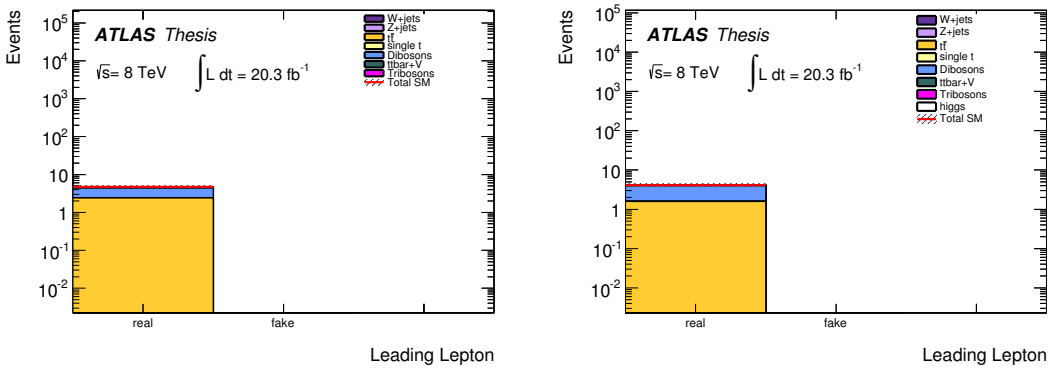

(c) SR2τa: e/μ (d) SR2τb: e/μ

Figure 7.15: The purity of the leading light lepton in SR0τb, SR1τ, SR2τa and SR2τb using MC events.

- N_{RR} is the number of events with two real leptons, $N_{RF} + N_{FR}$ is the number of events with one real and one fake lepton, and N_{FF} is the number of events with two fake leptons;

- N_{TT} , $N_{TL'}$, $N_{L'T}$ and $N_{L'L'}$, denote the number of events with two leptons with the first (second) index corresponds to the higher (lower) p_{T} lepton. Given that the leading light lepton is always a true one, the MM only considers the other two leptons ($e/\mu/\tau$). L' indicates loose leptons that fail the tight requirement.

In order to obtain the real composition (N_{RR}) and fake composition (N_{FF}) of loose leptons, the matrix must be inverted. This can be obtained if the efficiencies (ϵ and f) are known.

The total number of events with fake-loose leptons[1] is then given by

[1] N_{RR} does not contribute to the fake lepton estimate.

$$
\begin{aligned}
N_{Fake} &= N_{RF} \ + \ N_{FR} \ + \ N_{FF} \\
&= \frac{1}{(\epsilon_1 - f_1)(\epsilon_2 - f_2)}[\ (\epsilon_1\epsilon_2 - \epsilon_1 f_2 - f_1\epsilon_2 + f_1 + f_2 - 1)N_{TT} \\
&+ \ (\epsilon_1\epsilon_2 - \epsilon_1 f_2 - f_1\epsilon_2 + f_2)N_{TL} \ + \ (\epsilon_1\epsilon_2 - \epsilon_1 f_2 - f_1\epsilon_2 + f_1)N_{LT} \\
&\qquad + \ (\epsilon_1\epsilon_2 - \epsilon_1 f_2 - f_1\epsilon_2)N_{LL} \ ].
\end{aligned}
\tag{7.10}
$$

Since the analysis uses signal selection leptons (tight leptons), an extra step to extrapolate $LL \to TT$ is needed to estimate the fake-tight leptons selection:

$$
\begin{aligned}
N_{Fake}^{LL\to TT} &= N_{RF}^{LL\to TT} + N_{FR}^{LL\to TT} + N_{FF}^{LL\to TT} \\
&= \epsilon_1 f_2 \times N_{RF} + f_1\epsilon_2 \times N_{FR} + f_1 f_2 \times N_{FF}
\end{aligned}
\tag{7.11}
$$

with

$$
\begin{aligned}
N_{RR}^{LL\to TT} &= \epsilon_1\epsilon_2 \times N_{RR} \\
N_{RF}^{LL\to TT} &= \epsilon_1 f_2 \times N_{RF} \\
N_{FR}^{LL\to TT} &= f_1\epsilon_2 \times N_{FR} \\
N_{FF}^{LL\to TT} &= f_1 f_2 \times N_{FF}.
\end{aligned}
\tag{7.12}
$$

The real lepton efficiencies and fake rates are measured in each SR and VR using MC and corrected to those measured in data using "scale factors". These are measured for each lepton flavour as detailed below.

Real Lepton Efficiencies

The efficiency for real-loose leptons to satisfy the tight lepton requirements is measured on MC-simulated data using a tag-and-probe method on $Z \to \ell\ell$ events with two loose light leptons (e/μ) forming a SFOS pair with $|m_{\text{SFOS}} - m_Z| < 10$ GeV. The "tag" light lepton is required to satisfy the tight identification requirements and must be matched to the relevant single-lepton trigger chain. The efficiency calculation is tested on the other light lepton (the "probe"). Both light leptons are be considered as tags if they pass the tight requirements. The real efficiencies are then corrected via scale factors, which are assumed to be independent of the process, to account for potential differences with respect to the data. These scale factors are taken as the ratio of the efficiency measured in data over the efficiency measured in MC.

The real lepton efficiency scale factors for electrons and muons are found to be 0.998 ± 0.013 and 0.996 ± 0.001 respectively, where the uncertainties are statistical [1]. The real tau efficiency scale factor is assumed to be 1.0.

Fake Lepton Efficiencies

The fake lepton efficiencies for loose leptons ($\ell = e/\mu/\tau$) in a given region will depend on: the type of the fake candidate (heavy flavour, light flavour, conversion); and the process it originates from (top, Z+jets, $V+\gamma$, and diboson). These different behaviours will lead to different fake estimates in SRs and VRs. To accounts for potential differences arising from these behaviours and also for differences between data and simulation, scale factors are introduced for each measured fake rate. The total estimate will be a weighted average of the measured fake rates with the scale factors acting as weights, as in Equation 7.13,

$$f_{SR/VR} = \Sigma_{i,j}(sf^{i} \times R^{ij}_{SR/VR} \times f^{ij}), \tag{7.13}$$

where:

- the indices i indicate the fake type (LF, HF, CO) and j the process category the fake originates from (top, Z+jets, $V+\gamma$, and diboson);
- sf^{i} is the *scale factor* dependent only on the fake type.
- $R^{ij}_{SR/VR}$ are the *fake fractions* measured as the ratio of fake leptons of type i originating from the process category j with respect to the total number of all fake leptons from all processes, in a SR or VR. .
- f^{ij} is the *fake rate* measured as the ratio between tight leptons and loose leptons of a given type i and a originating process j.

The fake rates (f^{ij}) for each relevant fake lepton type (HF, LF or CO) and for each reducible background process are obtained using MC-simulated events with a three lepton selection, where the leading light lepton is assumed real and the other two leptons enter the calculation. These fake rates are parametrised with the lepton p_{T} and η and are then corrected using the scale factors described below.

Heavy Flavour scale factors: sf^{HF} are measured as the ratio of the fake rate of HF candidates in data over the fake rate in MC simulation.

The electron and muon HF fake rate scale factor is calculated using a tag-and-probe method. In this case, the $b\bar{b}$ and $c\bar{c}$ production are chosen as the source of leptons from heavy flavour decay. Selected events must pass standard quality criteria and contain one tag muon within $\Delta R < 0.4$ from a b-tagged jet that fired the single-muon trigger and one loose probe lepton (e/μ). To suppress background, events

are rejected if there is more than one b-jet in the event. The missing transverse momentum for each event must be ≤ 60 GeV, and the transverse mass of the probe lepton is ≤ 50 GeV. In data, any remaining background ($\sim 1\%$) due to non heavy flavour leptons is subtracted using the predictions from MC (these predictions include all relevant processes normalised to the luminosity in the data). The fake rate is then measured as the probability that the probe lepton passes the tight requirements.

The heavy-flavour scale factors found are: $sf_e^{\mathrm{HF}} = 0.74 \pm 0.04$, $sf_\mu^{\mathrm{HF}} = 0.89 \pm 0.03$, where the uncertainties are statistical [1]. Studies done in the trilepton analysis group showed that HF tau fakes are negligible in three lepton regions, therefore this value is taken to be $sf_\tau^{\mathrm{HF}} = 1.0$ with a 10% uncertainty, which is conservative with respect to the other measured HF scale factors.

Light Flavour scale factors. Studies done in the trilepton analysis group showed that LF electron and muon fakes are negligible in three lepton events[103] and so the LF scale factors are taken as $sf_{e/\mu}^{\mathrm{LF}} = 1.0$ with a conservative uncertainty of 10%. The light flavour fake rate for taus is measured in a W+jets enriched region that is rich in taus faked by quark jets. The same LF scale factor is applied also to fake rates of taus from gluon jets. Taus faked by quark jets are seen to be the dominating source of light flavour faked taus (by roughly a factor of 10) due to the larger fake rate compared to those faked by gluon jets.

Selected events must contain one tight muon and an additional loose tau to derive the LF tau fake rate. The muon is required to have fired the single isolated muon trigger with $p_{\mathrm{T}} > 25$ GeV. Significant background suppression of the $Z \to \tau\tau$ decays is obtained by requiring the transverse mass $m_T(\mu, E_T^{miss}) > 60$ GeV and $\sum \cos(\Delta\phi)$ $= \cos(\Delta\phi(E_{\mathrm{T}}^{\mathrm{miss}}, \mu)) + \cos(\Delta\phi(E_{\mathrm{T}}^{\mathrm{miss}}, \tau)) \leq$ -0.15. In addition, a b-jet veto is applied to separate the light and heavy flavour fake rates. The remaining background is subtracted using a MC based estimate (method explained in the HF section).

The LF tau scale factors are separated into 1- and 3-prong taus due to observed differences in the fake rates and scale factors. These scale factors decrease from 0.9 to 0.6 (1.0 to 0.6) for 1-prong (3-prong) taus as the p_{T} increases from 20 GeV to 150 GeV, therefore a p_T dependent scale factor is applied to correct the MC based fake rates [1].

Conversions scale factors. The electron conversion fake rate is the probability that a loose electron originating from a photon conversion passes the tight identification

requirements. The conversion scale factors are determined in events with a converted photon radiated from a muon in $Z \to \mu\mu$ decays. Events passing the quality and trigger requirements are requested to contain a pair of OS tight muons and one loose electron (tag) such that the tri-lepton invariant mass, $m_{\mu\mu e}$, is compatible with the Z boson hypothesis ($81.2 < m_{\mu\mu e} < 101.2\,\text{GeV}$). A constraint on $m_{\mu\mu e}$ helps suppress contributions from jets in $Z/\gamma^* + jets$ processes. Additional fake contributions from dibosons and $t\bar{t}$ samples are subtracted from the data during the calculation of the fake rate (following the same procedure described in the HF section).

The conversion scale factor for electrons is $sf_e^{\text{CO}} = 1.14 \pm 0.12$. The background from muons coming from electron conversion is considered to be negligible.

7.5.3 Validation of Background Estimation Method

To validate the background modelling, the MC estimates for irreducible backgrounds and the data-driven estimates for the reducible backgrounds estimated in VRs are compared to the observed data.

The definition of the VRs used in this analysis are shown in Table 7.5 with the respective SM background(s) that each of them is sensitive to.

Table 7.5: Summary of the selection requirements for the validation regions.

Region name	N(ℓ)	N(τ)	Flavour/sign	Z boson	$E_{\text{T}}^{\text{miss}}$ [GeV]	N(b-jets)	Target process
VR0τnoZa	3	0	$\ell^+\ell^-\ell$, $\ell^+\ell^-\ell'$	m_{SFOS} & 3$ell Z veto	35–50	–	WZ^*, Z^*Z^*
		0					Z^*+jets
VR0τZa	3	0	$\ell^+\ell^-\ell$, $\ell^+\ell^-\ell'$	request	35–50	–	WZ, Z+jets
VR0τnoZb	3	0	$\ell^+\ell^-\ell$, $\ell^+\ell^-\ell'$	m_{SFOS} & $m_{3\ell}$ veto	> 50	1	$t\bar{t}$
VR0τZb	3	0	$\ell^+\ell^-\ell$, $\ell^+\ell^-\ell'$	request	> 50	1	WZ
VR0τb	3	0	$\ell^+\ell^-\ell$, $\ell^+\ell^-\ell'$	binned	binned	1	WZ, $t\bar{t}$
VR1τa	2	1	$\tau^\pm\ell^\mp\ell^\mp$, $\tau^\pm\ell^\mp\ell'^\mp$	–	35–50	–	WZ, Z+jets
VR1τb	2	1	$\tau^\pm\ell^\mp\ell^\mp$, $\tau^\pm\ell^\mp\ell'^\mp$	–	> 50	1	$t\bar{t}$
VR2τa	1	2	$\tau\tau\ell$	–	35–50	–	W+jets, Z+jets
VR2τb	1	2	$\tau\tau\ell$	–	> 50	1	$t\bar{t}$

Similarly to the tri-lepton SRs, VRs are distinguished in terms of tau multiplicity final states ($\ell\ell\ell$, $\ell\ell\tau$ and $\ell\tau\tau$ VRs). For each considered τ multiplicity, validation regions are defined with either low-$E_{\text{T}}^{\text{miss}}$ ("a" regions) or high-$E_{\text{T}}^{\text{miss}}$ + b-tagged jet ("b" regions) to target different background processes. To validate the background model in the light lepton SRs (SR0τa/b), two different VRs are defined: a low-$E_{\text{T}}^{\text{miss}}$ validation regions are defined so that the dominant backgrounds, WZ and/or Z processes, are enhanced; and a binned high-$E_{\text{T}}^{\text{miss}}$ + b-jet validation region so that $t\bar{t}$ is enhanced. Additionally, VRs with a Z-veto and a Z-request are also defined in the regions "a" and "b". In the Z-veto

region, Z candidates are vetoed using an invariant mass window on the invariant mass of the SFOS pair, thus reducing the $Z \to \ell\ell\ell$ contribution from Z+jets processes (where the third lepton is a converted photon from final state radiation). Even though Z+jets contribute very little to the total background estimate in light lepton SRs (due to high $E_{\mathrm{T}}^{\mathrm{miss}}$ requirements), by vetoing them in the VRs a better modelling of more relevant backgrounds is achieved.

An orthogonal validation region (VR0τb) to the light lepton binned signal region SR0τa is defined, by having the same binning as in Table 7.3 with the addition of a b-jet request.

Similarly, for tau-rich SRs, the VRs are split into low-$E_{\mathrm{T}}^{\mathrm{miss}}$ and high-$E_{\mathrm{T}}^{\mathrm{miss}}$ + b-jet selections. A same charge requirement of the light lepton pair in 1-τ VR regions is required to remain close to SR1τ.

The agreement between the background expectation and the data within statistical and systematic uncertainties (described in the Section 7.6) can be seen in Table 7.6, in which the reducible background is estimated with the MM and the irreducible is estimated from MC. This indicates that the reducible background is well described by the matrix method. The number of expected and observed events for all bins defined in VR0τb can be seen in Figure 7.16.

Table 7.6: Expected numbers of SM background events in selected validation regions, as defined in table 7.5. The binned validation region VR0τb is displayed in Figure 7.16. Statistical and systematic uncertainties are included (as described in section 7.6).

Sample	VR0τnoZa	VR0τZa	VR0τnoZb	VR0τZb	VR1τa	VR1τb	VR2τa	VR2τb
WZ	91 ± 12	471 ± 47	$10.5^{+1.8}_{-2.0}$	58 ± 7	14.6 ± 1.9	1.99 ± 0.35	$14.3^{+2.4}_{-2.5}$	1.9 ± 0.4
ZZ	19 ± 4	48 ± 7	0.62 ± 0.12	2.6 ± 0.4	$1.76^{+0.29}_{-0.28}$	0.138 ± 0.028	1.8 ± 0.4	0.12 ± 0.04
$t\bar{t}V + tZ$	3.2 ± 1.0	$10.1^{+2.3}_{-2.2}$	9.5 ± 3.1	18 ± 4	0.9 ± 0.9	2.8 ± 1.3	1.0 ± 0.7	1.7 ± 0.7
VVV	1.9 ± 1.9	0.7 ± 0.7	$0.35^{+0.36}_{-0.35}$	0.18 ± 0.18	0.4 ± 0.4	0.08 ± 0.08	0.12 ± 0.12	$0.06^{+0.07}_{-0.06}$
Higgs	2.7 ± 1.3	2.7 ± 1.5	1.5 ± 1.0	0.71 ± 0.29	0.57 ± 0.34	0.5 ± 0.5	0.6 ± 0.4	0.5 ± 0.5
Reducible	73^{+20}_{-17}	261 ± 70	47^{+15}_{-13}	19 ± 5	71 ± 9	22.7 ± 2.8	630^{+9}_{-12}	162^{+6}_{-8}
Total SM	191^{+24}_{-22}	794 ± 86	69^{+15}_{-14}	98 ± 10	89^{+10}_{-9}	28.2 ± 3.2	648^{+10}_{-13}	166^{+6}_{-8}
Data	228	792	79	110	82	26	656	158

Also, the agreement between the MC-only background expectation and the data within statistical and systematic uncertainties (described in the Section 7.6) can be seen in Table 7.7. This indicates that the SM background is moderately well described by the MC. The MC-only expectation in the "b" regions is seen to agree well with the observed data. However, in the "a" regions, the MC-only expectation is slightly lower than the observed

data in three out of four regions, due to small MC statistics in the reducible background processes.

Table 7.7: Expected numbers of SM background events using MC based estimates in selected validation regions, as defined in table 7.5. Statistical and systematic uncertainties are included (as described in section 7.6).

Sample	VR0τnoZa	VR0τZa	VR0τnoZb	VR0τZb	VR1τa	VR1τb	VR2τa	VR2τb
WZ	91^{+12}_{-12}	471^{+47}_{-47}	$10.5^{+1.8}_{-2.0}$	58^{+7}_{-7}	$14.6^{+1.9}_{-1.9}$	$1.99^{+0.35}_{-0.35}$	$14.3^{+2.4}_{-2.5}$	$1.9^{+0.4}_{-0.4}$
ZZ	19^{+4}_{-4}	48^{+7}_{-7}	$0.62^{+0.12}_{-0.12}$	$2.6^{+0.4}_{-0.4}$	$1.76^{+0.29}_{-0.28}$	$0.138^{+0.028}_{-0.028}$	$1.8^{+0.4}_{-0.4}$	$0.12^{+0.04}_{-0.04}$
$Top + V$	$3.211^{+1.010}_{-0.970}$	$10.1^{+2.3}_{-2.2}$	$9.5^{+3.1}_{-3.1}$	18^{+4}_{-4}	$0.9^{+0.9}_{-0.9}$	$2.8^{+1.3}_{-1.3}$	$1.0^{+0.7}_{-0.7}$	$1.7^{+0.7}_{-0.7}$
VVV	$1.9^{+1.9}_{-1.9}$	$0.7^{+0.7}_{-0.7}$	$0.35^{+0.36}_{-0.36}$	$0.18^{+0.18}_{-0.18}$	$0.4^{+0.4}_{-0.4}$	$0.08^{+0.08}_{-0.08}$	$0.12^{+0.12}_{-0.12}$	$0.06^{+0.07}_{-0.07}$
Higgs	$2.7^{+1.3}_{-1.3}$	$2.7^{+1.5}_{-1.5}$	$1.5^{+1.0}_{-1.0}$	$0.71^{+0.29}_{-0.29}$	$0.57^{+0.34}_{-0.34}$	$0.5^{+0.5}_{-0.5}$	$0.6^{+0.4}_{-0.4}$	$0.5^{+0.5}_{-0.5}$
Z+jets	36^{+21}_{-20}	143^{+54}_{-46}	$0.0^{+0.0}_{-0.0}$	6^{+6}_{-6}	28^{+17}_{-14}	$1.1^{+1.4}_{-1.4}$	212^{+61}_{-54}	$0.5^{+0.6}_{-0.4}$
WW	$0.45^{+0.19}_{-0.16}$	$0.14^{+0.10}_{-0.10}$	$0.04^{+0.04}_{-0.04}$	$0.0^{+0.0}_{-0.0}$	$0.14^{+0.12}_{-0.12}$	$0.0^{+0.0}_{-0.0}$	$3.7^{+0.5}_{-0.6}$	$0.54^{+0.17}_{-0.19}$
$V + \gamma$	$20.2^{+3.3}_{-4.1}$	31^{+5}_{-5}	$0.26^{+0.33}_{-0.47}$	$0.9^{+0.7}_{-0.6}$	6^{+4}_{-4}	$0.5^{+0.5}_{-0.6}$	15^{+6}_{-6}	$0.0^{+0.0}_{-0.0}$
$t\bar{t}$	22^{+5}_{-4}	$4.7^{+1.9}_{-1.4}$	53^{+7}_{-7}	$13.9^{+2.3}_{-2.3}$	$9.8^{+3.0}_{-2.8}$	$16.00^{+2.50}_{-2.50}$	78^{+9}_{-10}	112^{+9}_{-10}
t	$2.5^{+1.4}_{-1.4}$	$0.7^{+1.4}_{-0.7}$	$1.5^{+0.9}_{-1.0}$	$1.1^{+1.3}_{-1.3}$	$1.0^{+0.7}_{-0.7}$	$1.3^{+0.8}_{-0.8}$	11^{+7}_{-6}	$13.6^{+3.1}_{-3.3}$
Σ SM	198^{+32}_{-30}	713^{+86}_{-79}	78^{+10}_{-9}	101^{+11}_{-11}	68^{+18}_{-15}	$24.3^{+3.5}_{-3.6}$	654^{+165}_{-154}	146^{+16}_{-15}
Data	228	792	79	110	82	26	656	158

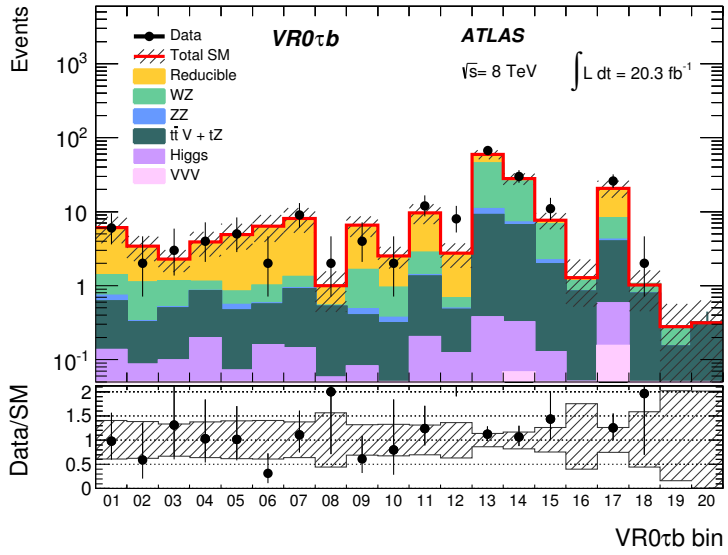

Figure 7.16: Number of expected and observed events in the validation region VR0τb [1]. Also shown are the respective contributions of the various background processes as described in the legend. The uncertainty band includes both the statistical and systematic uncertainties on the SM prediction.

The following paragraphs show the most interesting kinematic distributions relevant to each validation region (except for the binned VR, VR0τb).

$3\ell + 0\tau$ channel

A few kinematic distributions in validation regions with three light leptons (VR0τnoZa, VR0τZa, VR0τnoZb and VR0τZb) are shown in Figures 7.17-7.20. Table 7.6 shows the yields in these regions (using the MM estimates for the reducible background), where good agreement is seen between data and the expected SM background. The shapes of these kinematic variables are seen to agree well with data in VR0τnoZa, VR0τZa, VR0τnoZb and VR0τZb.

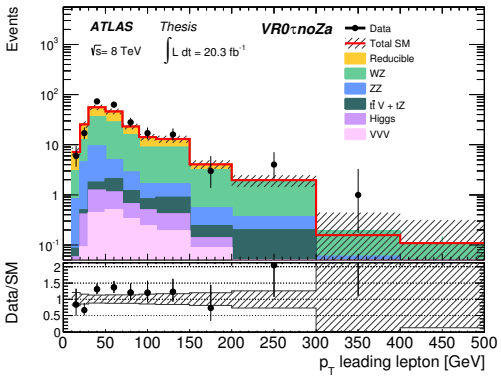

(a)

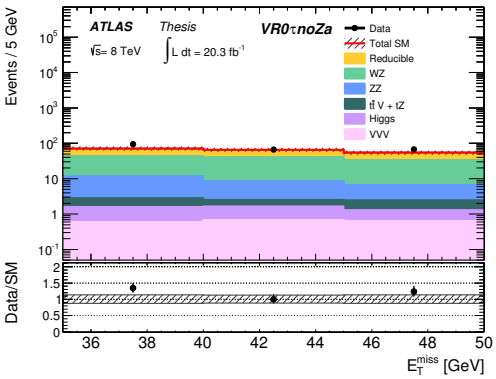

(b)

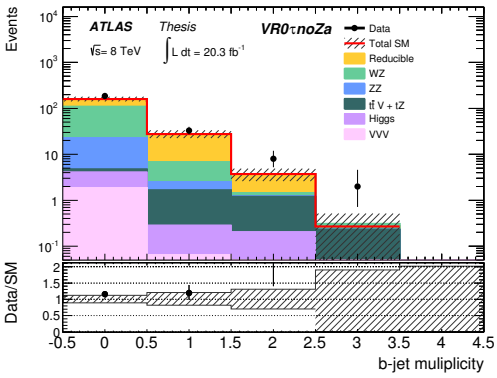

(c)

Figure 7.17: Distributions in VR0τnoZa. The uncertainties are statistical and systematic (as described in section 7.6). The last bin in each distribution includes the overflow.

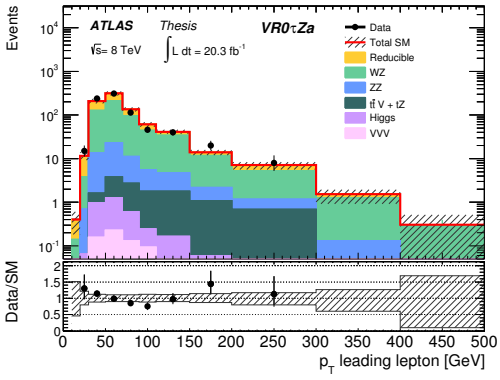

(a)

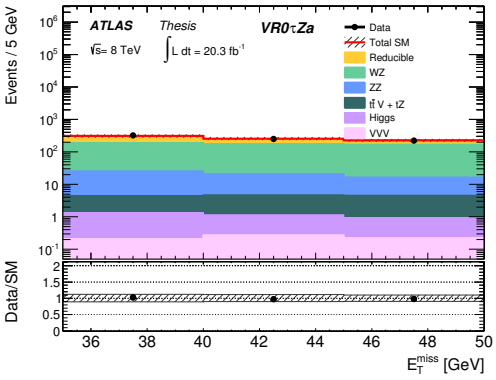

(b)

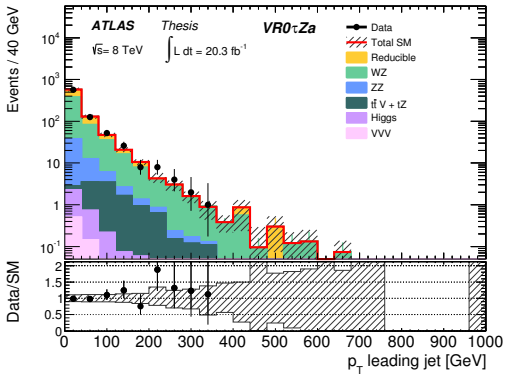

(c)

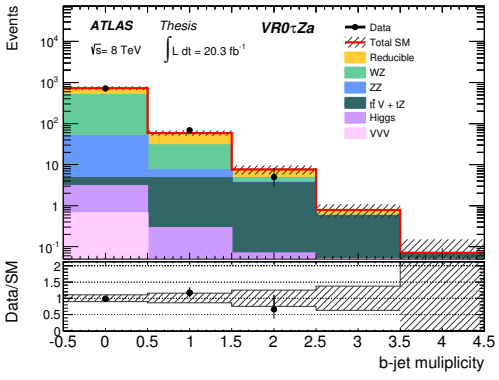

(d)

Figure 7.18: Distributions in VR0τZa. The uncertainties are statistical and systematic (as described in section 7.6). The last bin in each distribution includes the overflow.

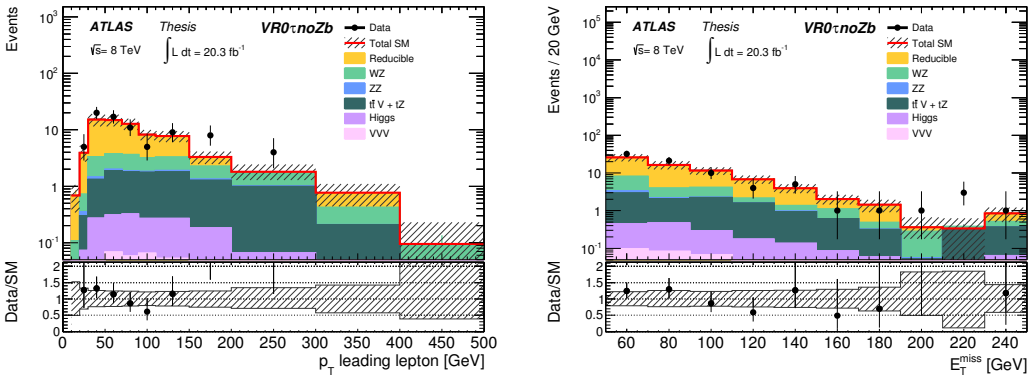

(a) (b)

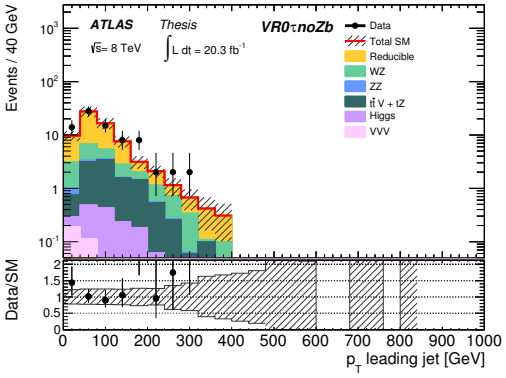

(c)

Figure 7.19: Distributions in VR0τnoZb. The uncertainties are statistical and systematic (as described in section 7.6). The last bin in each distribution includes the overflow.

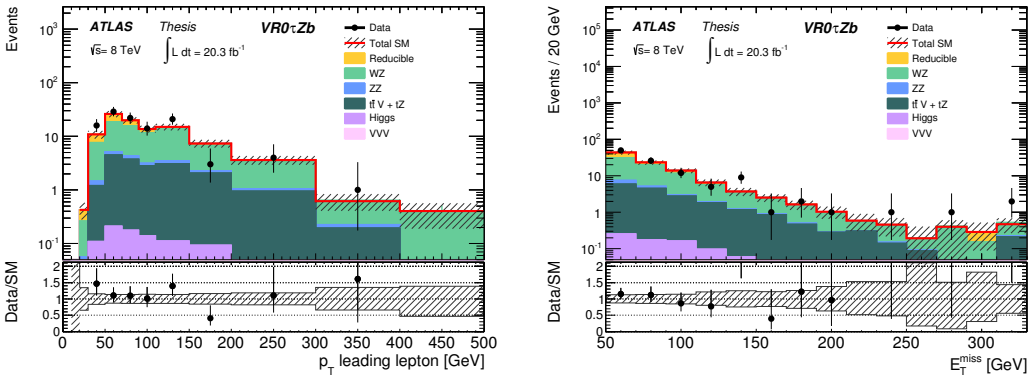

(a)

(b)

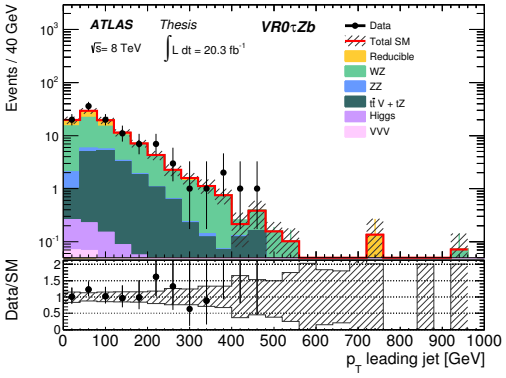

(c)

Figure 7.20: Distributions in VR0τZb. The uncertainties are statistical and systematic (as described in section 7.6). The last bin in each distribution includes the overflow.

$2\ell + 1\tau$ channel

The yields (using the MM estimates for the reducible background) in VRs with two light leptons and one hadronic tau (VR1τa and VR1τb) show excellent agreement between the expected background and observed events (see Table 7.6). The ability to correctly model kinematic variables used to define SR1τ is also tested. The shapes of the expected $m_{\ell\tau}$, $E_{\mathrm{T}}^{\mathrm{miss}}$, $\sum p_{\mathrm{T}}(e/\mu)$ distributions shown in Figure 7.21-7.22 are seen to agree well with data in VR1τa and VR1τb.

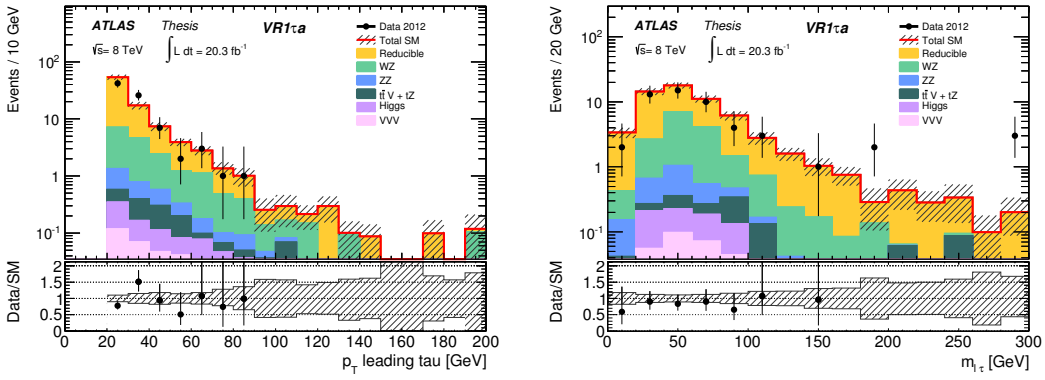

(a) (b)

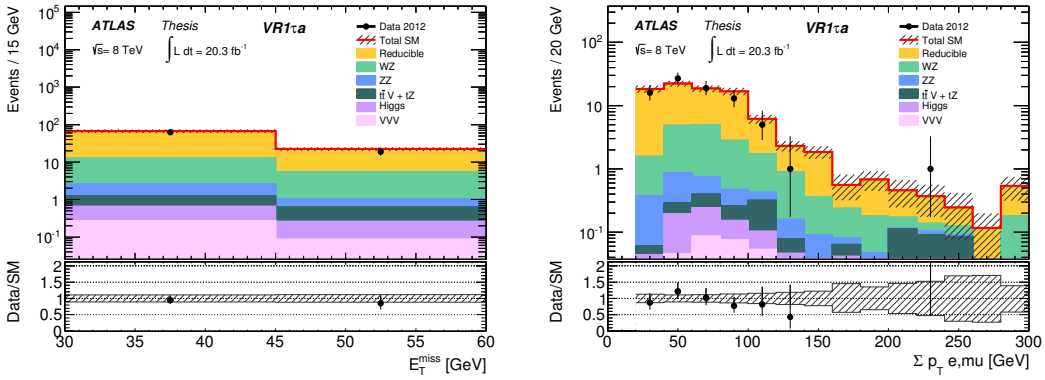

(c) (d)

Figure 7.21: Distributions in VR1τa. The uncertainties are statistical and systematic (as described in section 7.6). The last bin in each distribution includes the overflow. The data excess shown in the overflow bin in Figure 7.21(b) is above 1 TeV.

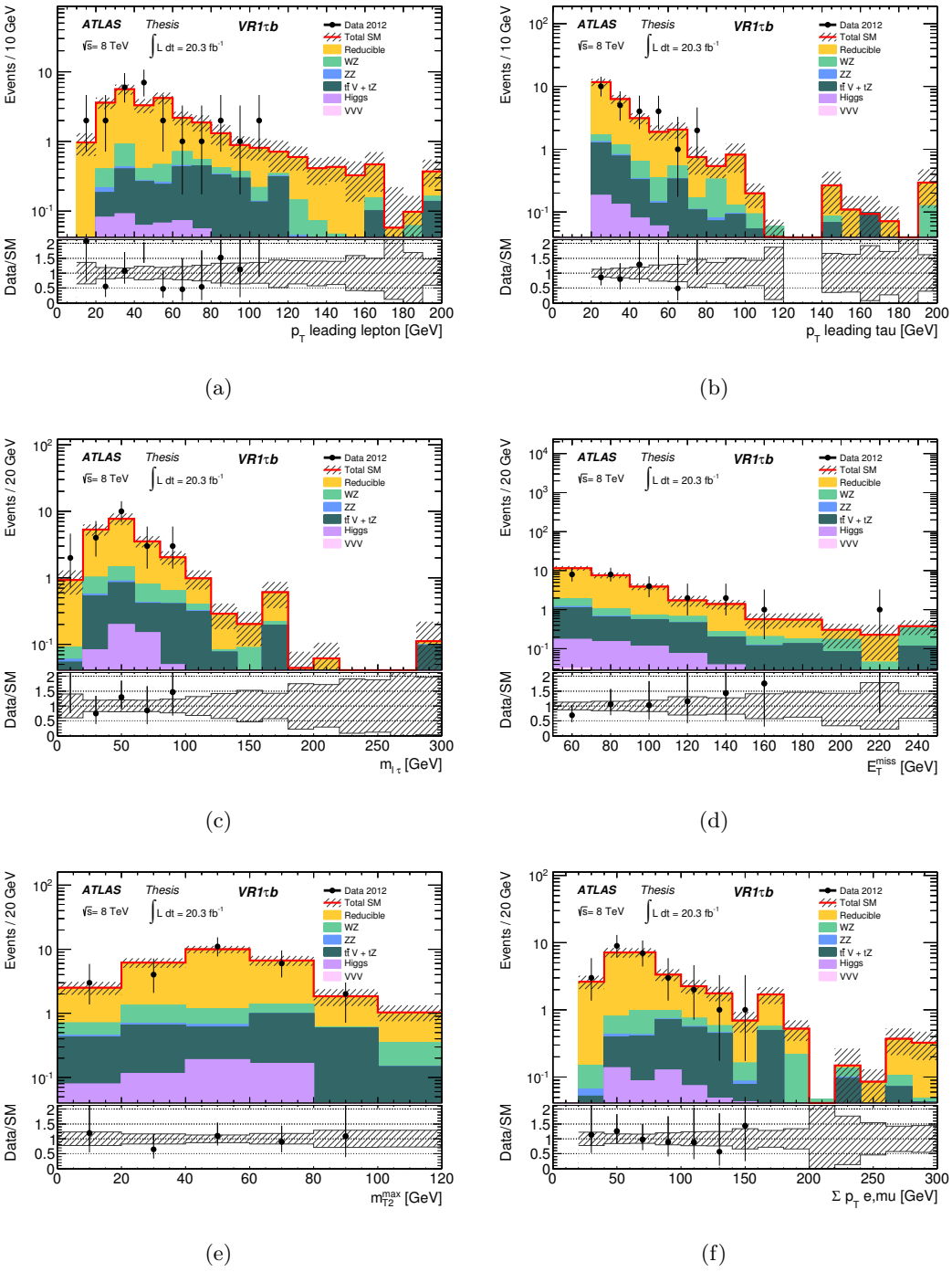

Figure 7.22: Distributions in VR1τb. The uncertainties are statistical and systematic (as described in section 7.6). The last bin in each distribution includes the overflow.

$1\ell + 2\tau$ channel

In VRs with two hadronic taus and one light lepton (VR2τa and VR2τb), the shapes of the expected $m_{\tau\tau}$, $E_{\mathrm{T}}^{\mathrm{miss}}$, $m_{\mathrm{T2}}^{\mathrm{max}}$, and p_{T} of the taus are seen to agree well with data, as shown in Figures 7.23-7.24. Table 7.6 shows the very good agreement between data and expected MC background in these two VRs.

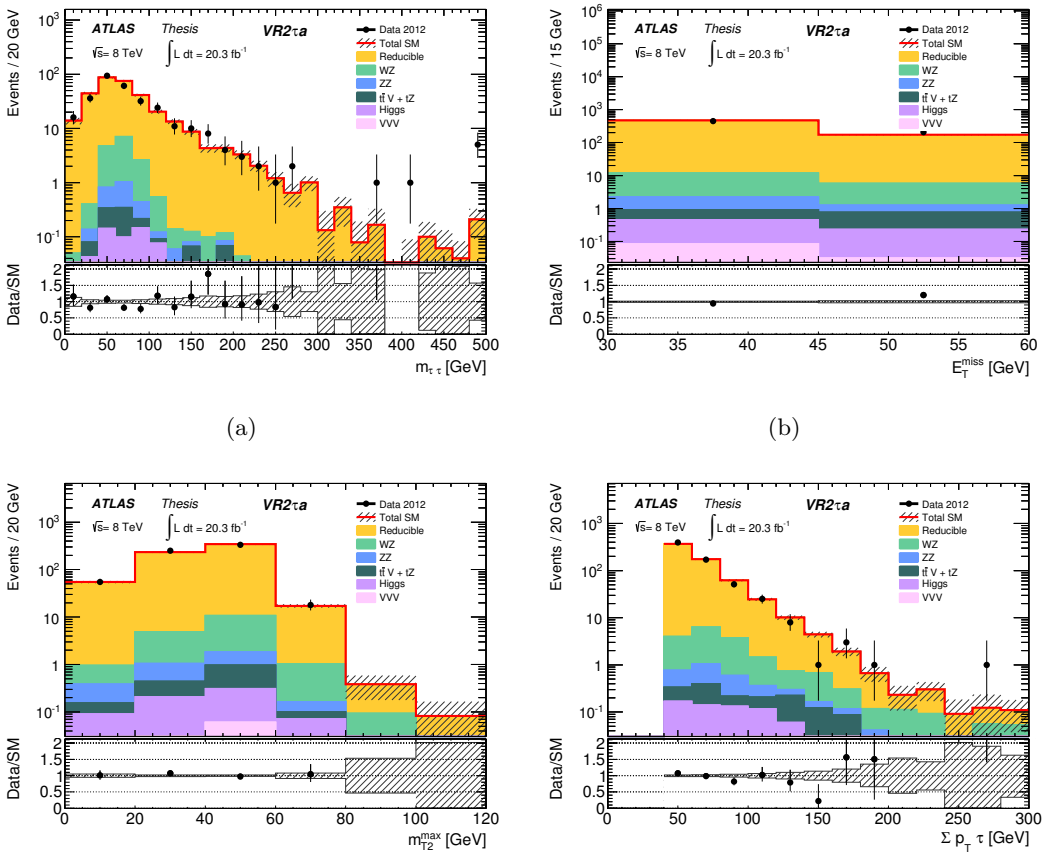

(a) (b)

(c) (d)

Figure 7.23: Distributions in VR2τa. The uncertainties are statistical and systematic (as described in section 7.6). The last bin in each distribution includes the overflow. The data excess shown in the overflow bin in Figure 7.23(a) is above 1 TeV.

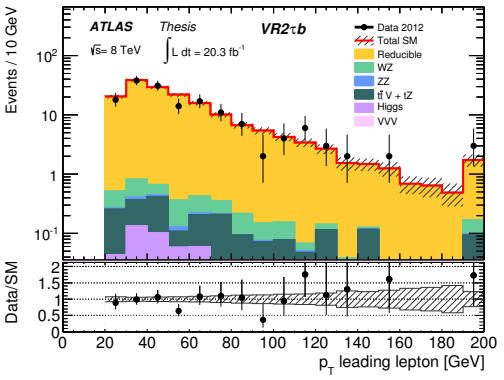

(a)

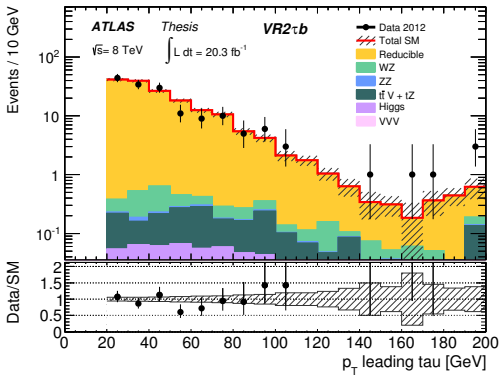

(b)

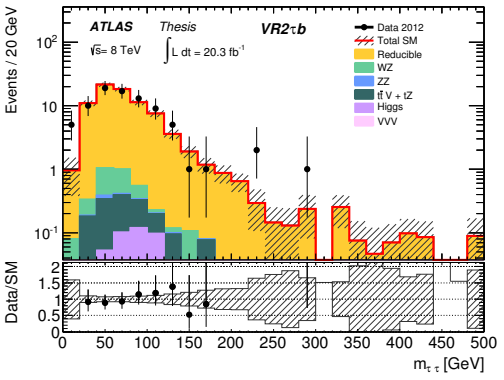

(c)

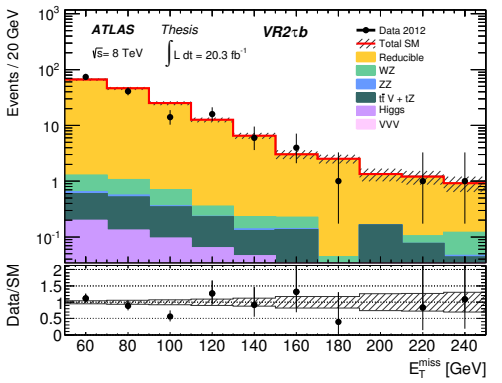

(d)

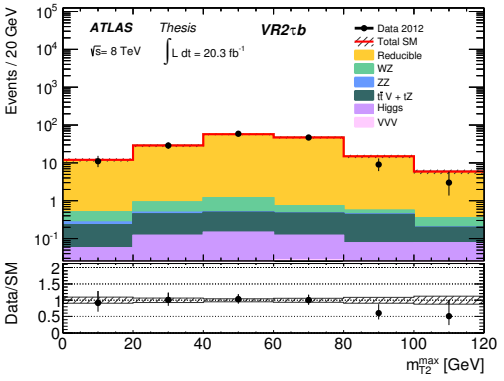

(e)

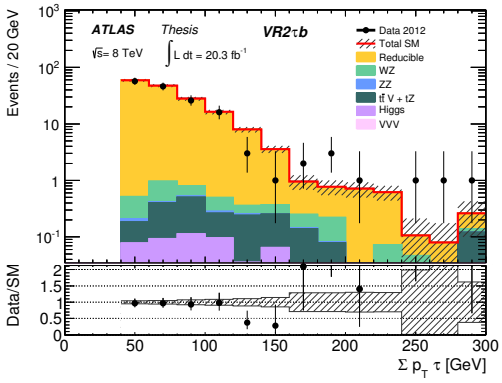

(f)

Figure 7.24: Distributions in VR2τb. The uncertainties are statistical and systematic (as described in section 7.6). The last bin in each distribution includes the overflow.

7.6 Systematic Uncertainties

A summary of the dominant sources of systematic uncertainties in the background and signal estimates for each SR are listed in Table 7.8, where the component due to the limited number of simulated events (also referred to as statistics) available in the MC-simulated data is separated into both the reducible and irreducible background parts. In SR0τa, the leading systematic uncertainties are due to theoretical uncertainties on the cross sections of the irreducible backgrounds, the choice of MC generator for the diboson and $t\bar{t}V$ processes, and the statistical uncertainty on the irreducible and reducible background estimates. In SR0τb, the theoretical cross section uncertainties on the irreducible backgrounds dominates the overall uncertainty. In SR1τ, the total uncertainty is mainly dominated by uncertainties on the reducible background and the theoretical cross section uncertainty on on the irreducible backgrounds. In the two tau signal regions SR2τa and SR2τb, the total uncertainty is mainly dominated by the systematics that arise from the fake background estimation, particularly from the tau fake rate measurements described in Section 7.5.2 and the statistical uncertainties.

Table 7.8: Summary of the dominant systematic uncertainties in the background estimates for each SR defined in Section 7.4. Uncertainties are quoted relative to the total expected background. For the 20 bins of the SR0τa the range of the uncertainties is provided.

	SR0τa	SR0τb	SR1τ	SR2τa	SR2τb
Cross section	4–25%	37%	9%	3.1%	3.0%
Generator	3.2–35%	11%	3.1%	6%	$< 1\%$
Statistics on irreducible background	0.8–26%	8%	5%	5%	3.1%
Statistics on reducible background	0.4–29%	14%	8%	13%	12%
Electron mis-identification probability	0.3–10%	1.3%	$< 1\%$	–	–
Muon mis-identification probability	0.1–24%	2.2%	$< 1\%$	–	–
τ mis-identification probability	–	–	8%	4%	5%

7.6.1 Uncertainties on the Irreducible Background

Theoretical uncertainties affecting the simulation-based background estimates used for the analysis presented in this thesis are detailed in the following.

MC Cross Section. Theoretical cross section uncertainties on the irreducible background processes due to the choice of re-normalisation, factorisation scales and PDFs are summarised below:

- a 30% systematic on the production cross section of $t\bar{t} + Z(/W/WW)$ at NLO is applied based on the resulted in ref. [89, 90];
- 5% for ZZ and 7% for WZ production cross section has been applied based on the predictions in ref. [113];
- 100% uncertainty is assumed as a conservative approach for triboson processes since there are no measurements yet;

The Higgs boson production cross sections are calculated with varying precision in the perturbative expansion. For total cross sections, the calculations are performed up to the NNLO QCD correction (and NLO electroweak corrections) for the following production modes: $gg \to H$, $qq' \to qq'H$ and $q\bar{q} \to WH/ZH$ processes, while up to NLO for $q\bar{q}/gg \to t\bar{t}H$ process.

- 20% uncertainty is used for VH and VBF production, while a 100% uncertainty is assigned to $t\bar{t}H$ and ggF production, based on studies detailed in Ref. [97]. The uncertainty for $t\bar{t}H$ and ggF production are assumed to be large to account for uncertainties on the acceptance, while the inclusive cross-sections are known to better precision.

MC Generator Systematic uncertainties arising from the choice of MC generator used to simulate the irreducible SM processes are estimated by comparing the acceptance in the SR between two different MC generators. For WZ, ZZ diboson processes, the comparison is done between Powheg (main generator) and aMC@NLO samples. For the $t\bar{t} + Z/W$ background processes, events generated using MadGraph (main generator) are compared to those simulated in Alpgen. The generator systematic uncertainties found to be in a range from 3-35% in regions without a hadronic tau requirement in the final state, whereas the regions which do have this requirement have a systematic uncertainty of around 1-6%.

PDF The acceptance uncertainty due to PDFs was also estimated for the diboson irreducible background.

These PDF uncertainties are estimated using 90% confidence level CT10 PDF eigenvectors [114]. The CT10 PDF set is based on 26 free parameters and the resulting 90% confidence level upper and lower variations in these parameters form the "error set" for the PDF. The asymmetric positive and negative uncertainties of the PDFs (f_a) are computed as

$$\sigma_{+}[f] = \frac{1}{C_{90}}\sqrt{\sum_{i=1}^{26}(max[(f_i^{+} - f_0),(f_i^{-} - f_0),0])^2},$$
$$\sigma_{-}[f] = \frac{1}{C_{90}}\sqrt{\sum_{i=1}^{26}(max[(f_0 - f_i^{+}),(f_0 - f_i^{-}),0])^2}. \quad (7.14)$$

$C_{90} = 1.64485$ is a re-scaling factor to convert the 90% CL variations into 1σ variations and f_0 is the nominal eigenvector value.

The impact of the PDF uncertainties on the acceptance was found to be negligible ($< 3\%$).

The experimental systematic uncertainties on the SM backgrounds estimated with MC-simulated data considered in the analysis presented here are described in the following.

Luminosity. The uncertainty of the total integrated luminosity for 2012 data collected by the ATLAS detector is found to be 2.8% [115], where this uncertainty is estimated by evaluating the luminosity scale using several luminosity- sensitive detectors, and comparisons are made of the long-term stability and accuracy of this calibration applied to the pp collisions for a given luminosity.

Pile-up. In the 2012 MC-simulated data, events with a certain $\langle\mu\rangle$ have a number of primary vertices comparable with data by $1.11\times\langle\mu\rangle$. Therefore, the uncertainty on the MC modelling of the pile-up is provided by assessing the up- and down-variation of the scale factor 1/1.11 .

Trigger. A conservative systematic uncertainty of 5% is assigned to the trigger simulation used in this analysis, to account for any differences in efficiency observed between the trigger in data and the MC trigger simulation. Particularly, the studies were performed by evaluating muon and electron triggering efficiency derived in data and MC simulation using a tag-and-probe method with Z+jets events [103]. These studies were performed for all single and dilepton triggers available in data in 2012.

***b*-tagging efficiency.** Uncertainties arising from a b-jet identification and mis-identification (charm and light-flavour jet rejection) efficiency are also taken into account in this analysis. ATLAS developed calibration methods based on $t\bar{t}$ events to exploit their large b-jet content, where the efficiencies are found to be jet p_{T} dependent. Scale factors with this jet p_{T} dependence are derived to correct the performance of the "b-tagging" in simulation to the one observed in data. The total uncertainties range

from 5% to 15% for jet p_{T} in the range 25 GeV to 300 GeV [116]. These uncertainties are found to be $\leq 1\%$ for all SRs described in this document.

Electrons. Uncertainties on the electron identification efficiencies, energy scales and resolutions are determined using $Z \to ee$, $W \to e\nu$ and $J/\psi \to ee$ events in data [60]. The reconstructed energy of electrons, referred to as Electron Energy Scale (EES), is determined by applying an in-situ calibration dependant on E_{T} and η. The corresponding Electron Energy Resolution (EER) uncertainties are also taken into account after the calibration is applied by comparing the di-electron mass spectrum in the $Z, J/\psi \to ee$ decays. Lastly, an uncertainty based on the electron identification efficiency (ESF) measurements is applied to all electrons which satisfy the "signal" criteria described in 6.2.1.

Muons. Uncertainties on the muon identification efficiencies, energy scales and resolutions are determined using $Z \to \mu\mu$ events in data [64]. The effect of the uncertainty on the muon momentum scale in the inner detector track and the muon spectrometer track has been studied for both combined and segment-tagged muons. The muon momentum scale is calibrated by comparing the invariant mass spectrum of the $J/\Psi \to \mu\mu$ and $Z \to \mu\mu$ decays between simulation and data. A smearing correction is derived to match the MC simulated di-muon mass resolution to the one measured in data. The uncertainty based on the muon identification efficiency measurements is applied to all muons which satisfy the "signal" criteria described in 6.2.2.

Taus. The systematic uncertainties on the hadronic tau energy scale (TES) were evaluated by combining individual visible decay products, namely neutral and charged pions [117]. These single particle uncertainties are given by an in-situ measurement comparing calorimeter energy measurements to momenta measured in the ID. The propagated uncertainty is also validated with studies using $Z \to \tau\tau$ decays. An uncertainty in the Tau Identification Scale Factor (TIDSF) is applied to all true "signal" taus in the event, is provided which accounts for the uncertainties from the BDT identification: jet-BDT and the electron-veto.

Jets. Uncertainties arising from the jet energy scale calibration and resolution are derived from a combination of simulated data, in-situ measurements and test-beam data. In particular, jet energy and angle corrections are determined from MC simulations to calibrate jets with transverse momenta greater than 20 GeV and pseudorapidities $|\eta| < 4.5$; and the jet energy scale systematic uncertainty is estimated using the

single-isolated hadron response measured in-situ and in test-beams, exploiting the transverse momentum balance between central and forward jets in events with di-jet events and studying systematic variations in MC simulations.

These uncertainties due to jet identification were found to be negligible in the SR presented here.

Missing Transverse Energy Measurement. The $E_{\mathrm{T}}^{\mathrm{miss}}$ is affected by various uncertainties coming from energy measurements of the physics objects that are taken as input in the calculation described in Section 6.2.5. Any variation in the electron, muon and/or jet energies will directly propagate to the $E_{\mathrm{T}}^{\mathrm{miss}}$ calculation. The uncertainty associated with the soft term of the $E_{\mathrm{T}}^{\mathrm{miss,CellOut}}$ is estimated by adjusting the energy scale (5%) and resolution of this term [102]. The uncertainties arising from the measurement of $E_{\mathrm{T}}^{\mathrm{miss}}$ is seen to be negligible in the SR discussed in this thesis.

7.6.2 Uncertainties on the Reducible Background

Systematic uncertainties on the reducible background estimated with the data-driven technique, the matrix method, can be classified into systematics arising from the various components entering the calculation on the weighted average fake rates defined in Equation 7.13: on the fake rate and real lepton efficiencies (f and ϵ respectively), the scale factors fake rates (sf), and the fake fractions (R), defined in Section 7.5.2. Below is a discussion of these sources of systematic uncertainties affecting the final estimate of the reducible background.

f and ϵ Efficiencies . The measured fake rate and real lepton efficiencies are taken from MC-simulated events which are corrected for any discrepancies with respect to data. These efficiencies showed a dependence on p_{T}, η and the number of τ prongs, therefore parametrised in these three kinematic variables. The dependency of these efficiencies on variables used in the event selection of the signal regions were thoroughly investigated by the 3L analysis team. The source of systematic uncertainties due to a dependence on other important event kinematics not taken into account by the parametrisation range between: $E_{\mathrm{T}}^{\mathrm{miss}}$ (0–7%), m_{T} (1–7%), $m_{\mathrm{T2}}^{\mathrm{max}}$ (0–18%), m_{SFOS} (0–18%), SFOS veto (0–5%), and η (1–5%) in the SR.

Fake Rate SF. The measurement of the fake rate scale factors for the different fake sources showed no strong dependence in p_{T}, $|\eta|$, and number of good vertices. There-

fore, they are fitted to a constant function. The central values of the scale factors are calculated without parametrisation on any variable and the differences with respect to the results of the fit in these three variables are assigned as a systematic uncertainty of the order of 5%.

Fake Fractions. The uncertainty on the fake fractions originates from a potential lack of knowledge of the relative contributions of a certain type of physics process in a given region (SR/VR). This uncertainty is covered by varying the yields of the physics processes by the following amounts: top processes by 50%, diboson processes by 50%, and V+jets processes by 30%.

Also included in the uncertainty on the reducible background is the the statistical uncertainty on the data events, used to apply the matrix equation and the statistical uncertainty from the fake rates measured in simulation.

7.6.3 Uncertainties on the Signal

The systematic uncertainties on the SUSY signal processes also include theoretical uncertainties on the calculated NLO cross sections, due to envelope of cross-section predictions using different PDF sets and factorisation and re-normalisation scales. These theoretical systematic uncertainties on all signal processes are evaluated by varying the factorisation and re-normalisation scales in PROSPINO and are calculated using the method described in ref. [118]. The uncertainties on the signal are in the 20-40% range, including the uncertainties due to the sources considered above for the irreducible background and the uncertainty due to limited Monte Carlo statistics.

Chapter 8

Results

In Chapter 7, the analysis strategy developed for the search for SUSY events in three lepton final states has been described. This chapter presents the interpretation of the results obtained, starting with an introduction of the statistical tools used, followed by an assessment of compatibility between the expected SM background and the observed events in data in all signal regions, finishing with the statistical interpretation of the results for each SUSY model considered.

8.1 Statistical Analysis Tools

The way to assess the statistical significance of the number of observed events in data with respect to the expected background is to define the probability that the observation agrees with the background-only hypothesis (H_0) or with the signal+background hypothesis (H_1) [109]. The so-called "p-values" for H_0 and H_1 are defined by:

$$\begin{aligned} p_0 &= P(q \leq q_{obs}|H_0) = \int_{-\infty}^{q_{obs}} f(q|b)dq \\ p_1 &= P(q \geq q_{obs}|H_1) = \int_{q_{obs}}^{\infty} f(q|s+b)dq \end{aligned} \tag{8.1}$$

where $f(q|b)$ and $f(q|s+b)$ are the probability density functions (pdfs) of the test statistic q, and q_{obs} is the observed result. The test statistic is a scalar quantity representative of the experiment. An illustration of both pdfs as a function of the test statistic is shown in Figure 8.1 along with their corresponding one-sided p-values.

A given "signal" hypothesis, corresponding in this case to a given SUSY model, is considered to be excluded when $p_1 \leq 0.05$, i.e. the probability of wrongly excluding the hypothesis is 5%. One can also say that the hypothesis is excluded at 95% Confidence Level (CL), which is equivalent to a value of Z_N (see Equation 7.1) of 1.64 σ.

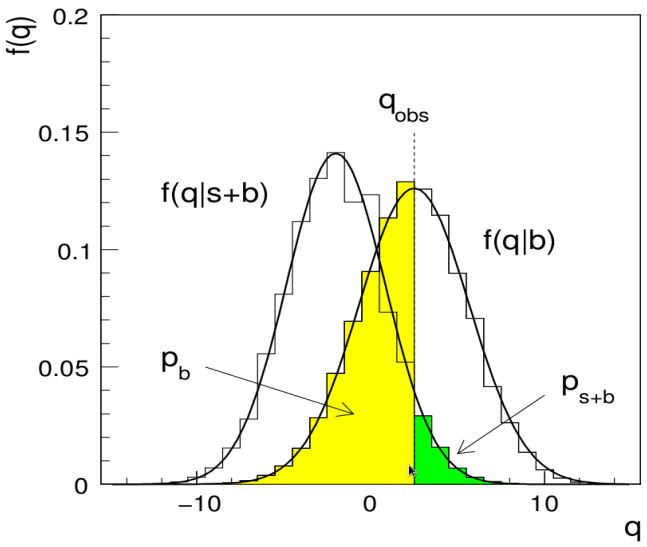

Figure 8.1: Distribution of the pdf of a test statistic (q) for background-only and signal+background hypotheses [109].

For the case where no excess is observed above the expected SM background then the alternative hypothesis (signal+background), predicted by some new physics model, can be excluded. This can be done by using the CL_s prescription [119, 120]. The CL_s is defined as a ratio of p-values (in order to prevent inconsistencies from cases when the signal yields are low):

$$CL_s = \frac{CL_{s+b}}{CL_b}, \tag{8.2}$$

where s is the expected signal,

$$CL_{s+b} = P(q \geq q_{obs}|s+b), \tag{8.3}$$

and

$$CL_b = P(q \geq q_{obs}|b). \tag{8.4}$$

Using this, a given hypothesis can be excluded if $CL_s \leq 0.05$.

Another procedure used for the exclusion of hypothesis is performed using a likelihood ratio [121] as a test statistic, which incorporates systematic uncertainties in its calculation. Starting for the case where there are n events measured in each signal region, with s signal and b background expected events, the expectation value for n can be written as

$$E[n] = \mu s + b \tag{8.5}$$

where μ is a strength parameter ($\mu = 0$ for background-only and $\mu = 1$ for signal+background

hypothesis). A resulting likelihood function can be constructed as a product of Poisson probabilities, one for each signal region,

$$\mathcal{L}(\mu,\theta) = \prod_{i=1}^{SR} \frac{(\mu s_i + b_i)^{n_i}}{n_i!} e^{-(\mu s_i + b_i)} \tag{8.6}$$

where the systematic uncertainties enter the likelihood calculation as nuisance parameters, θ, which must be simultaneously fitted from the data. To determine a value for μ, the likelihood function (see Equation 8.6) has to be maximised, which can be achieved by using the likelihood ratio as:

$$\lambda(\mu) = \frac{\mathcal{L}(\mu,\hat{\hat{\theta}})}{\mathcal{L}(\hat{\mu},\hat{\theta})} \tag{8.7}$$

where $\hat{\mu}$ and $\hat{\theta}$ are the maximum likelihood estimators, value which maximises $\mathcal{L}(\mu,\theta)$; and $\hat{\hat{\theta}}$ denotes the value of θ that maximises $\mathcal{L}$ given a specified μ. The inclusion of nuisance parameters broadens the profile likelihood distribution as a function of μ with respect to a function with fixed values.

The compatibility with the SM, upper limits on the expected and observed number of beyond-the-SM events and the exclusion limits obtained considering the events seen in data are assessed with a profile likelihood ratio test statistic. For the interpretation of the observed results in this analysis, the profile likelihood used is of the form

$$L(n|\mu,\boldsymbol{b},\boldsymbol{\theta}) \;=\; Pois(n|\lambda(\mu,\boldsymbol{b},\boldsymbol{\theta})) \;\times\; P_{\mathrm{Sys}}(\boldsymbol{\theta}^0,\boldsymbol{\theta})$$

where parameter n represents the number of observed events in data, $P(n|\lambda)$ a Poisson distribution modelling the expected event count in the SR, given an expectation value λ. The parameter μ is the SUSY signal strength to be tested, $\boldsymbol{b}$ is the background, and $\boldsymbol{\theta}$ describes the systematic uncertainties as nuisance parameters. P_{Sys} represents the constraints on systematic uncertainties and $\boldsymbol{\theta}^0$ are the nominal values around which $\boldsymbol{\theta}$ can be varied, for example when maximising the likelihood. P_{Sys} is the product of Gaussian distributions with $\sigma = 1$ (one Gaussian for each nuisance parameter). The modelling of the likelihood, calculation of the CL_s and p-values, were performed using the ATLAS HistFitter package (version HistFitter-00-00-33) [119, 109], a tool able to perform likelihood fits and their statistical interpretation.

8.2 Observed Events in Signal Regions

The observed number of events in all signal regions along with the total background expectations and uncertainties are shown in Table 8.1 (full breakdown can be found in App A). The quoted uncertainties include both the statistical and systematic components, as described in Section 7.6.

Table 8.1: Expected numbers of SM background events and observed numbers of data events in all signal regions for $20.3\,\text{fb}^{-1}$. Statistical and systematic uncertainties are included as described in section 7.6.

Sample	Irreducible	Reducible	Σ SM	Data
SR0τa-bin01	$15.8^{+3.6}_{-3.4}$	$6.7^{+2.4}_{-2.4}$	$\mathbf{23^{+4}_{-4}}$	**36**
SR0τa-bin02	$3.4^{+1.4}_{-1.4}$	$0.8^{+0.4}_{-0.4}$	$\mathbf{4.2^{+1.5}_{-1.5}}$	**5**
SR0τa-bin03	$9.0^{+1.7}_{-1.7}$	$1.6^{+0.7}_{-0.6}$	$\mathbf{10.6^{+1.8}_{-1.8}}$	**9**
SR0τa-bin04	$5.9^{+1.3}_{-1.3}$	$2.656^{+1.043}_{-0.988}$	$\mathbf{8.5^{+1.7}_{-1.6}}$	**9**
SR0τa-bin05	$8.6^{+1.8}_{-1.8}$	$4.3^{+1.6}_{-1.4}$	$\mathbf{12.9^{+2.4}_{-2.3}}$	**11**
SR0τa-bin06	$4.6^{+1.7}_{-1.6}$	$2.0^{+0.8}_{-0.8}$	$\mathbf{6.6^{+1.9}_{-1.8}}$	**13**
SR0τa-bin07	$10.1^{+1.7}_{-1.7}$	$4.0^{+1.5}_{-1.4}$	$\mathbf{14.1^{+2.2}_{-2.2}}$	**15**
SR0τa-bin08	$0.69^{+0.32}_{-0.31}$	$0.40^{+0.27}_{-0.26}$	$\mathbf{1.1^{+0.4}_{-0.4}}$	**1**
SR0τa-bin09	$18.3^{+3.3}_{-3.1}$	$4.1^{+1.3}_{-1.2}$	$\mathbf{22.4^{+3.6}_{-3.4}}$	**28**
SR0τa-bin10	$14.4^{+2.6}_{-2.7}$	$1.9^{+0.9}_{-0.8}$	$\mathbf{16.4^{+2.8}_{-2.8}}$	**24**
SR0τa-bin11	21^{+4}_{-4}	$5.7^{+2.1}_{-1.9}$	$\mathbf{27^{+5}_{-5}}$	**29**
SR0τa-bin12	$4.7^{+1.4}_{-1.4}$	$0.9^{+0.5}_{-0.4}$	$\mathbf{5.5^{+1.5}_{-1.4}}$	**8**
SR0τa-bin13	648^{+67}_{-66}	68^{+21}_{-19}	$\mathbf{715^{+70}_{-68}}$	**714**
SR0τa-bin14	216^{+33}_{-33}	$2.2^{+1.9}_{-2.0}$	$\mathbf{219^{+33}_{-33}}$	**214**
SR0τa-bin15	64^{+13}_{-13}	$1.2^{+0.6}_{-0.6}$	$\mathbf{65^{+13}_{-13}}$	**63**
SR0τa-bin16	$4.4^{+1.7}_{-1.5}$	$0.14^{+0.25}_{-0.27}$	$\mathbf{4.6^{+1.7}_{-1.5}}$	**3**
SR0τa-bin17	58^{+8}_{-7}	$11.3^{+3.5}_{-3.2}$	$\mathbf{69^{+9}_{-8}}$	**60**
SR0τa-bin18	$3.1^{+1.4}_{-1.4}$	$0.27^{+0.20}_{-0.20}$	$\mathbf{3.4^{+1.4}_{-1.4}}$	**1**
SR0τa-bin19	$1.0^{+0.4}_{-0.4}$	$0.17^{+0.16}_{-0.15}$	$\mathbf{1.2^{+0.4}_{-0.4}}$	**0**
SR0τa-bin20	$0.21^{+0.14}_{-0.14}$	$0.08^{+0.11}_{-0.10}$	$\mathbf{0.29^{+0.18}_{-0.17}}$	**0**
SR0τb	$2.4^{+1.1}_{-1.1}$	$1.5^{+0.4}_{-0.4}$	$\mathbf{3.8^{+1.2}_{-1.2}}$	**3**
SR1τ	$5.9^{+0.9}_{-0.8}$	$4.3^{+0.8}_{-0.8}$	$\mathbf{10.3^{+1.2}_{-1.2}}$	**13**
SR2τa	$1.9^{+0.5}_{-0.5}$	$5.1^{+0.7}_{-0.7}$	$\mathbf{6.9^{+0.8}_{-0.8}}$	**6**
SR2τb	$2.36^{+0.32}_{-0.34}$	$4.9^{+0.7}_{-0.7}$	$\mathbf{7.2^{+0.7}_{-0.8}}$	**5**

In order to quantify the probability of the background-only hypothesis to fluctuate to the observed number of events or higher, the one-sided p_0-value is calculated (truncated to 0.5 for $p_0 > 0.5$). Also, upper limits at 95% CL on the expected and observed number of beyond the SM events (N^{95}_{exp} and N^{95}_{obs}) for each signal region are calculated using the CL_s prescription. For both of these calculations the profile likelihood ratio is used as a test statistic. The p_0 and CL_s values are calculated using pseudo-experiments (also referred to as toys). A full description of these is given in Section 8.1.

Tables 8.2-8.3 shows the p_0-values of the background-only hypothesis and the the upper limits at 95% CL on the expected and observed number of BSM (signal) events for each signal region. Some fluctuations are visible in the binned SRs, particularly for SR0τa-bin01, when 23 ± 4 expected events have to be compared with 36 observed events. The local p_0-value for this bin is 0.015 corresponding to a significance of 2.16σ. Fluctuations are to be expected whenever the binning approach is implemented on a variable, i.e. the p-values are calculated locally (per bin) rather than globally, which can cause over- or under-fluctuations [122].

Table 8.2: Expected numbers of SM background events and observed numbers of data events in the signal regions SR0τb, SR1τ, SR2τa and SR2τb for 20.3 fb^{-1}. Statistical and systematic uncertainties are included as described in section 7.6. Also shown are the one-sided p_0-values and the upper limits at 95% CL on the expected and observed number of beyond-the-SM events (N^{95}_{exp} and N^{95}_{obs}) for each signal region, calculated using pseudo-experiments and the CL$_s$ prescription, described in Section 8.1. For p_0-values below 0.5, the observed number of standard deviations, σ, is also shown in parentheses.

Sample	SR0τb	SR1τ	SR2τa	SR2τb
Total SM	3.8 ± 1.2	10.3 ± 1.2	6.9 ± 0.8	$7.2^{+0.7}_{-0.8}$
Data	3	13	6	5
p_0 (σ)	0.50	0.19 (0.86)	0.50	0.50
N^{95}_{exp}	$5.6^{+2.2}_{-1.4}$	$8.1^{+3.2}_{-2.2}$	$6.8^{+2.7}_{-1.9}$	$6.7^{+2.8}_{-1.8}$
N^{95}_{obs}	5.4	10.9	6.0	5.2

Table 8.3: Expected numbers of SM background events and observed numbers of data events in the 20 bins in signal region SR0τa for 20.3 fb^{-1}. Statistical and systematic uncertainties are included as described in section 7.6. Also shown are the one-sided p_0-values and the upper limits at 95% CL on the expected and observed number of beyond the SM events (N^{95}_{exp} and N^{95}_{obs}) for each signal region, calculated using pseudo-experiments and the CL$_s$ prescription, described in Section 8.1. For p_0-values below 0.5, the observed number of standard deviations, σ, is also shown in parentheses.

	Bin01	Bin02	Bin03	Bin04	Bin05	Bin06	Bin07
$\sum$ SM	23 ± 4	4.2 ± 1.5	10.6 ± 1.8	$8.5^{+1.7}_{-1.6}$	$12.9^{+2.4}_{-2.3}$	$6.6^{+1.9}_{-1.8}$	14.1 ± 2.2
Data	36	5	9	9	11	13	15
p_0	0.02	0.35	0.50	0.40	0.50	0.03	0.37
(σ)	(2.16)	(0.38)		(0.26)		(1.91)	(0.33)
N^{95}_{exp}	$14.1^{+5.6}_{-3.6}$	$6.2^{+2.5}_{-1.7}$	$8.4^{+3.1}_{-2.3}$	$7.7^{+3.1}_{-2.1}$	$9.0^{+3.6}_{-2.5}$	$8.0^{+3.2}_{-1.9}$	$9.6^{+3.9}_{-2.5}$
N^{95}_{obs}	26.8	6.9	7.3	8.4	7.9	14.4	10.8

	Bin08	Bin09	Bin10	Bin11	Bin12	Bin13	Bin14
Total SM	1.1 ± 0.4	$22.4^{+3.6}_{-3.4}$	16.4 ± 2.8	27 ± 5	$5.5^{+1.5}_{-1.4}$	715 ± 70	219 ± 33
Data	1	28	24	29	8	714	214
p_0 (σ)	0.50	0.13	0.07	0.39	0.21	0.50	0.50
(σ)		(1.12)	(1.50)	(0.28)	(0.82)		
N^{95}_{exp}	$3.7^{+1.5}_{-0.9}$	$12.7^{+4.9}_{-3.5}$	$11.3^{+4.5}_{-3.1}$	$13.8^{+5.4}_{-3.7}$	$6.9^{+2.9}_{-1.7}$	133^{+46}_{-36}	66^{+24}_{-18}
N^{95}_{obs}	3.7	18.0	18.3	15.3	9.2		

	Bin15	Bin16	Bin17	Bin18	Bin19	Bin20
Total SM	65 ± 13	$4.6^{+1.7}_{-1.5}$	69^{+9}_{-8}	3.4 ± 1.4	1.2 ± 0.4	$0.29^{+0.18}_{-0.17}$
Data	63	3	60	1	0	0
p_0	0.50	0.50	0.50	0.50	0.50	0.50
N^{95}_{exp}	$28.6^{+10.1}_{-7.2}$	$5.9^{+2.6}_{-1.5}$	$21.4^{+8.2}_{-5.6}$	$4.8^{+2.0}_{-1.1}$	$3.7^{+1.4}_{-0.7}$	$3.0^{+0.8}_{-0.0}$
N^{95}_{obs}	27.6	5.2	18.8	3.7	3.0	3.0

Kinematic distributions

Figure 8.2 shows the SM expectations and the observations in data in the individual SR0τa bins as well as the distribution of $E_{\mathrm{T}}^{\mathrm{miss}}$, m_{T} and m_{SFOS} in the combination of all SR0τa regions. For illustration purposes, the distributions are also shown for two representative SUSY benchmark points, one for each of the most sensitive models for these signal regions: WZ-mediated and $\tilde{\ell}_L$-mediated simplified models.

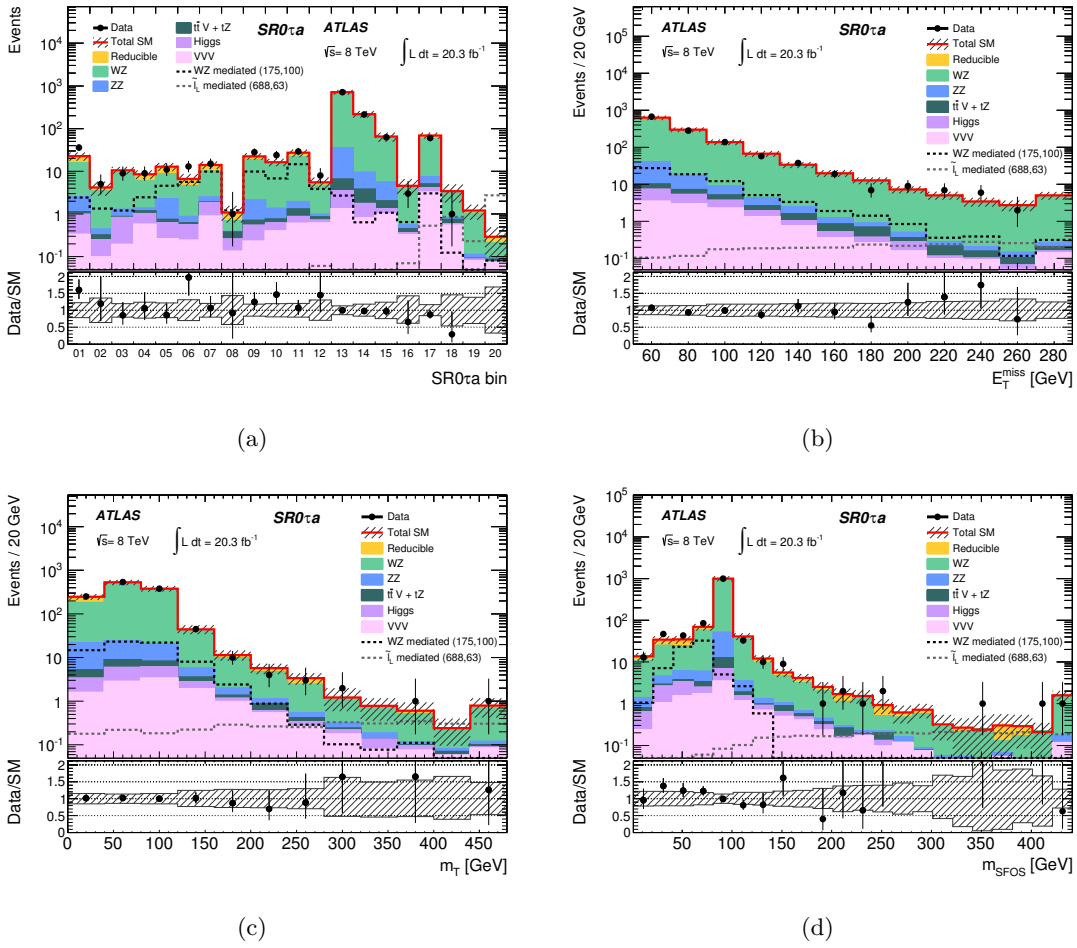

Figure 8.2: Expected distributions of SM background events and observed data distributions in (a) the binned signal regions SR0τa. The distributions of (b) $E_{\mathrm{T}}^{\mathrm{miss}}$, (c) m_{T} and (d) m_{SFOS} are shown in the summation of all SR0τa regions prior to the requirements on these variables. Also shown are the respective contributions of the various background processes as described in the legend. Both the statistical and systematic uncertainties are shown. The plots also show the distribution for signal hypotheses, where the parentheses following the simplified model denote the mass parameters in GeV as $(m(\tilde{\chi}_1^{\pm}, \tilde{\chi}_2^0), m(\tilde{\chi}_1^0))$ [1].

Figures 8.3-8.5 show the distributions of the quantities $\Delta\phi_{\ell\ell'}^{\mathrm{min}}$, $E_{\mathrm{T}}^{\mathrm{miss}}$, $m_{\mathrm{T2}}^{\mathrm{max}}$ and $m_{\tau\tau}$

chosen in the SR0τb, SR1τ, SR2τa and SR2τb regions respectively, prior to the requirements made on the variables themselves. The arrows in the figures shows where the requirement on the variable is placed. Also shown are the distributions for representative SUSY benchmark points selected for the signal hypotheses. In the case of the $\tilde{\tau}_L$-mediated simplified model, points are shown only in the $m_{\mathrm{T2}}^{\mathrm{max}}$ distribution for SR2τa and in case of the Wh-mediated simplified model, points are shown only in the $\Delta\phi_{\ell\ell'}^{\mathrm{min}}$, $E_{\mathrm{T}}^{\mathrm{miss}}$and $m_{\tau\tau}$ distributions for SR0τb, SR1τ and SR2τb regions respectively.

It is important to highlight the signal shape feature seen in the $m_{\mathrm{T2}}^{\mathrm{max}}$ distribution (see Figure 8.5(a)), where at high values of $m_{\mathrm{T2}}^{\mathrm{max}}$ there is a clear separation from the SM background. This shows the importance of this particular variable when it came to defining SR2τa.

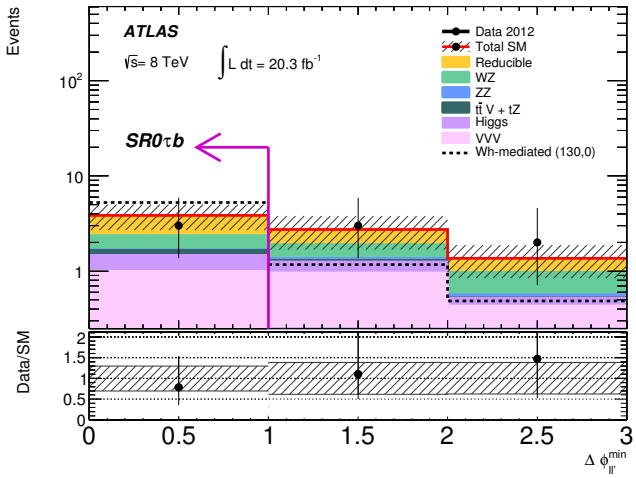

Figure 8.3: Expected distributions of SM background events and observed data for $\Delta\phi_{\ell\ell'}^{\mathrm{min}}$ in SR0τb, prior to the requirements on this variable. Arrows indicate the limits on the value of the variable used to define the signal region. Also shown are the respective contributions of the various background processes as described in the legend. Both the statistical and systematic uncertainties are shown. The plots also show the distribution for signal hypotheses, where the parentheses following the simplified model denote the mass parameters in GeV as $(m(\tilde{\chi}_1^{\pm}, \tilde{\chi}_2^0), m(\tilde{\chi}_1^0))$ [1].

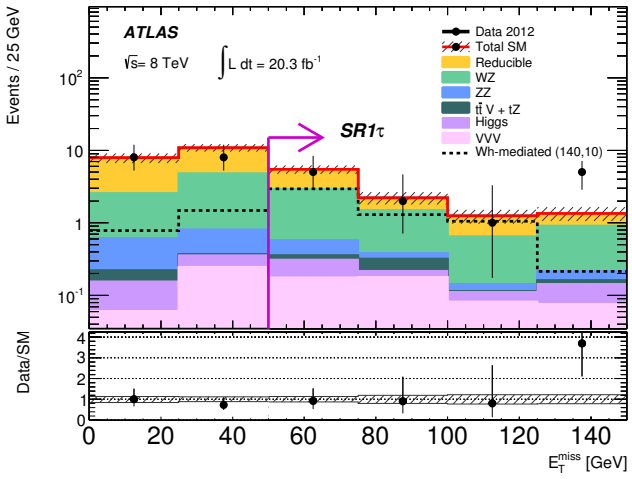

Figure 8.4: Expected distributions of SM background events and observed data for $E_{\mathrm{T}}^{\mathrm{miss}}$ in SR1τ, prior to the requirement on this variable. Arrows indicate the limits on the value of the variable used to define the signal regions. Also shown are the respective contributions of the various background processes as described in the legend. Both the statistical and systematic uncertainties are shown. The plots also show the distribution for signal hypotheses, where the parentheses following the simplified model denote the mass parameters in GeV as $(m(\tilde{\chi}_1^{\pm}, \tilde{\chi}_2^0), m(\tilde{\chi}_1^0))$ [1].

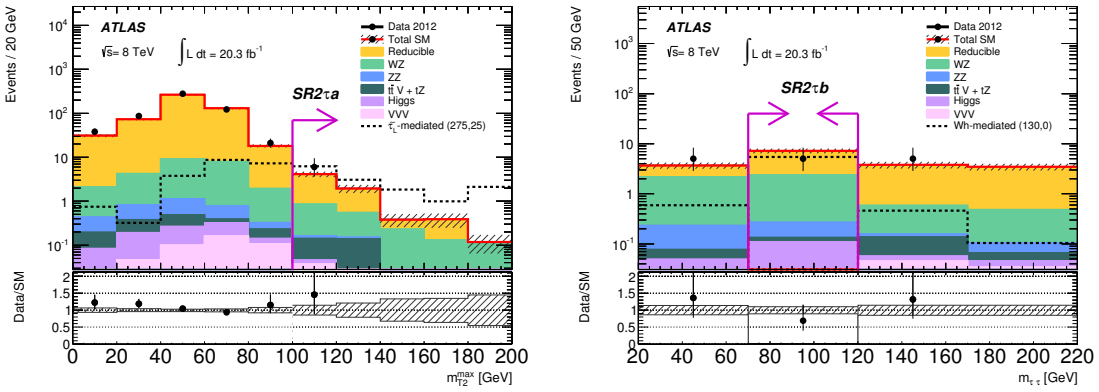

(a) (b)

Figure 8.5: Expected distributions of SM background events and observed data for (a) $m_{\mathrm{T2}}^{\mathrm{max}}$ and (b) $m_{\tau\tau}$ variables in SR2τa and SR2τb regions respectively, prior to the requirements on these variables. Arrows indicate the limits on the values of the variables used to define the signal regions. Also shown are the respective contributions of the various background processes as described in the legend. Both the statistical and systematic uncertainties are shown. The plots also show the distribution for signal hypotheses, where the parentheses following the simplified model denote the mass parameters in GeV as $(m(\tilde{\chi}_1^{\pm}, \tilde{\chi}_2^0), m(\tilde{\chi}_1^0))$ [1].

The number of observed events is consistent with the SM expectation in all signal regions, within uncertainties. Since no significant excess is observed, these results are used to derive exclusion limits on the simplified and pMSSM models described in section 2.2.

8.3 Statistical Interpretation

Exclusion limits are calculated by statistically combining results from a number of disjoint signal regions in order to obtain maximum exclusion. SR2τa and SR2τb are not disjointed, hence only one of the two must be chosen for the combination based on the highest sensitivity provided for the model studied. For the $\tilde{\ell}_L$-mediated, WZ-mediated and $\tilde{\tau}_L$-mediated simplified models and for the pMSSM scenarios, SR0τa, SR0τb, SR1τ and SR2τa are statistically combined. For the Wh-mediated simplified model, the statistical combination of SR0τa, SR0τb, SR1τ and SR2τb is used.

For the exclusion limits, the observed and expected 95% CL limit contours are calculated using MC pseudo-experiments for each SUSY model point, taking into account the theoretical and experimental uncertainties on the SM background and the experimental uncertainties on the signal, σ_{exp}, as well as the Poissonian fluctuations on the number of observed events. The yellow bands in the figures for the exclusion contours show the impact of $\pm 1\sigma$ variations of σ_{exp} on the expected limit. The theoretical uncertainties on the signal cross section, $\sigma^{\text{SUSY}}_{\text{theory}}$, are not included, however, their impact is shown as the $\pm 1\sigma$ variation bands (red dashed lines) on the observed limit.

8.3.1 Model Dependent Interpretation: Simplified Models

Figure 8.6 shows the $\tilde{\ell}_L$-mediated simplified model interpretation, where the masses of the degenerate $\tilde{\chi}_1^{\pm}$ and $\tilde{\chi}_2^0$ are excluded up to 700 GeV. In the WZ-mediated simplified model shown in figure 8.7, $\tilde{\chi}_1^{\pm}$ and $\tilde{\chi}_2^0$ masses are excluded up to 345 GeV.

The over- (under-) fluctuations in the observed results in the signal regions lead to a weaker (stronger) observed exclusion limits with respect to the expected for the compressed scenarios (small $m_{\tilde{\chi}_2^0} - m_{\tilde{\chi}_1^0}$) in both the $\tilde{\ell}_L$-mediated and WZ-mediated simplified models.

The two exclusion limits shown in Figures 8.6-8.7 improve those reported by the previous ATLAS publication [103], also shown in the figures as a blue line. For the $\tilde{\ell}_L$-mediated simplified model and the WZ-mediated simplified model, an improvement of $\sim$200 GeV for high $\tilde{\chi}_1^{\pm}$ and $\tilde{\chi}_2^0$ masses is seen.

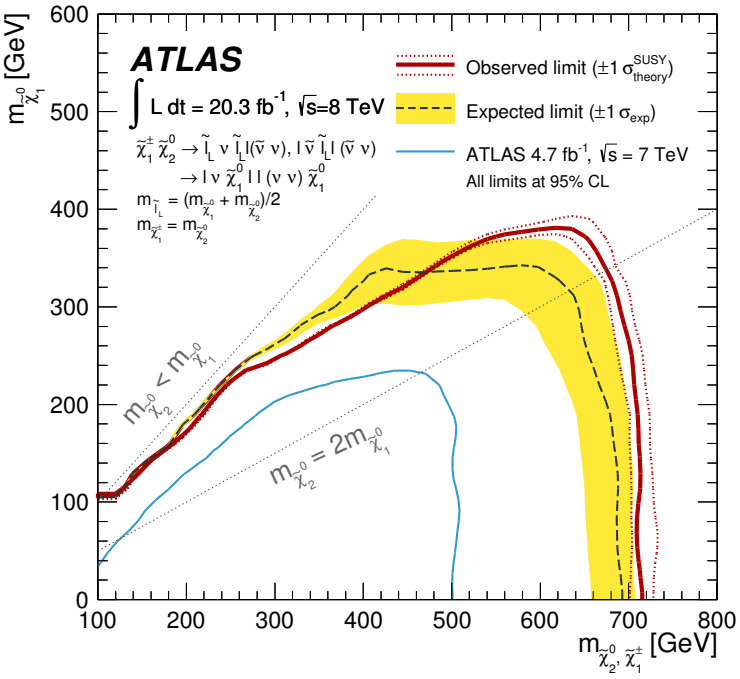

Figure 8.6: Observed and expected 95% CL exclusion contours for chargino and neutralino production in the $\tilde{\ell}_L$-mediated simplified models [1]. The band around the expected limit shows the $\pm 1\sigma$ variations of the expected limit, including all uncertainties except theoretical uncertainties on the signal cross section. The dotted lines around the observed limit indicate the sensitivity to $\pm 1\sigma$ variations of these theoretical uncertainties. The blue contour corresponds to the 7 TeV limits from the ATLAS three-lepton analysis. Linear interpolation is used to account for the discrete nature of the signal grids.

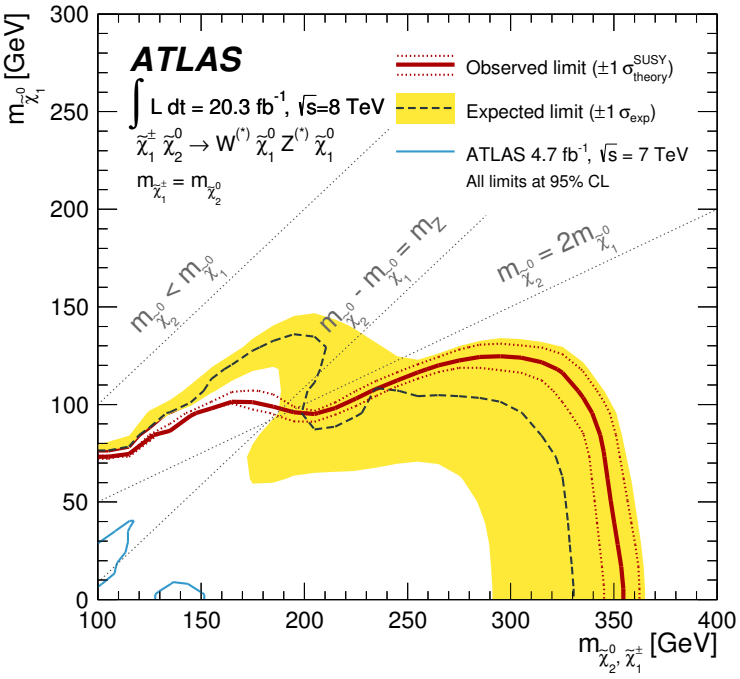

Figure 8.7: Observed and expected 95% CL exclusion contours for chargino and neutralino production in the WZ-mediated simplified models [1]. The band around the expected limit shows the $\pm 1\sigma$ variations of the expected limit, including all uncertainties except theoretical uncertainties on the signal cross section. The dotted lines around the observed limit indicate the sensitivity to $\pm 1\sigma$ variations of these theoretical uncertainties. The blue contour corresponds to the 7 TeV limits from the ATLAS three-lepton analysis. Linear interpolation is used to account for the discrete nature of the signal grids.

In the $\tilde{\ell}_L$-mediated simplified model, the region with high-m_{SFOS} bins in SR0τa (i.e. SR0τa-bin20) offers the best sensitivity to scenarios with high $\tilde{\chi}_1^{\pm}$ and $\tilde{\chi}_2^0$ masses, and the low-m_{SFOS} bins in SR0τa to scenarios where the $m_{\tilde{\chi}_2^0} - m_{\tilde{\chi}_1^0}$ is small. In the WZ-mediated simplified model, SR0τa-bin16 offers the best sensitivity to scenarios with high $\tilde{\chi}_1^{\pm}$ and $\tilde{\chi}_2^0$ masses, and SR0τa-bin01 to scenarios where the $m_{\tilde{\chi}_2^0} - m_{\tilde{\chi}_1^0}$ is small. There is a reduced sensitivity to scenarios in the $m_{\tilde{\chi}_2^0} - m_{\tilde{\chi}_1^0} = m_Z$ region as the signal populates regions with high WZ background. These statements are verified by computing the observed and expected CL_s values, which are shown in Figure 8.8, for the $\tilde{\ell}_L$- and WZ-mediated simplified models using only bins SR0τa-bin20 and SR0τa-bin16 respectively.

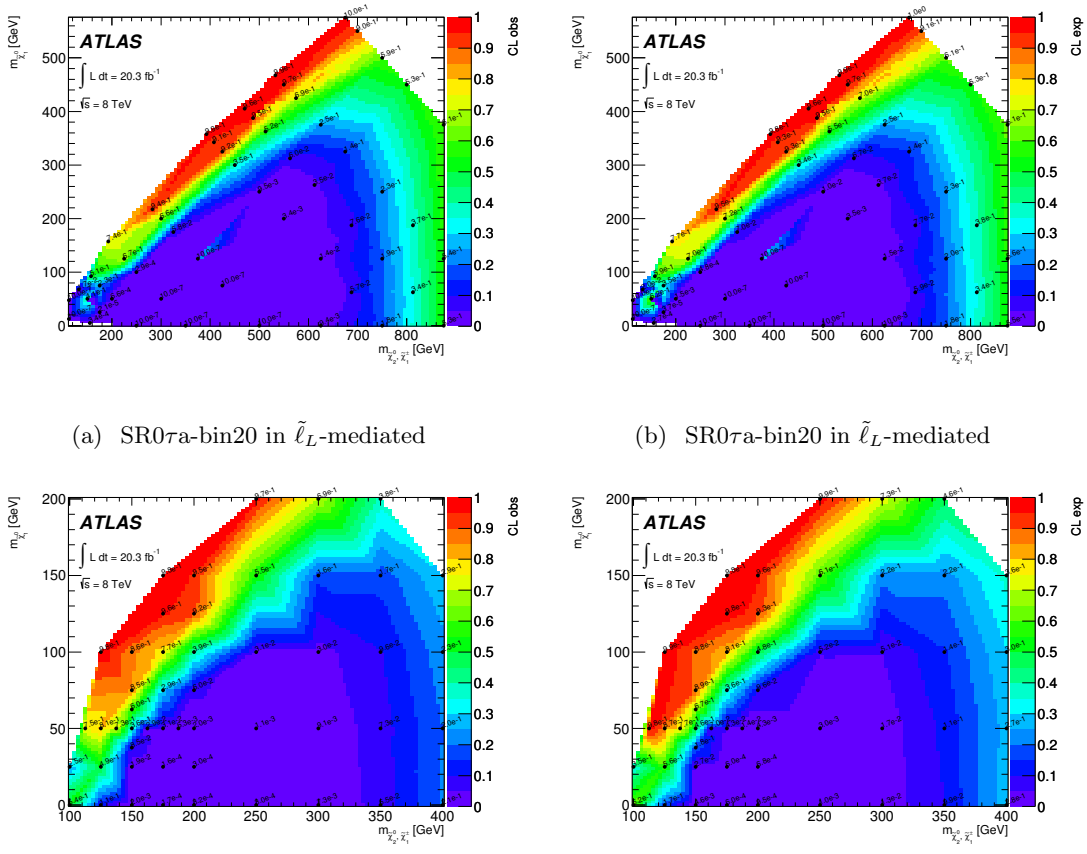

(a) SR0τa-bin20 in $\tilde{\ell}_L$-mediated

(b) SR0τa-bin20 in $\tilde{\ell}_L$-mediated

(c) SR0τa-bin16 in WZ-mediated

(d) SR0τa-bin16 in WZ-mediated

Figure 8.8: The observed (left) and expected (right) CL_s for (a-b) $\tilde{\ell}_L$-mediated and (c-d) WZ-mediated, using pseudo-experiments [1]. Each signal point in the parameter space is shown by a black dot, and the numbers show the observed or expected CL_s at each point, calculated using the prescription defined in Section 8.1. For $\tilde{\ell}_L$-mediated, only SR0τa bin 20 is used. For WZ-mediated, only SR0τa bin 16 is used.

In the $\tilde{\tau}_L$-mediated simplified model, $\tilde{\chi}_1^{\pm}$ and $\tilde{\chi}_2^0$ masses are excluded up to 380 GeV

for massless $\tilde{\chi}_1^0$ as shown in figure 8.9. In the Wh-mediated simplified model shown in figure 8.10, $\tilde{\chi}_1^\pm$ and $\tilde{\chi}_2^0$ masses are excluded up to 148 GeV.

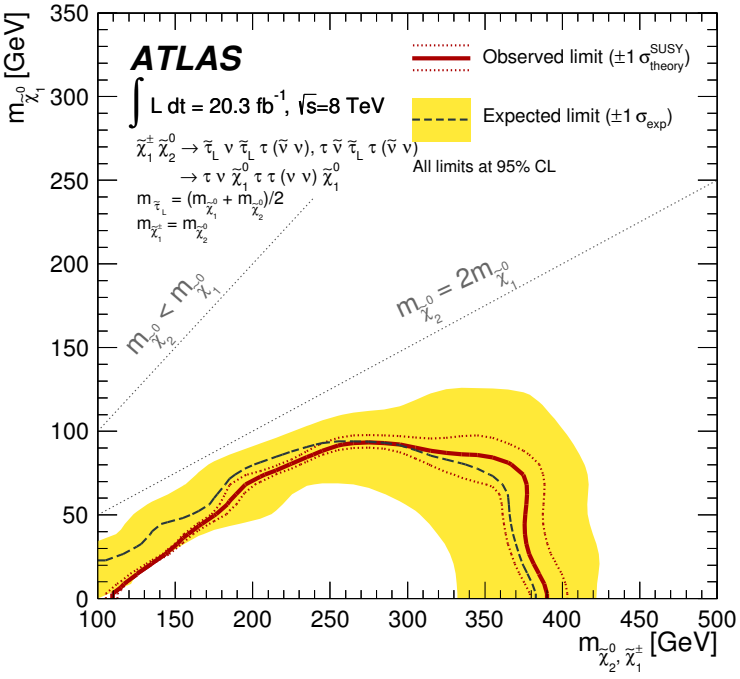

(a) $\tilde{\tau}_L$-mediated simplified model

Figure 8.9: Observed and expected 95% CL exclusion contours for chargino and neutralino production in the $\tilde{\tau}_L$-mediated simplified model [1]. The band around the expected limit shows the $\pm 1\sigma$ variations of the expected limit, including all uncertainties except theoretical uncertainties on the signal cross section. The dotted lines around the observed limit indicate the sensitivity to $\pm 1\sigma$ variations of these theoretical uncertainties. Linear interpolation is used to account for the discrete nature of the signal grids.

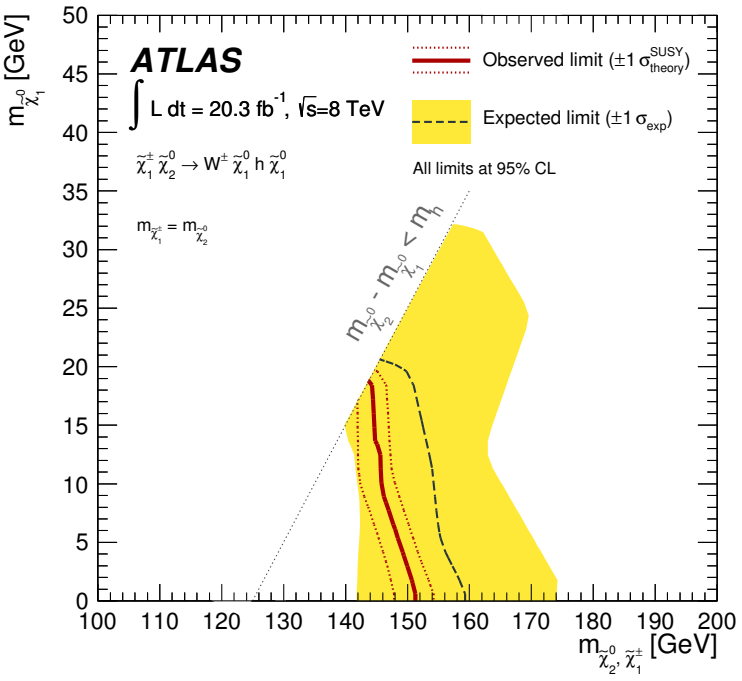

(a) Wh-mediated simplified model

Figure 8.10: Observed and expected 95% CL exclusion contours for chargino and neutralino production in the Wh-mediated simplified model [1]. The band around the expected limit shows the $\pm 1\sigma$ variations of the expected limit, including all uncertainties except theoretical uncertainties on the signal cross section. The dotted lines around the observed limit indicate the sensitivity to $\pm 1\sigma$ variations of these theoretical uncertainties. Linear interpolation is used to account for the discrete nature of the signal grids.

The low m_{SFOS} SR0τa bins offer the best sensitivity to the small $m_{\tilde{\chi}_2^0} - m_{\tilde{\chi}_1^0}$ scenarios in the $\tilde{\tau}_L$-mediated simplified model, and SR2τa to the high-mass $\tilde{\chi}_1^{\pm}$, $\tilde{\chi}_2^0$ scenarios. The results in the low m_{SFOS} SR0τa bins lead to a weaker observed exclusion than expected for the compressed scenarios. In case of the Wh-mediated simplified model, regions SR0τa, SR0τb, SR1τ and SR2τb jointly offer the best sensitivity. The over-fluctuations in the observed results in some SR0τa bins and SR1τ, which were specifically designed to provide sensitivity to this model, are responsible for the observed exclusion contour being slightly weaker than the expected. These statements are verified by computing the observed and expected CL_s values, which are shown in Figure 8.11, for the $\tilde{\tau}_L$- and Wh-mediated simplified models using only bins SR2τa and SR2τb respectively.

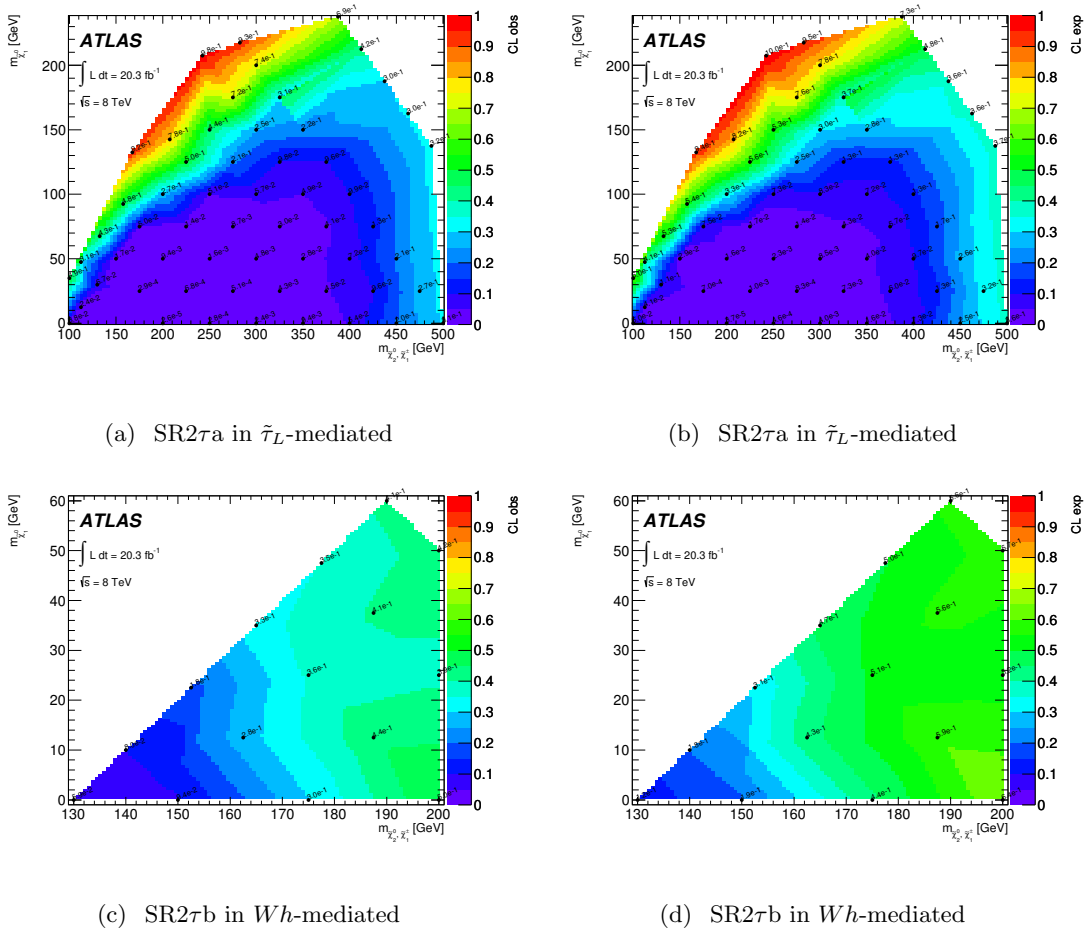

(a) SR2τa in $\tilde{\tau}_L$-mediated

(b) SR2τa in $\tilde{\tau}_L$-mediated

(c) SR2τb in Wh-mediated

(d) SR2τb in Wh-mediated

Figure 8.11: The observed (left) and expected (right) CL_s for (a-b) $\tilde{\tau}_L$-mediated and (c-d) Wh-mediated, using pseudo-experiments [1]. Each signal point in the parameter space is shown by a black dot, and the numbers show the observed or expected CL_s at each point, calculated using the prescription defined in Section 8.1. For $\tilde{\tau}_L$-mediated, SR2τa is used. For Wh-mediated, SR2τb is used.

8.3.2 Model Dependent Interpretation: pMSSM

In the pMSSM scenarios, for a given value of M_1 , the sensitivity for high values of M_2 and μ, and therefore for high values of chargino and heavy neutralino (not the LSP) masses, is driven by the decrease of the production cross section.

Figures 8.12-8.15 show the exclusion contours for pMSSM $\tilde{\ell}_{\mathrm{R}}$ scenarios and the pMSSM $\tilde{\tau}_{\mathrm{R}}$ scenario, which have limited sensitivity in the regions with $M_1 \sim M_2 \ll \mu$, due to small $m_{\tilde{\chi}_2^0} - m_{\tilde{\chi}_1^0}$ or $m_{\tilde{\chi}_1^\pm} - m_{\tilde{\chi}_1^0}$. Values for the masses of $\tilde{\chi}_1^\pm$ and $\tilde{\chi}_1^0$ are shown in the figure as gray isolines.

In the case of the pMSSM $\tilde{\ell}_{\mathrm{R}}$ with $M_1 = 250$ GeV and $\tilde{\tau}_{\mathrm{R}}$ scenarios shown in Figure 8.14 and Figure 8.15 respectively, the small mass splittings ($m_{\tilde{\chi}_1^\pm} - m_{\tilde{\chi}_1^0}$) also reduces the

sensitivity in the $M_1 \sim \mu \ll M_2$ region. In particular, the pMSSM $\tilde{\ell}_R$ scenario with $M_1 = 250$ GeV, the $M_2 \gtrsim 250$ GeV and $\mu \gtrsim 250$ GeV, a region characterised by small $m_{\tilde{\chi}_1^\pm, \tilde{\chi}_2^0} - m_{\tilde{\chi}_1^0}$, due to the over-fluctuation seen in SR0τa-bin01 the observed exclusion region is significantly smaller than that expected.

For the pMSSM no $\tilde{\ell}$ scenarios (Figures 8.16), in the region with $M_2 \gtrsim 200$ GeV and $\mu \gtrsim 200$ GeV the decay mode $\tilde{\chi}_2^0 \to h\tilde{\chi}_1^0$ is kinematically allowed and reduces the sensitivity due to its branching ratios into three light lepton final states.

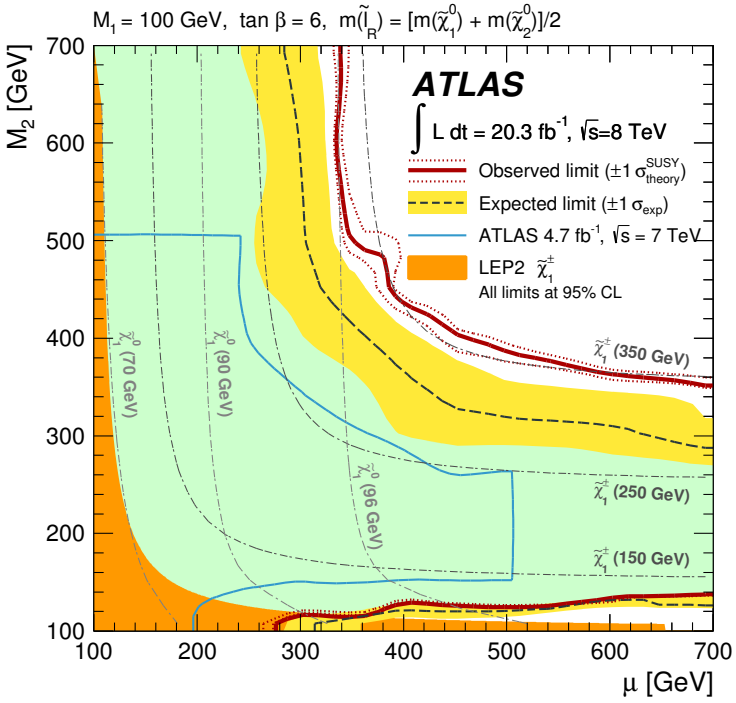

(a) pMSSM $\tilde{\ell}_R$, M_1=100 GeV

Figure 8.12: Observed and expected 95% CL exclusion contours in the pMSSM model with sleptons, $M_1 = 100$ GeV [1]. The band around the expected limit shows the $\pm 1\sigma$ variations of the expected limit, including all uncertainties except theoretical uncertainties on the signal cross section. The dotted lines around the observed limit indicate the sensitivity to $\pm 1\sigma$ variations of these theoretical uncertainties. The area covered by the -1σ expected limit is shown in green. The blue contours correspond to the 7 TeV limits from the ATLAS three-lepton analysis. Linear interpolation is used to account for the discrete nature of the signal grids.

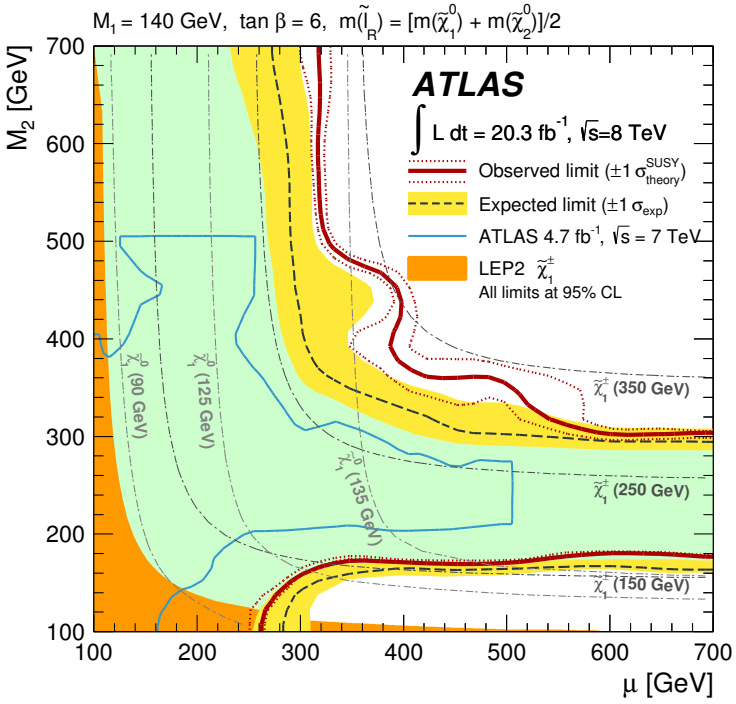

(a) pMSSM $\tilde{\ell}_{\mathrm{R}}$, M_1=140 GeV

Figure 8.13: Observed and expected 95% CL exclusion contours in the pMSSM model with sleptons, $M_1 = 140$ GeV. The band around the expected limit shows the $\pm 1\sigma$ variations of the expected limit, including all uncertainties except theoretical uncertainties on the signal cross section. The dotted lines around the observed limit indicate the sensitivity to $\pm 1\sigma$ variations of these theoretical uncertainties. The area covered by the -1σ expected limit is shown in green. The blue contours correspond to the 7 TeV limits from the ATLAS three-lepton analysis. Linear interpolation is used to account for the discrete nature of the signal grids.

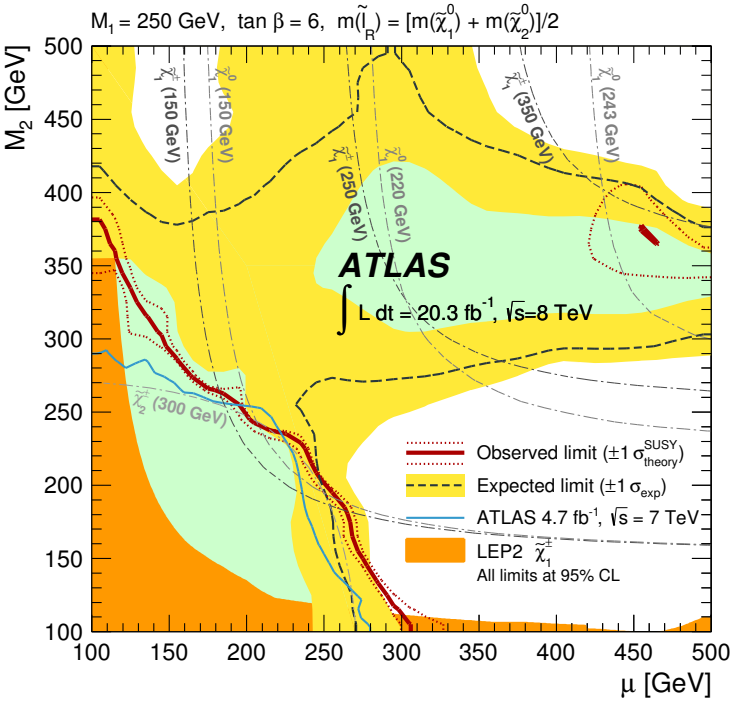

(a) pMSSM $\tilde{\ell}_{\mathrm{R}}$, M_1=250 GeV

Figure 8.14: Observed and expected 95% CL exclusion contours in the pMSSM model with sleptons, $M_1 = 250$ GeV [1]. The band around the expected limit shows the $\pm 1\sigma$ variations of the expected limit, including all uncertainties except theoretical uncertainties on the signal cross section. The dotted lines around the observed limit indicate the sensitivity to $\pm 1\sigma$ variations of these theoretical uncertainties. The area covered by the -1σ expected limit is shown in green. The blue contours correspond to the 7 TeV limits from the ATLAS three-lepton analysis. Linear interpolation is used to account for the discrete nature of the signal grids.

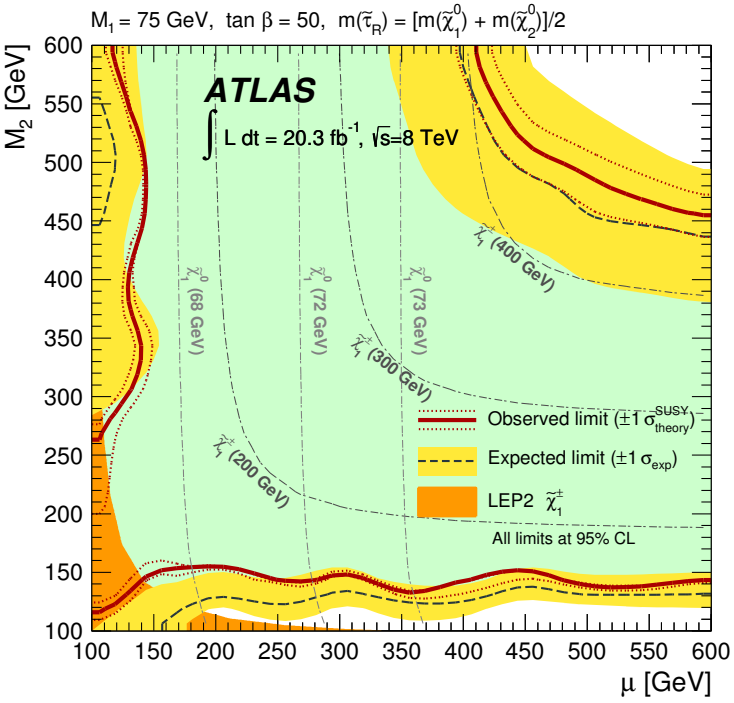

(a) pMSSM $\tilde{\tau}_{\mathrm{R}}$, M_1=75 GeV

Figure 8.15: Observed and expected 95% CL exclusion contours in the pMSSM model with $\tilde{\tau}_{\mathrm{R}}$ [1]. The band around the expected limit shows the $\pm 1\sigma$ variations of the expected limit, including all uncertainties except theoretical uncertainties on the signal cross section. The dotted lines around the observed limit indicate the sensitivity to $\pm 1\sigma$ variations of these theoretical uncertainties. The area covered by the -1σ expected limit is shown in green. Linear interpolation is used to account for the discrete nature of the signal grids.

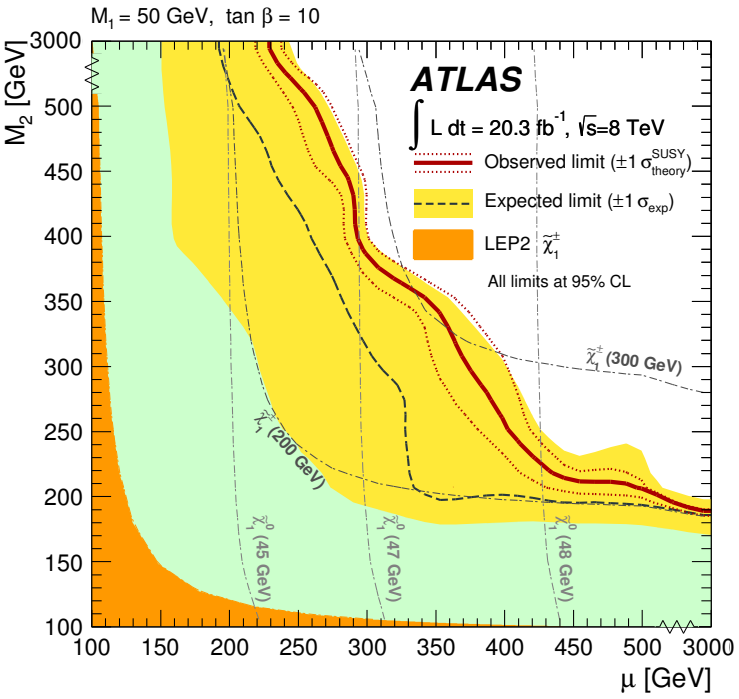

(a) pMSSM no $\tilde{\ell}$, M_1=50 GeV

Figure 8.16: Observed and expected 95% CL exclusion contours in the pMSSM model with no $\tilde{\ell}$ [1]. The band around the expected limit shows the $\pm 1\sigma$ variations of the expected limit, including all uncertainties except theoretical uncertainties on the signal cross section. The dotted lines around the observed limit indicate the sensitivity to $\pm 1\sigma$ variations of these theoretical uncertainties. The area covered by the -1σ expected limit is shown in green. Linear interpolation is used to account for the discrete nature of the signal grids.

Chapter 9

Conclusion

This thesis summarises the work done during my PhD at the University of Sussex on the search at ATLAS for the production of charginos and neutralinos decaying into final states with three leptons ($e/\mu/\tau$) and missing transverse momentum. The analysis was performed using 20.3 fb^{-1} of the $\sqrt{s} = 8$ TeV proton-proton collision data delivered by the LHC and recorded with the ATLAS detector in 2012. The results presented in Chapter 8 show no significant excess of events above SM expectations with respect to what was found in data. These are interpreted in different simplified SUSY models and in various pMSSM scenarios, detailed in Section 2.2.1. For the simplified SUSY models with intermediate slepton decays, degenerate $\tilde{\chi}_1^{\pm}$ and $\tilde{\chi}_2^0$ masses up to 700 GeV are excluded for large mass differences with the $\tilde{\chi}_1^{\pm}$, while for the simplified SUSY models with gauge boson (W, Z) decays, the mass exclusion limit reaches 345 GeV. These limits improve upon the previous ATLAS results in ref [103] by almost 200 GeV. For the newly explored simplified SUSY models with intermediate staus, degenerate $\tilde{\chi}_1^{\pm}$ and $\tilde{\chi}_2^0$ masses up to 380 GeV are excluded, while for the simplified SUSY models with intermediate Higgs boson decays, degenerate $\tilde{\chi}_1^{\pm}$ and $\tilde{\chi}_2^0$ masses up to 148 GeV are excluded.

This analysis has been published in a refereed paper [1] in April 2014.

Appendix A

Observed Data

This Section provides a full process breakdown for the MC-based estimates of the irreducible background in each SR. Also shown, are the MM estimates for the reducible background, the total expectation of SM and the observed data. These estimates are provided in Table A.1-A.3.

Table A.1: Expected numbers of SM background events and observed numbers of data events in the signal regions SR0τa-bin01–bin12 for 20.3 fb^{-1}. Statistical and systematic uncertainties are included as described in section 7.6.

Sample	SR0τa-bin01	SR0τa-bin02	SR0τa-bin03	SR0τa-bin04	SR0τa-bin05	SR0τa-bin06
WZ	$13.2^{+3.4}_{-3.2}$	3.0 ± 1.4	7.8 ± 1.6	$4.5^{+1.1}_{-1.0}$	6.3 ± 1.6	3.7 ± 1.6
ZZ	$1.4^{+0.6}_{-0.5}$	0.12 ± 0.06	0.40 ± 0.14	0.20 ± 0.18	1.5 ± 0.5	$0.25^{+0.14}_{-0.11}$
$t\bar{t}V + tZ$	0.14 ± 0.05	0.07 ± 0.04	$0.04^{+0.05}_{-0.04}$	0.14 ± 0.13	0.11 ± 0.08	$0.047^{+0.022}_{-0.021}$
VVV	0.33 ± 0.33	0.10 ± 0.10	0.19 ± 0.19	0.6 ± 0.6	$0.26^{+0.27}_{-0.26}$	0.24 ± 0.24
Higgs	0.66 ± 0.26	0.15 ± 0.08	0.64 ± 0.22	$0.46^{+0.18}_{-0.17}$	$0.36^{+0.14}_{-0.15}$	$0.33^{+0.13}_{-0.12}$
Reducible	6.7 ± 2.4	0.8 ± 0.4	$1.6^{+0.7}_{-0.6}$	2.7 ± 1.0	$4.3^{+1.6}_{-1.4}$	2.0 ± 0.8
Total SM	23 ± 4	4.2 ± 1.5	10.6 ± 1.8	$8.5^{+1.7}_{-1.6}$	$12.9^{+2.4}_{-2.3}$	$6.6^{+1.9}_{-1.8}$
Data	36	5	9	9	11	13

Sample	SR0τa-bin07	SR0τa-bin08	SR0τa-bin09	SR0τa-bin10	SR0τa-bin11	SR0τa-bin12
WZ	7.6 ± 1.3	$0.30^{+0.25}_{-0.24}$	$16.2^{+3.2}_{-3.1}$	$13.1^{+2.5}_{-2.6}$	19 ± 4	3.7 ± 1.2
ZZ	$0.55^{+0.16}_{-0.14}$	$0.012^{+0.008}_{-0.007}$	$1.43^{+0.32}_{-0.28}$	$0.60^{+0.12}_{-0.13}$	0.7 ± 1.2	0.14 ± 0.09
$t\bar{t}V + tZ$	$0.04^{+0.15}_{-0.04}$	$0.12^{+0.13}_{-0.12}$	$0.16^{+0.09}_{-0.12}$	0.12 ± 0.10	$0.41^{+0.24}_{-0.22}$	0.12 ± 0.11
VVV	0.9 ± 0.9	$0.13^{+0.14}_{-0.13}$	$0.23^{+0.24}_{-0.23}$	0.4 ± 0.4	0.6 ± 0.6	0.6 ± 0.6
Higgs	$0.98^{+0.29}_{-0.30}$	0.13 ± 0.06	0.32 ± 0.11	$0.22^{+0.10}_{-0.11}$	0.28 ± 0.12	0.12 ± 0.06
Reducible	$4.0^{+1.5}_{-1.4}$	$0.40^{+0.27}_{-0.26}$	$4.1^{+1.3}_{-1.2}$	$1.9^{+0.9}_{-0.8}$	$5.7^{+2.1}_{-1.9}$	$0.9^{+0.5}_{-0.4}$
Total SM	14.1 ± 2.2	1.1 ± 0.4	$22.4^{+3.6}_{-3.4}$	16.4 ± 2.8	27 ± 5	$5.5^{+1.5}_{-1.4}$
Data	15	1	28	24	29	8

Table A.2: Expected numbers of SM background events and observed numbers of data events in the signal regions SR0τa-bin13–bin20 for 20.3 fb^{-1}. Statistical and systematic uncertainties are included as described in section 7.6.

Sample	SR0τa-bin13	SR0τa-bin14	SR0τa-bin15	SR0τa-bin16	SR0τa-bin17	SR0τa-bin18
WZ	613 ± 65	207^{+33}_{-32}	58^{+12}_{-13}	$3.9^{+1.6}_{-1.4}$	50^{+7}_{-6}	2.3 ± 1.3
ZZ	29 ± 4	5.5 ± 1.5	$3.5^{+1.1}_{-1.0}$	$0.12^{+0.08}_{-0.07}$	$2.4^{+0.7}_{-0.6}$	0.08 ± 0.04
$t\bar{t}V + tZ$	$2.9^{+0.7}_{-0.6}$	$2.0^{+0.7}_{-0.6}$	$0.67^{+0.29}_{-0.28}$	$0.08^{+0.10}_{-0.08}$	0.8 ± 0.5	$0.15^{+0.16}_{-0.15}$
VVV	1.3 ± 1.3	0.8 ± 0.8	1.0 ± 1.0	0.33 ± 0.33	3.2 ± 3.2	0.5 ± 0.5
Higgs	2.2 ± 0.7	0.98 ± 0.20	0.31 ± 0.11	0.033 ± 0.018	0.95 ± 0.29	0.05 ± 0.04
Reducible	68^{+21}_{-19}	$2.2^{+1.9}_{-2.0}$	1.2 ± 0.6	$0.14^{+0.25}_{-0.14}$	$11.3^{+3.5}_{-3.2}$	0.27 ± 0.20
Total SM	715 ± 70	219 ± 33	65 ± 13	$4.6^{+1.7}_{-1.5}$	69^{+9}_{-8}	3.4 ± 1.4
Data	714	214	63	3	60	1

Sample	SR0τa-bin19	SR0τa-bin20
WZ	0.9 ± 0.4	0.12 ± 0.11
ZZ	0.021 ± 0.019	0.009 ± 0.009
$t\bar{t}V + tZ$	$0.0023^{+0.0032}_{-0.0019}$	
VVV	0.08 ± 0.08	$0.07^{+0.08}_{-0.07}$
Higgs	0.007 ± 0.006	0.0009 ± 0.0004
Reducible	$0.17^{+0.16}_{-0.15}$	$0.08^{+0.11}_{-0.08}$
Total SM	1.2 ± 0.4	$0.29^{+0.18}_{-0.17}$
Data	0	0

Table A.3: Expected numbers of SM background events and observed numbers of data events in the signal regions SR0τb, SR1τ, SR2τa and SR2τb for 20.3 fb^{-1}. Statistical and systematic uncertainties are included as described in section 7.6.

Sample	SR0τb	SR1τ	SR2τa	SR2τb
WZ	0.68 ± 0.20	4.6 ± 0.6	$1.51^{+0.35}_{-0.33}$	$2.09^{+0.30}_{-0.31}$
ZZ	0.028 ± 0.009	0.36 ± 0.08	$0.049^{+0.016}_{-0.014}$	0.135 ± 0.025
$t\bar{t}V + tZ$	$0.17^{+0.32}_{-0.17}$	$0.16^{+0.18}_{-0.16}$	$0.21^{+0.27}_{-0.21}$	$0.023^{+0.015}_{-0.018}$
VVV	1.0 ± 1.0	0.5 ± 0.5	0.09 ± 0.09	0.031 ± 0.033
Higgs	0.49 ± 0.17	0.28 ± 0.12	0.021 ± 0.010	0.08 ± 0.04
Reducible	1.5 ± 0.4	4.3 ± 0.8	5.1 ± 0.7	4.9 ± 0.7
Total SM	3.8 ± 1.2	10.3 ± 1.2	6.9 ± 0.8	$7.2^{+0.7}_{-0.8}$
Data	3	13	6	5

Appendix B

Improvements to the ATLAS offline shifter Tools

This section introduces the technical work done in order to obtain the ATLAS authorship qualification. The main purpose of this task was to add and improve features of some of the main tools available for the so-called "trigger offline" shifts. In these shifts the quality of the data collected by the ATLAS detector is thoroughly analysed to identify failures in the data processing with the ATLAS trigger, in particular in those areas where the trigger fails to promptly categorise events during data taking.

B.1 Offline Data Quality

For each physics object, one or more trigger objects can be defined (μ, τ, e, γ, jet, b-tagged jet and $E_{\mathrm{T}}^{\mathrm{miss}}$); given the complexity of the ATLAS trigger system, thorough monitoring of the performance of these trigger objects is vital. A data quality assessment of the events as soon as they are collected by the experiments was developed and deployed successfully in 2011, including tools which tested the analysis of events whilst data taking (online analysis) as well as the events produced after standard reconstruction is performed (offline analysis). The online data quality analysis focuses on major failures in the system and corrects them instantly, while the offline part is used to verify the online assessment and also to perform a more detailed analysis and filter out unsuitable data for physics analyses.

B.2 Debug Stream

Data for which the HLT failed to make a decision are automatically streamed into an output category known as the "debug stream". Events that "fire" the debug stream are still considered for analysis, based on the assumption that only a small fraction of those events are unsuitable for physics. The offline data quality assessment ensures that all debug stream events are recovered after reprocessing of the raw data with validated improvements in the trigger configuration, and also provides tools to distinguish between known and unknown problems during data taking, which can help understand the behaviour of the trigger.

Events where an error is detected at the level of the trigger are sent to the debug stream for further evaluation. These are events where one or more trigger algorithms failed, and therefore a trigger decision is not possible. These trigger events can be categorised as type L2 or EF, depending on which stage these events ended up in the debug stream. For example, very busy events (large pileup, large number of tracks, etc) can cause a timeout in the execution of the trigger algorithm. A list of the most frequent debug stream errors found in in 2011 and 2012 are listed in Table B.1.

Table B.1: Main types of debug stream errors.

Name	HLT system	Description
L2HltError	L2	Level-2 algorithm errors.
L2HltTimeout	L2	Level-2 timeouts which are usually recovered.
L2ForcedAccept	L2	Event algorithm timeouts at Level-2, reprocessing usually leads to recovery.
L2ProcTimeout	L2	Event processing timeout where the result at Level-2 is lost.
L2MissingData	L2	Major problem that leads to all events ending up in the debug stream.
efdProcTimeout	L2,EF	HLT processing timeout expired.
EFHLTError	EF	Severe algorithm errors at EF, which abort the event processing.
EFHltTimeout	EF	Event algorithm timeouts at EF, usually can be recovered.
EFMissingData	EF	Major problem that leads to all events ending up in the debug stream.

Events in the debug stream are analysed offline to study problems in the online system caused by the trigger. Such information is provided in detail with the dedicated tools for the analysis of debug stream events, which are aimed to promptly identify problems and while doing so, reducing the turn-around time for fixing these problems in future data

taking. Debug stream analysis tools produce several histograms needed for online and offline systems, however, this document will focus only on the description of some of the tools and histograms used during 2012. These are described in the following sections.

B.2.1 Automatic debug stream defect and web interface

The first part of my qualification task involved producing many debug stream analysis histograms by using legacy code as well as developed code. The analysis involved assessing whether there were too many events in the debug stream, i.e. more than 5% of the total number of events per luminosity block. In such cases, the production of a new histogram would take place, which contained information of the ratio of debug stream events and total events, clearly highlighting the luminosity block and run number for data with such feature. Finally an automated email notification to the expert shifters mailing list was sent out in these instances to warn the shifter and have him/her take immediate action. These plots were included along with the default histograms for the debug stream analysis in the official ATLAS trigger offline monitoring web-pages. The web-pages were also redesigned as part of my technical work, this re-design was motivated mainly to highlight the relevant information for the shifter without inspecting an overwhelming number of histograms by hand. An example of such plot is shown in Figure B.1.

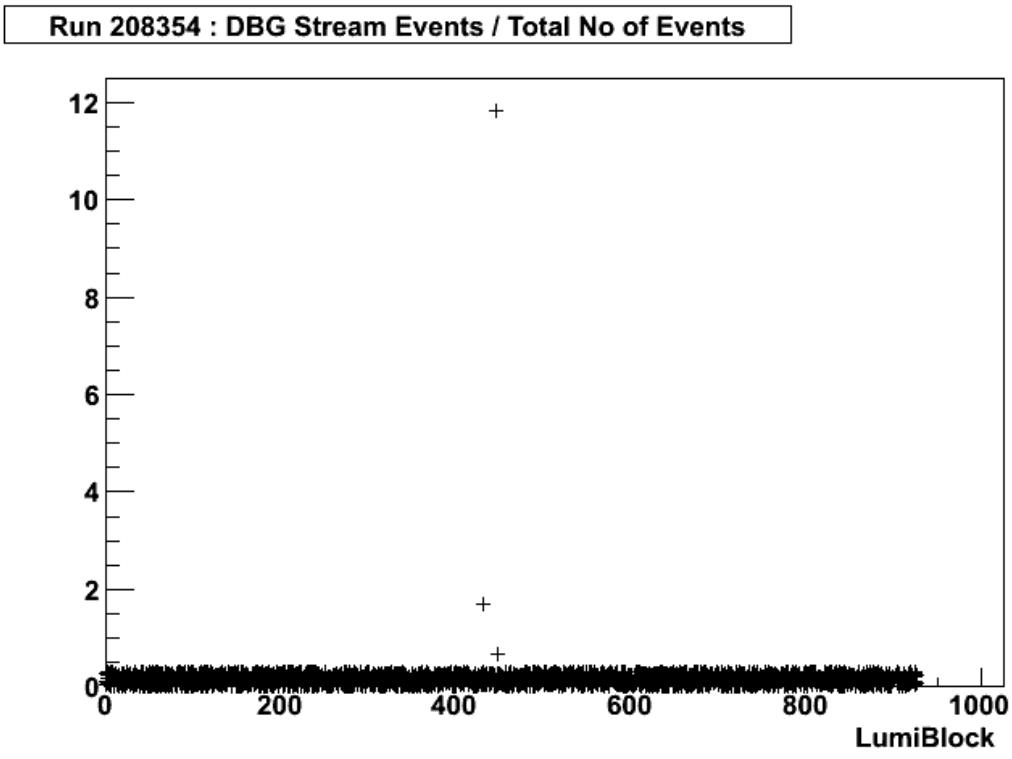

Figure B.1: Percentage of debug stream events in a given luminosity block [123].

These features were in place and fully functional throughout Run2.

B.2.2 New debug stream analysis histograms

Generally, one of the most useful things a shifter could know is whether a specific type of debug stream error was understood or even known. This motivated the need for a histogram with the error history over a relevant time period, in this case we set this to be 60 runs (also for cosmetic reasons). An example of a "history plot" is shown in Figure B.2. The y-axis incorporates the elements of Figure B.1 by showing the percentage of debug stream events.

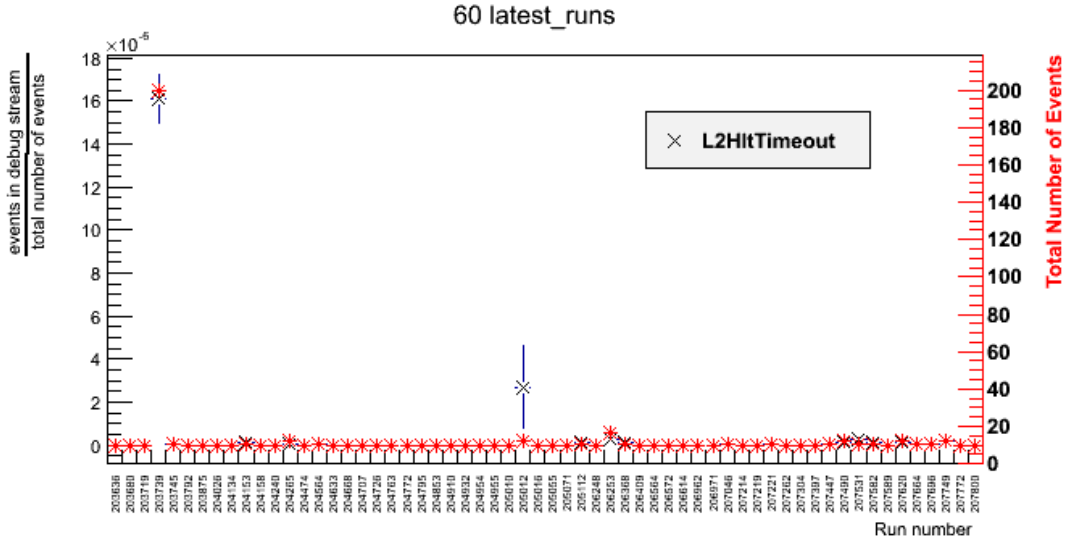

Figure B.2: Debug stream error history plot. [123].

These features were in place and fully functional throughout Run2.

Bibliography

[1] I. Melzer-Pellmann and P. Pralavorio, *Lessons for SUSY from the LHC after the first run*, Eur.Phys.J. **C74** (2014) 2801, arXiv:1404.7191 [hep-ex]. viii, 12

[2] ATLAS Collaboration, *Search for direct production of charginos and neutralinos in events with three leptons and missing transverse momentum in sqrt(s) = 8TeV pp collisions with the ATLAS detector*, arXiv:1402.7029 [hep-ex]. 1, 68, 70, 90, 92, 96, 118, 119, 120, 122, 123, 124, 125, 126, 127, 128, 130, 131, 132, 133

[3] C. Burgess and G. Moore, *The standard model: A primer*. Cambridge University Press, 2007. 2, 5

[4] G. Altarelli, *Collider Physics within the Standard Model: a Primer*, arXiv:1303.2842 [hep-ph]. 2

[5] W. Cottingham and D. Greenwood, *An Introduction to the Standard Model of Particle Physics*. Cambridge University Press, 2007. 2

[6] D. Bailin and A. Love, *Introduction to Gauge Field Theory Revised Edition*. Graduate Student Series in Physics. Taylor & Francis, 1993. 2

[7] B. Martin and G. Shaw, *Particle Physics*. Manchester Physics Series. Wiley, 2008. 4, 5

[8] Ellis, R. K., W. J. Stirling, and B. R. Webber, *QCD and Collider Physics*. Cambridge University Press, Cambridge, UK, 1996. 4

[9] C. Quigg, *The Electroweak theory*, arXiv:hep-ph/0204104 [hep-ph]. 4

[10] S. Raby, *Grand Unified Theories*, arXiv:hep-ph/0608183 [hep-ph]. 4

[11] C. Quigg, *Gauge Theories of the Strong, Weak, and Electromagnetic Interactions*. Advanced book classics. Addison-Wesley, 1983. 5

[12] A. Pich, *Quantum chromodynamics*, arXiv:hep-ph/9505231 [hep-ph]. 5

[13] J. B. et al. (Particle Data Group) Phys. Rev. D86 **010001** (2012). 6

[14] R. Mann, *An Introduction to Particle Physics and the Standard Model*. Taylor & Francis, 2011. 6

[15] L. Alvarez-Gaume and J. Ellis, *Eyes on a prize particle*, vol. 7. 2011. http://dx.doi.org/10.1038/nphys1874. Editorial Material. 7

[16] W. Hollik, *Quantum field theory and the Standard Model*, arXiv:1012.3883. 8

[17] ATLAS Collaboration, *Observation of a new particle in the search for the Standard Model Higgs boson with the ATLAS detector at the LHC*, Phys.Lett. **B716** (2012) 1–29, arXiv:1207.7214 [hep-ex]. 8, 22

[18] CMS Collaboration, *Observation of a new boson at a mass of 125 GeV with the CMS experiment at the LHC*, Phys.Lett. **B716** (2012) 30–61, arXiv:1207.7235 [hep-ex]. 8, 22

[19] *Projections for measurements of Higgs boson cross sections, branching ratios and coupling parameters with the ATLAS detector at a HL-LHC*, Tech. Rep. ATL-PHYS-PUB-2013-014, CERN, Geneva, Oct, 2013. 8

[20] CMS Collaboration, V. Khachatryan et al., *Constraints on the Higgs boson width from off-shell production and decay to Z-boson pairs*, Phys.Lett. **B736** (2014) 64, arXiv:1405.3455 [hep-ex]. 8

[21] https://atlas.web.cern.ch/Atlas/GROUPS/PHYSICS/CombinedSummaryPlots/SM/. 8, 9

[22] J. F. Donoghue, *The Fine-tuning problems of particle physics and anthropic mechanisms*, arXiv:0710.4080 [hep-ph]. 9

[23] A. Djouadi, *The anatomy of electroweak symmetry breaking Tome II: The Higgs bosons in the Minimal Supersymmetric Model*, Physics Reports **459** no. 16, (2008) 1 – 241. http://www.sciencedirect.com/science/article/pii/S0370157307004346. 9, 13, 14

[24] Planck Collaboration, *Planck 2013 results. XVI. Cosmological parameters*, arXiv:1303.5076 [astro-ph.CO]. 10

[25] S. P. Martin, *A Supersymmetry primer*, arXiv:hep-ph/9709356 [hep-ph]. 11

[26] Y. Shadmi, *Supersymmetry breaking*, arXiv:hep-th/0601076 [hep-th]. 11

[27] F. Jegerlehner, *The hierarchy problem of the electroweak Standard Model revisited*, arXiv:1305.6652 [hep-ph]. 12

[28] A. Djouadi, J.-L. Kneur, and G. Moultaka, *SuSpect: A Fortran code for the supersymmetric and Higgs particle spectrum in the MSSM*, Comput.Phys.Commun. **176** (2007) 426–455, arXiv:hep-ph/0211331 [hep-ph]. 12, 21

[29] J. Alwall et al., *Simplified Models for a First Characterization of New Physics at the LHC*, Phys. Rev. **D 79** (2009) 075020, arXiv:0810.3921 [hep-ph]. 13

[30] M. W. Cahill-Rowley, J. L. Hewett, S. Hoeche, A. Ismail, and T. G. Rizzo, *The New Look pMSSM with Neutralino and Gravitino LSPs*, Eur.Phys.J. **C72** (2012) 2156, arXiv:1206.4321 [hep-ph]. 13, 21

[31] *Search for squarks and gluinos with the ATLAS detector in final states with jets and missing transverse momentum and 20.3 fb^{-1} of $\sqrt{s} = 8$ TeV proton-proton collision data*, Tech. Rep. ATLAS-CONF-2013-047, CERN, Geneva, May, 2013. https://cds.cern.ch/record/1547563/files/ATLAS-CONF-2013-047.pdf. 14

[32] www.thphys.uni-heidelberg.de/~plehn/includes/prospino/prospino_lhc8.eps. 15

[33] G. R. Farrar and P. Fayet, *Phenomenology of the production, decay, and detection of new hadronic states associated with supersymmetry*, Physics Letters B **76** no. 5, (1978) 575 – 579. http://www.sciencedirect.com/science/article/pii/0370269378908584. 17

[34] R. Fleischer, *Flavour Physics and CP Violation*, arXiv:hep-ph/0608010 [hep-ph]. 21

[35] O. S. Brüning, P. Collier, P. Lebrun, S. Myers, R. Ostojic, J. Poole, and P. Proudlock, *LHC Design Report*. CERN, Geneva, 2004. 26, 28

[36] *LEP design report*. CERN, Geneva, 1984. Copies shelved as reports in LEP, PS and SPS libraries. 26

[37] LHCb Collaboration, *The LHCb Detector at the LHC*, JINST **3** (2008) S08005. 26

[38] ALICE Collaboration, *The ALICE experiment at the CERN LHC*, Journal of Instrumentation **3** no. 08, (2008) S08002. http://stacks.iop.org/1748-0221/3/i=08/a=S08002. 26

[39] ATLAS Collaboration, *The ATLAS Experiment at the CERN Large Hadron Collider*, Journal of Instrumentation **3** no. 08, (2008) S08003. http://stacks.iop.org/1748-0221/3/i=08/a=S08003. 26, 30, 34, 36, 39

[40] CMS Collaboration, *The CMS experiment at the CERN LHC*, Journal of Instrumentation **3** no. 08, (2008) S08004. http://stacks.iop.org/1748-0221/3/i=08/a=S08004. 26

[41] *The four main LHC experiments*, Jun, 1999. http://www.atlas.ch/photos/detector-site-surface.html. 27

[42] J. Haffner, *The CERN accelerator complex. Complexe des acclrateurs du CERN*, Oct, 2013. https://cds.cern.ch/record/1260465. General Photo. 28

[43] J. Pequenao, *Computer generated image of the whole ATLAS detector*, Mar, 2008. https://cds.cern.ch/record/1095924. 29

[44] A. Yamamoto, Y. Makida, R. Ruber, Y. Doi, T. Haruyama, F. Haug, H. ten Kate, M. Kawai, T. Kondo, Y. Kondo, J. Metselaar, S. Mizumaki, G. Olesen, O. Pavlov, S. Ravat, E. Sbrissa, K. Tanaka, T. Taylor, and H. Yamaoka, *The ATLAS central solenoid*, Nuclear Instruments and Methods in Physics Research Section A: Accelerators, Spectrometers, Detectors and Associated Equipment **584** no. 1, (2008) 53 – 74. http://www.sciencedirect.com/science/article/pii/S0168900207020414. 30, 31

[45] ATLAS Collaboration, *Expected Performance of the ATLAS Experiment - Detector, Trigger and Physics*, arXiv:0901.0512 [hep-ex]. 31, 33, 40, 45, 61

[46] J. Pequenao, *Computer generated image of the ATLAS inner detector*, Mar, 2008. https://cds.cern.ch/record/1095926. 32, 33

[47] D. Fasching, *The ATLAS pixel detector*, Nuclear Instruments and Methods in Physics Research Section A: Accelerators, Spectrometers, Detectors and Associated Equipment **408** no. 1, (1998) 229 – 234. http://www.sciencedirect.com/science/article/pii/S0168900298002472. 32

[48] ATLAS TRT Collaboration, *The ATLAS TRT and its Performance at LHC*, Journal of Physics: Conference Series **347** no. 1, (2012) 012025. http://stacks.iop.org/1742-6596/347/i=1/a=012025. 33

[49] ATLAS TRT Collaboration, *Electron identification with a prototype of the Transition Radiation Tracker for the ATLAS experiment*, Nuclear Instruments and Methods in Physics Research Section A: Accelerators, Spectrometers, Detectors and Associated Equipment **412** no. 23, (1998) 200 – 215. http://www.sciencedirect.com/science/article/pii/S0168900298004574. 33

[50] ATLAS Collaboration, *ATLAS liquid-argon calorimeter: Technical Design Report*. Technical Design Report ATLAS. CERN, Geneva, 1996. https://cds.cern.ch/record/331061. 34

[51] J. Pequenao, *Computer Generated image of the ATLAS calorimeter*, Mar, 2008. https://cds.cern.ch/record/1095927. 35

[52] ATLAS Collaboration, *ATLAS muon spectrometer: Technical design report*,. https://cds.cern.ch/record/331068. 36

[53] ATLAS Collaboration, *Performance of the ATLAS Trigger System in 2010*, Eur.Phys.J. **C72** (2012) 1849, arXiv:1110.1530 [hep-ex]. 38

[54] ATLAS Collaboration, *The ATLAS Simulation Infrastructure*, Eur.Phys.J. **C70** (2010) 823–874, arXiv:1005.4568 [physics.ins-det]. 41

[55] J. M. Campbell, J. Huston, and W. Stirling, *Hard Interactions of Quarks and Gluons: A Primer for LHC Physics*, Rept.Prog.Phys. **70** (2007) 89, arXiv:hep-ph/0611148 [hep-ph]. 42

[56] S. Agostinelli, J. Allison, K. Amako, J. Apostolakis, and H. Araujo, *Geant4 simulation toolkit*, Nuclear Instruments and Methods in Physics Research Section A: Accelerators, Spectrometers, Detectors and Associated Equipment **506** no. 3, (2003) 250 – 303. http://www.sciencedirect.com/science/article/pii/S0168900203013688. 43

[57] ATLAS Collaboration, M. Beckingham, M. Duehrssen, E. Schmidt, M. Shapiro, M. Venturi, J. Virzi, I. Vivarelli, M. Werner, S. Yamamoto, and T. Yamanaka, *The simulation principle and performance of the ATLAS fast calorimeter simulation FastCaloSim*,. 44

[58] ATLAS Collaboration, W. Liebig, *Track and vertex reconstruction in ATLAS*, PoS **VERTEX2007** (2007) 025. 46

[59] W. Lampl, S. Laplace, D. Lelas, P. Loch, H. Ma, S. Menke, S. Rajagopalan, D. Rousseau, S. Snyder, and G. Unal, *Calorimeter Clustering Algorithms: Description and Performance*, Tech. Rep. ATL-LARG-PUB-2008-002. ATL-COM-LARG-2008-003, CERN, Geneva, Apr, 2008. https://cds.cern.ch/record/1099735. 46, 48

[60] ATLAS Collaboration, *Electron performance measurements with the ATLAS detector using the 2010 LHC proton-proton collision data*, Eur. Phys. J. **C 72** (2012) 1909, arXiv:1110.3174 [hep-ex]. 46, 47, 58, 108

[61] https://atlas.web.cern.ch/Atlas/GROUPS/PHYSICS/EGAMMA/PublicPlots/20130926/ATL-COM-PHYS-2013-1287/ATL-COM-PHYS-2013-1287.pdf. 47, 60

[62] ATLAS Collaboration, B. Resende, *Muon identification algorithms in ATLAS*, PoS **EPS-HEP2009** (2009) 431. 47

[63] ATLAS Collaboration, *Muon Momentum Resolution in First Pass Reconstruction of pp Collision Data Recorded by ATLAS in 2010*, ATLAS-CONF-2011-046. http://cdsweb.cern.ch/record/1338575. 48

[64] *Preliminary results on the muon reconstruction efficiency, momentum resolution, and momentum scale in ATLAS 2012 pp collision data*, Tech. Rep. ATLAS-CONF-2013-088, CERN, Geneva, Aug, 2013. https://cds.cern.ch/record/1580207. 48, 108

[65] M. Cacciari, G. P. Salam, and G. Soyez, *The Anti-k(t) jet clustering algorithm*, JHEP **0804** (2008) 063, arXiv:0802.1189 [hep-ph]. 48

[66] ATLAS Collaboration, *Jet energy scale and its systematic uncertainty in proton-proton collisions at sqrt(s)=7 TeV with ATLAS 2011 data*, Tech. Rep. ATLAS-CONF-2013-004, CERN, Geneva, Jan, 2013. https://cds.cern.ch/record/1509552. 48

[67] A. B. Galtieri, F. Margaroli, and I. Volobouev, *Precision measurements of the top quark mass from the Tevatron in the pre-LHC era*, Reports on Progress in Physics **75** no. 5, (2012) 056201. http://stacks.iop.org/0034-4885/75/i=5/a=056201. 49

[68] ATLAS Collaboration, *Commissioning of the ATLAS high-performance b-tagging algorithms in the 7 TeV collision data*, tech. rep., 2011. https://cds.cern.ch/record/1369219. 49

[69] *Calibration of b-tagging using dileptonic top pair events in a combinatorial likelihood approach with the ATLAS experiment*, Tech. Rep. ATLAS-CONF-2014-004, CERN, Geneva, Feb, 2014. https://cds.cern.ch/record/1664335. 49, 61, 62

[70] ATLAS Collaboration, *Luminosity Determination in pp Collisions at $\sqrt{s} = 7$ TeV Using the ATLAS Detector at the LHC*, Eur.Phys.J. **C71** (2011) 1630, arXiv:1101.2185 [hep-ex]. 50

[71] T. Sjostrand, S. Mrenna, and P. Z. Skands, *PYTHIA 6.4 Physics and Manual*, JHEP **0605** (2006) 026, arXiv:hep-ph/0603175 [hep-ph]. 51

[72] G. Corcella, I. Knowles, G. Marchesini, S. Moretti, K. Odagiri, et al., *HERWIG 6: An Event generator for hadron emission reactions with interfering gluons (including supersymmetric processes)*, JHEP **0101** (2001) 010, arXiv:hep-ph/0011363 [hep-ph]. 51

[73] M. Bahr, S. Gieseke, M. Gigg, D. Grellscheid, K. Hamilton, et al., *Herwig++ Physics and Manual*, Eur.Phys.J. **C58** (2008) 639–707, arXiv:0803.0883 [hep-ph]. 51

[74] J. Butterworth et al., *Multiparton interactions in photoproduction at HERA*, Z. Phys. **C 72** (1996) 637–646, arXiv:hep-ph/9601371 [hep-ph]. 51

[75] T. Gleisberg, S. Hoeche, F. Krauss, M. Schonherr, S. Schumann, et al., *Event generation with SHERPA 1.1*, JHEP **0902** (2009) 007, arXiv:0811.4622 [hep-ph]. 51

[76] M. L. Mangano et al., *ALPGEN, a generator for hard multiparton processes in hadronic collisions*, JHEP **07** (2003) 001, arXiv:hep-ph/0206293 [hep-ph]. 51

[77] J. Alwall et al., *MadGraph/MadEvent v4: The New Web Generation*, JHEP **09** (2007) 028, arXiv:0706.2334 [hep-ph]. 51

[78] B. P. Kersevan and E. Richter-Was, *The Monte Carlo event generator AcerMC versions 2.0 to 3.8 with interfaces to PYTHIA 6.4, HERWIG 6.5 and ARIADNE 4.1*, Comput. Phys. Commun. **184** no. 3, (2013) 919 – 985. 51

[79] S. Catani, F. Krauss, R. Kuhn, and B. Webber, *QCD matrix elements + parton showers*, JHEP **0111** (2001) 063, arXiv:hep-ph/0109231 [hep-ph]. 52

[80] M. L. Mangano, M. Moretti, and R. Pittau, *Multijet matrix elements and shower evolution in hadronic collisions: $Wb\bar{b}$ + n jets as a case study*, Nucl.Phys. **B632** (2002) 343–362, arXiv:hep-ph/0108069 [hep-ph]. 52

[81] S. Frixione and B. R. Webber, *Matching NLO QCD computations and parton shower simulations*, JHEP **06** (2002) 029, arXiv:hep-ph/0204244. 52

[82] P. Nason, *A New method for combining NLO QCD with shower Monte Carlo algorithms*, JHEP **11** (2004) 040, arXiv:hep-ph/0409146 [hep-ph]. 52

[83] *ATLAS tunes of PYTHIA 6 and Pythia 8 for MC11*, Tech. Rep. ATL-PHYS-PUB-2011-009, CERN, Geneva, Jul, 2011. https://cds.cern.ch/record/1363300. 53

[84] J. Pumplin, D. Stump, J. Huston, H. Lai, P. M. Nadolsky, et al., *New generation of parton distributions with uncertainties from global QCD analysis*, JHEP **0207** (2002) 012, arXiv:hep-ph/0201195 [hep-ph]. 53

[85] H.-L. Lai, M. Guzzi, J. Huston, Z. Li, P. M. Nadolsky, et al., *New parton distributions for collider physics*, Phys.Rev. **D82** (2010) 074024, arXiv:1007.2241 [hep-ph]. 53

[86] J. Campbell, R. Ellis, and C. Williams, *Vector boson pair production at the LHC*, Journal of High Energy Physics **2011** no. 7, (2011) 1–36. http://dx.doi.org/10.1007/JHEP07%282011%29018. 54

[87] J. M. Campbell and R. K. Ellis, *An Update on vector boson pair production at hadron colliders*, Phys.Rev. **D60** (1999) 113006, arXiv:hep-ph/9905386 [hep-ph]. 54

[88] F. Campanario, V. Hankele, C. Oleari, S. Prestel, and D. Zeppenfeld, *QCD corrections to charged triple vector boson production with leptonic decay*, Phys. Rev. D **78** (2008) 094012. http://link.aps.org/doi/10.1103/PhysRevD.78.094012. 54

[89] J. Campbell and R. Ellis, *$t\bar{t}W^{\pm}$ production and decay at NLO*, Journal of High Energy Physics **2012** no. 7, (2012) 1–12. http://dx.doi.org/10.1007/JHEP07%282012%29052. 54, 106

[90] A. Kardos, Z. Trócsányi, and C. G. Papadopoulos, *Top quark pair production in association with a Z boson at next-to-leading-order accuracy*, Phys. Rev. D **85** (2012) 054015. http://link.aps.org/doi/10.1103/PhysRevD.85.054015. 54, 106

[91] J. Campbell, R. K. Ellis, and R. Rtsch, *Single top production in association with a Z boson at the LHC*, Phys.Rev. **D87** no. 11, (2013) 114006, arXiv:1302.3856 [hep-ph]. 54

[92] M. Aliev, H. Lacker, U. Langenfeld, S. Moch, P. Uwer, and M. Wiedermann, *HATHOR - HAdronic Top and Heavy quarks crOss section calculatoR*, Computer Physics Communications **182** no. 4, (2011) 1034 – 1046. http://www.sciencedirect.com/science/article/pii/S0010465510005333. 54

[93] N. Kidonakis, *Next-to-next-to-leading-order collinear and soft gluon corrections for t-channel single top quark production*, Phys.Rev. **D83** (2011) 091503, arXiv:1103.2792 [hep-ph]. 54

[94] N. Kidonakis, *NNLL resummation for s-channel single top quark production*, Phys.Rev. **D81** (2010) 054028, arXiv:1001.5034 [hep-ph]. 54

[95] N. Kidonakis, *Two-loop soft anomalous dimensions for single top quark associated production with a W- or H-*, Phys.Rev. **D82** (2010) 054018, arXiv:1005.4451 [hep-ph]. 54

[96] S. Catani, L. Cieri, G. Ferrera, D. de Florian, and M. Grazzini, *Vector Boson Production at Hadron Colliders: A Fully Exclusive QCD Calculation at Next-to-Next-to-Leading Order*, Phys. Rev. Lett. **103** (2009) 082001. http://link.aps.org/doi/10.1103/PhysRevLett.103.082001. 54

[97] S. Dittmaier, S. Dittmaier, C. Mariotti, G. Passarino, R. Tanaka, et al., *Handbook of LHC Higgs Cross Sections: 2. Differential Distributions*, arXiv:1201.3084 [hep-ph]. 54, 106

[98] W. Beenakker, R. Hopker, M. Spira, and P. Zerwas, *Squark and gluino production at hadron colliders*, Nucl.Phys. **B492** (1997) 51–103, arXiv:hep-ph/9610490 [hep-ph]. 54

[99] ATLAS Collaboration, *Measurement of the $W \to \ell\nu$ and $Z/\gamma^* \to \ell\ell$ production cross sections in proton-proton collisions at $\sqrt{s} = 7$ TeV with the ATLAS detector*, JHEP **1012** (2010) 060, arXiv:1010.2130 [hep-ex]. 60

[100] ATLAS Collaboration, *Performance of the Reconstruction and Identification of Hadronic Tau Decays with ATLAS*, Tech. Rep. ATLAS-CONF-2011-152, CERN, Geneva, Nov, 2011. https://cds.cern.ch/record/1398195. 63

[101] *Identification of the Hadronic Decays of Tau Leptons in 2012 Data with the ATLAS Detector*, Tech. Rep. ATLAS-CONF-2013-064, CERN, Geneva, Jul, 2013. https://cds.cern.ch/record/1562839. 63, 64, 65, 66

[102] ATLAS Collaboration, *Performance of Missing Transverse Momentum Reconstruction in Proton-Proton Collisions at 7 TeV with ATLAS*, Eur.Phys.J. **C72** (2012) 1844, arXiv:1108.5602 [hep-ex]. 67, 109

[103] ATLAS Collaboration, *Search for direct production of charginos and neutralinos in events with three leptons and missing transverse momentum in 21 fb^{-1} of pp collisions at $\sqrt{s} = 8$ TeV with the ATLAS detector*, Tech. Rep. ATLAS-CONF-2013-035, CERN, Geneva, Mar, 2013. https://cds.cern.ch/record/1532426. 70, 74, 92, 107, 121, 133

[104] ATLAS Collaboration, *Search for direct production of charginos and neutralinos in events with three leptons and missing transverse momentum in 13.0 fb-1 of pp collisions at sqrt(s)=8 TeV with the ATLAS detector*, Tech. Rep. ATLAS-CONF-2012-154, CERN, Geneva, Nov, 2012. https://cds.cern.ch/record/1493493. 70, 74

[105] ATLAS Collaboration, *Search for direct production of charginos and neutralinos in events with three leptons and missing transverse momentum in $\sqrt{s} = 7$ TeV pp collisions with the ATLAS detector*, Phys.Lett. **B718** (2013) 841–859, arXiv:1208.3144 [hep-ex]. 70, 74

[106] M. Wielers, R. Mantifel, A. Tricoli, and P. Bell, *Single Electron Trigger Performance Plots*, Tech. Rep. ATL-COM-DAQ-2012-146, CERN, Geneva, Jun, 2012. https://cds.cern.ch/record/1456795. 71

[107] https://twiki.cern.ch/twiki/bin/view/AtlasPublic/MuonTriggerPublicResults#Muon_trigger_performances_in_AN1. 71

[108] ATLAS Collaboration, *Jet energy measurement with the ATLAS detector in proton-proton collisions at* $\sqrt{s} = 7$ *TeV*, Eur.Phys.J. **C73** (2013) 2304, arXiv:1112.6426 [hep-ex]. 72

[109] G. Cowan, K. Cranmer, E. Gross, and O. Vitells, *Asymptotic formulae for likelihood-based tests of new physics*, Eur.Phys.J. **C71** (2011) 1554, arXiv:1007.1727 [physics.data-an]. 73, 111, 112, 113

[110] https://twiki.cern.ch/twiki/bin/view/LHCPhysics/CrossSectionsFigures. 76

[111] A. Barr, C. Lester, and P. Stephens, *m(T2): The Truth behind the glamour*, J.Phys. **G29** (2003) 2343–2363, arXiv:hep-ph/0304226 [hep-ph]. 81

[112] C. Lester and D. Summers, *Measuring masses of semiinvisibly decaying particles pair produced at hadron colliders*, Phys.Lett. **B463** (1999) 99–103, arXiv:hep-ph/9906349 [hep-ph]. 81

[113] J. Butterworth, E. Dobson, U. Klein, B. Mellado Garcia, T. Nunnemann, J. Qian, D. Rebuzzi, and R. Tanaka, *Single Boson and Diboson Production Cross Sections in pp Collisions at sqrts=7 TeV*, Tech. Rep. ATL-COM-PHYS-2010-695, CERN, Geneva, Aug, 2010. https://cds.cern.ch/record/1287902. 106

[114] http://www.hep.ucl.ac.uk/pdf4lhc/PDF4LHC_practical_guide.pdf. 106

[115] ATLAS Collaboration, *Improved luminosity determination in pp collisions at* $\sqrt{s}$ *= 7 TeV using the ATLAS detector at the LHC*, Eur.Phys.J. **C73** (2013) 2518, arXiv:1302.4393 [hep-ex]. 107

[116] ATLAS Collaboration, *Measuring the b-tag efficiency in a top-pair sample with 4.7* fb^{-1} *of data from the ATLAS detector*, tech. rep., 2012. https://cds.cern.ch/record/1460443. 108

[117] ATLAS Collaboration, *Determination of the tau energy scale and the associated systematic uncertainty in proton-proton collisions at* $\sqrt{s} = 8$ *TeV with the ATLAS detector at the LHC in 2012*, ATL-PHYS-PUB-2013-044 (2013). https://cdsweb.cern.ch/record/1544036. 108

[118] M. Kramer, A. Kulesza, R. van der Leeuw, M. Mangano, S. Padhi, et al., *Supersymmetry production cross sections in pp collisions at* $\sqrt{s} = 7$ *TeV*, arXiv:1206.2892 [hep-ph]. 110

[119] A. L. Read, *Presentation of search results: the CL s technique*, Journal of Physics G: Nuclear and Particle Physics **28** no. 10, (2002) 2693. http://stacks.iop.org/0954-3899/28/i=10/a=313. 112, 113

[120] A. L. Read, *Modified frequentist analysis of search results (the CL_s method)*, Tech. Rep. CERN-OPEN-2000-205, 2000. https://cds.cern.ch/record/451614. 112

[121] E. Gross, *LHC Statistics for Pedestrians*,. https://cds.cern.ch/record/1099994. 112

[122] E. Gross and O. Vitells, *Trial factors for the look elsewhere effect in high energy physics*, European Physical Journal C **70** (2010) 525–530, arXiv:1005.1891 [physics.data-an]. 116

[123] https://atlas-trigmon.cern.ch/debug_stream/2012.php. 140, 141